Evaporation of Liquid Wall Film in Direct Injection Spark Ignition Engine-like Conditions

by

Song Yang

A thesis
presented to the University of Waterloo
in fulfillment of the
thesis requirement for the degree of
Doctor of Philosophy
in
Mechanical and Mechatronics Engineering

Waterloo, Ontario, Canada, 2019

Examining Committee Membership

The following served on the Examining Committee for this thesis. The decision of the Examining Committee is by majority vote.

External Examiner:	Dr. Xili Duan Associate Professor, Ph.D. Memorial University of Newfoundland
Supervisor:	Dr. Xianguo Li Professor, Ph.D.
Internal Member:	Dr. John Z. Wen Associate Professor, Ph.D.
Internal Member:	Dr. Fue-Sang Lien Professor, Ph.D.
Internal/External Member:	Dr. Xinzhi Liu Professor, Ph.D. Department of Applied Mathematics
Other Member(s)	N/A

Author's Declaration

I hereby declare that I am the sole author of this thesis. This is a true copy of the thesis, including any required final revisions, as accepted by my examiners.

I understand that my thesis may be made electronically available to the public.

Abstract

The liquid wall film formed by the spray impingement in Direct Injection Spark Ignition (DISI) engines can directly produce a large amount of Particulate Matter (PM) emissions. The PM emissions can be tremendously reduced if all the liquid wall film can evaporate completely before flame propagates to the wall surface and the combustion of 'pool fire' fed by the evaporating liquid wall film can be totally eliminated. Evaporation models are widely used to predict the evaporation of liquid wall film in engines, but requiring accurate mass transfer correlations. However, it is challenging to experimentally determine the accurate mass transfer correlations of the liquid wall film in engines; since the evaporation time of the thin liquid wall film in engines is quite short and the thickness of the liquid wall film is extremely thin. Thus, numerical simulation has become a useful tool to provide insight into the underlying transient evaporation characteristics of liquid wall film in DISI engine-like conditions and to derive the mass transfer correlations.

In this thesis research, numerical study has been conducted for a two-dimensional, two-phase, transient, non-isothermal and species transport problem representing the evaporation of liquid wall film in DISI engine-like conditions. The unique features of the numerical models are the inclusion of the transient motion and heating of the liquid phase, the blowing effects caused by evaporation, and the variation of thermo-physical properties. The governing equations which mathematically describe the transient evaporation process of liquid wall film in DISI engines, are discretized and solved using a Finite Volume Method (FVM) based software, Fluent, with its capability of User Defined Function (UDF) programming.

The numerical evaporation models are validated with existing analytical and experimental data; and good agreements are observed. Subsequently, the validated models are used for the numerical study of the evaporating liquid wall film in DISI engine-like conditions to investigate its transient

evaporation characteristics and determine its mass transfer correlations. The results show that the evaporation rate of liquid wall film, characterized by mass transfer coefficient, is non-uniform along the wall film, which is consistent with the development of species boundary layer and the decline of species concentration gradient within the boundary layer. The transient evaporation of liquid wall film in DISI engine-like conditions is mainly determined by the gas/liquid interfacial temperature, which can be directly affected by the transient heating of the liquid phase. The newly developed mass transfer correlations taking into account the blowing effects and effects caused by convection and the variation of thermo-physical properties during the transient evaporation process of the liquid wall film can predict their evaporation rate much more accurately than the existing correlations available in literature.

Acknowledgements

I would like to express my deepest gratitude to my supervisor, Dr. Xianguo Li, for his invaluable guidance, steady encouragement, inspiration and support throughout my Ph.D. I would also like to thank my committee members, Dr. Xili Duan, Dr. Xinzhi Liu, Dr. Fue-Sang Lien, and Dr. John Z. Wen for taking the time to scrutinize my thesis. Their comments are highly appreciated.

I would like to thank all my past and present group members, especially Dr. Ibrahim, E. Alaefour, Dr. Samaneh Shahgaldi, Dr. Jian Zhao, Dr. Abbaas, Dr. Bruck, Dr. Ronghui Qi and Dr. Huifang Kang, Dr. Zirong Yang, Mr. Yixiang Zhang, Mr. Xiaoyu Tan, Mr. Stephen, Grill, Dr. Yafei Chang, Dr. Haizhen Huang, Dr. Ping Sun, Dr. Yinggai Jin and Dr. Qian Xu. Without their help, accompany, encouragement and fruitful discussion throughout the course of my Ph.D., I would not have been able to put together this importance publication.

I would also like to express my sincere appreciation to my parents and siblings, for their unstopping support and love during the journey of pursuing my PhD degree. Also, I would like to thank my wife and parent in-law, their understanding and support are also a great source of encouragement in my study and life.

The financial support by the Chinese Scholarship Council and General Motor are also greatly appreciated.

Table of Contents

List of Figures

List of Tables

Nomenclature

A	Effective area (m^2)
B	Body forces $(kg/(m^2S^2))$
Cp	Heat capacity (J/K)
D	Mass diffusivity of species (m^2/s) in species equation/ Blending functions in the turbulence kinetic energy equations of low Reynolds turbulence model (m^2/S^2)
f	Volume fraction in the VOF equation/ damping functions in the low Reynolds turbulence model
G	Generation source term in the turbulence models / Gibbs free energy in Clausius-Clapeyron equation (kJ)
T	Temperature (K)
h	Mass average entropy (kJ/kg)
h_m	Mass transfer coefficient (m/s)
H	Wall film thickness (m)
I	Turbulence intensity (%)
K	Karman's constant
$\dot{m}$	Evaporation rate ($kg/(m^2s)$)
M	Molecular weight (kg/kmol)
N	Mass flux (kg/m^2)
Nu	Nusselt number
P	Pressure (Pa)
$\dot{Q}$	Heat transfer rate (w)
R	Universal gas constant ($J/mol \cdot K$)
Re	Reynolds number
Sh	Sherwood number

S	Source terms in conservation equations/ entropy in Clausius - Clapeyron equation
Sc	Schmidt number
Pr	Prandtl number
U	Velocity (m/s)
V	Volume (m^3) in the Volume of Fraction model/ atom volumes in Fuller's method of calculating the binary diffusivity $(\mathrm{cc}/\mathrm{mol})$
X	Molar fraction
Y	Dissipation rate $(\mathrm{m}^2/\mathrm{S}^3)$
Y_i	Mass fraction of component "i"

Greek letters

α	Thermal diffusivity $(\mathrm{m}^2/\mathrm{s})$ in energy transport equation/ volume fractions in the VOF model
σ	Turbulence Prandtl number
ρ	Density $(\mathrm{kg}/\mathrm{m}^3)$
μ	Dynamic viscosity $(\mathrm{kg}/(\mathrm{m}\cdot\mathrm{s}))$
v	Kinematic viscosity $(\mathrm{m}^2/\mathrm{s})$
τ	Shear stress $(\mathrm{kg}/(\mathrm{m}\cdot\mathrm{s}^2))$
k	Turbulent kinetic energy $(\mathrm{m}^2/\mathrm{s}^2)$ in turbulence models/ thermal conductivity $\mathrm{W}/(\mathrm{m}\cdot\mathrm{K})$ in energy equation
ε	Dissipation rate of turbulent kinetic energy$(\mathrm{m}^2/\mathrm{s}^3)$
ω	Specific dissipation rate of turbulent kinetic energy$(1/\mathrm{s})$

Subscripts and Superscripts

a	Air
b	Boiling point

cr	Critical condition
eff	Effective value
g	Gas phase
i	The i^{th} component
k	Phase index
l	Liquid phase
m	Molecular component for the calculation of thermos-physical properties/ gas mixture in the species transport equation
s	Interfacial value
sat	Saturation pressure
t	Turbulent component for the calculation of thermos-physical properties / time step for the transient numerical study
vap	Evaporating fuel vapor
x	x –coordinate
y	y –coordinate
0	Reference value (298.15 K and 1atm)
∞	Free stream value of the inlet flow conditions/ reference value in the Clausius-Clapeyron equation

Abbreviations

GHG	Greenhouse Gas
DISI	Direct Injection Spark Ignition
PM	Particulate Matters
CFD	Computational Fluid Dynamics
FVM	Finite Volume Method
SUR	Successive Under Relaxation

UDF	User Defined Functions
UDS	User Defined Scalars
VOF	Volume of Fluid
FT	Front Tracking
LS	Level Set
SLIC	Simple Line Interface Calculation
PLIC	Piecewise Linear Interface Calculation
SOLA	Solution Algorithm
DTSF	Diffusion through Stagnant Film
EMCD	Equal Molar Counter Diffusion
NEDC	New European Driving Cycle
RIM	Reflection Index Match
CARB	California Air Resource Board
LEV	Low Emission Vehicle
RNG	Renormalization Group
SST	Shear Stress Transport

Chapter 1
Introduction

1.1 Background

The formation of liquid wall film caused by the spray impingement in Direct Injection Spark Ignition (DISI) engines can directly cause the formation of Particle Matter (PM) in engines [1-2]. The 'pool fire' fed by the evaporating liquid wall film in DISI engines has been proved to be the major source of the engine-out PM emissions [3-6] from DISI engines. Thus, the PM emissions can be tremendously reduced if all the liquid wall film can evaporate out before the flame propagates to the wall surface and the combustion of 'pool fire' can be eliminated. However, the understanding of the evaporation of liquid wall film in engines is still limited, since the evaporation time of liquid wall film in engines is exceptionally short and its thickness is extremely small[7-10]. Moreover, accurate mass transfer correlations that can predict the transient evaporation rate effectively and efficiently are urgently needed by the automotive industry. Therefore, the evaporation of liquid wall film in DISI engine-like conditions is investigated in this thesis research.

The total amount of liquid wall film is only several micrograms (μg) and its life time is only in the order of millisecond (ms) [11 - 13]; therefore, to measure the evaporation of liquid wall film in engines experimentally is extremely challenging. Thus, numerical simulation has been adopted in this thesis study aiming at providing some insights on the transient evaporation characteristics of liquid wall film in DISI engine-like conditions and determining its mass transfer correlations.

1.2 Direct Injection Spark Ignition Engines

DISI engines have huge potential on the reduction of fuel consumption and Greenhouse Gas (GHG) emissions, which have attracted a plenty of research aiming at having a better understanding of its working process [7-19]. In addition, the amount of gaseous engine-out emission (UBHC, NOx and CO) can be reduced obviously in cold start and warming up operating conditions. Other advantages of DISI engines include faster transient response (rapid acceleration or deceleration), more precise air/fuel ratio control and better cold start performance. All these advantages have made the DISI engines the most promising candidate for the next generation of power source in automotive industry.

DISI engines can be classified into three different types as shown in Figure 1.1, depending on the complexity of the shape of the combustion chamber, positioning between spark plug and high-pressure fuel injector. In spray guided DISI engines, the distance between the high-pressure fuel injector and spark plug is relatively short and the shape of the combustion chamber is not as complicated as wall-guided or air-guided DISI engines. However, since the available time for fuel spray and air mixing is very short, the injection pressure in spray-guided DISI engines is quite high, which leads to higher cost for engine manufactures. In addition, the spark plug is prone to be wetted by the fuel spray, which can cause the fluctuation of engine output or even misfire and spark plug deficiency due to carbon deposition. For the air-guided DISI engines, the fluctuation of engine output power is large, due to the instable flow conditions in the engine combustion chamber. Thus, the wall-guided DISI engines are widely used in automotive engine industry, which is also the easiest type of engine to be implemented.

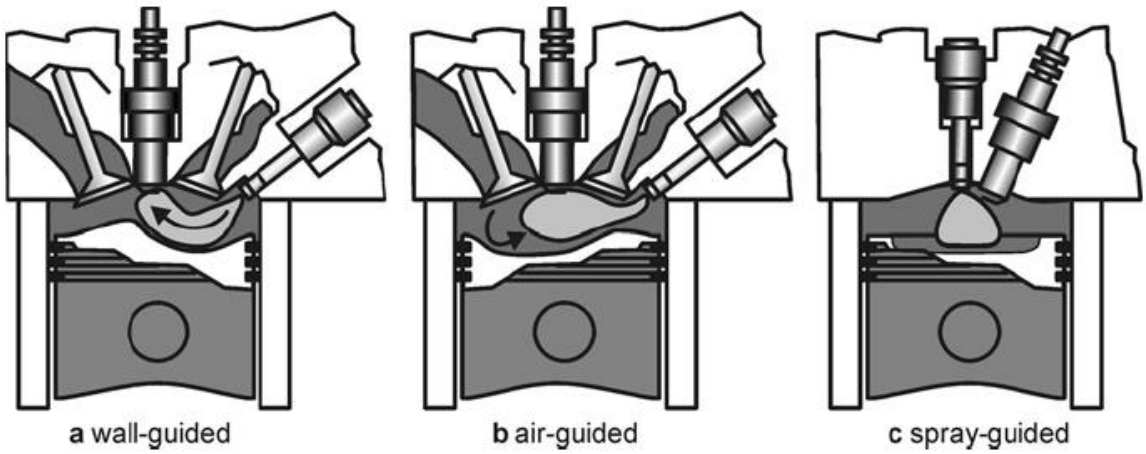

Figure 1.1: Schematic of different types of DISI engines [1].

1.2.1 Principle of Operation

In wall-guided DISI engines, fuel spray is injected into the combustion chamber directly instead of injecting into the intake manifold as in the conventional multi-point injection (MPI) gasoline engines. In DISI engines, the output power can be controlled though adjusting the quantity of injected fuel mass, rather than air flow throttling, which can significantly reduce the associated pumping losses. During partial load operation, the reduction of required fuel mass allows the DISI engine to operate with ultra-lean mixture. In order to work stably in the lean burn working mode, a stratified charge is formed in the DISI engine combustion chamber with an elaborated designed shape of piston head and in-cylinder air flow motion.

When fuel spray injected into the combustion chamber in wall-guided DISI engines, the piston top surface can direct the impinging spray towards the spark plug, and at the same time, a high speed air flow with strong swirling and tumbling motions also guide the fuel towards the region around the spark plug. With the strong guiding effects of piston top surface and in-cylinder air motion, an ignitable and stratified mixture where a fuel rich zone surrounded by a region of pure air or exhaust gas at the periphery of the cylinder can be formed near the spark plug of DISI engines.

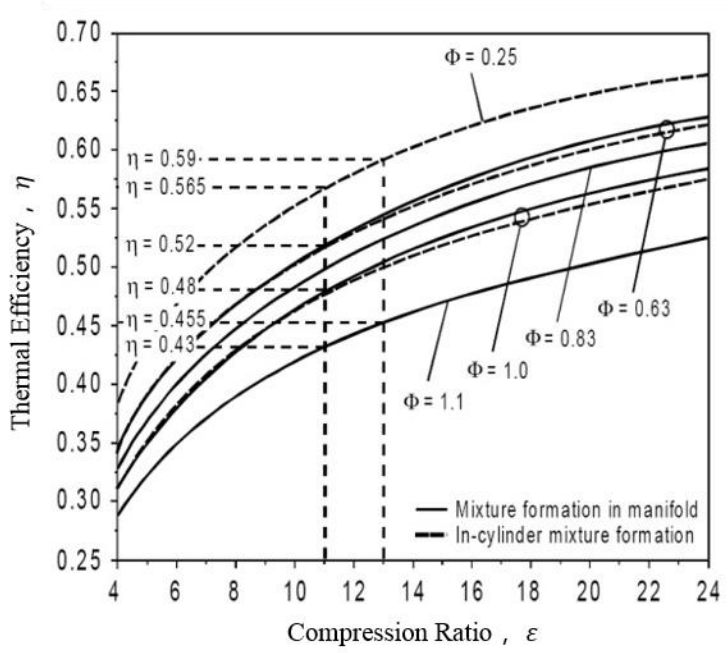

Figure 1.2: Theoretical thermal efficiency of gasoline engines [1-3]

The stratified mixture can bring benefits of reducing thermal losses from the combusted mixture to the cylinder walls. Furthermore, since a less ignitable mixture at the periphery of the cylinder is formed and cylinder temperature is reduced because of the cooling effects of fuel evaporation and the overall lean mixture, the tendency of engine knock is decrease, which allows the increase of compression ratio in DISI engines. Another benefit of using stratified and lean mixture in DISI engine is that the isentropic exponent of the mixture is higher, which also helps for the increase of thermal efficiency as shown in Figure 1.2.

1.2.2 Particulate Matter Emission

Typically, particulate matter emissions from engines can be divided into two different categories solid (such as: ash or carbon particles) and volatile components (such as liquid droplets or fuel vapor), and typical composition of engine-out particulate matters is presented in Figure 1.3. The solid particles are mainly agglomerated carbonaceous particles, also can be called as soot, and the

soot is usually formed by the combustion of fuel vapors/air mixture in locally rich regions in engines. Both organic compounds (such as unburnt hydrocarbons) and inorganic compounds (such as sulfur dioxide and sulfuric acid) can be absorbed upon and attached on those small solid particles to form larger particle parcels. Also, a small portion of the fuel vapor and some atomized or evaporated lubricant oil can escape the oxidation/combustion process and form particulate emissions in the engine-out exhaust gas [9-11].

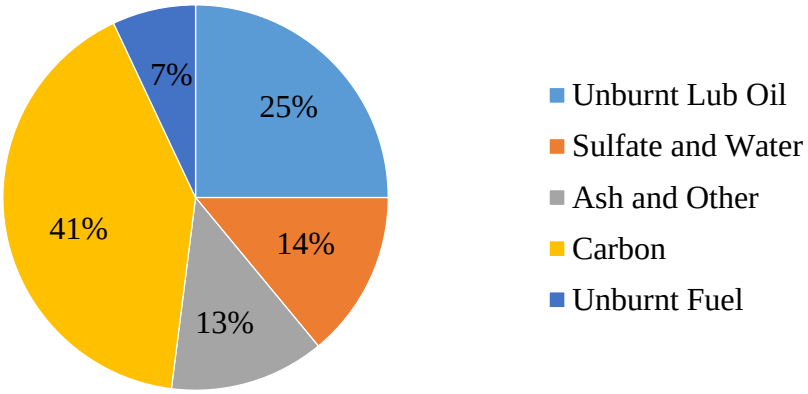

Figure 1.3: Typical compositions of Engine-out PM emissions [9].

The particle size in engine-out exhaust gas distributes as a tri-modal; and the particle sizes ranges from nanometers to microns as shown in Figure 1.4 [9]. Based on the size range of engine-out particles, three different modes of particles (nuclei, accumulation and coarse model) are found in the engine exhaust. In the accumulation mode, the typical diameter of the particles is in the range of 0.1 - 0.3 μm. And the main composition of particulate in this mode is soot and its adsorbed volatile materials; while in the nuclei mode, the diameter of particles ranges from 0.005 to 0.05 μm. Particles in nuclei mode are usually volatile organic or sulfur compounds in the nuclei model, and may also include solid carbon and metal compounds. Typically, 1-20% of the particle mass is in the nuclei mode, which contributes more than 90% of the particle number of engine-out particulate matters. In DISI engines, most of the engine-out particles are in the nuclei model within the

diameters ranging from 0.005 μm to 0.5 μm. Therefore, the quantity of particulate matters from DISI engines is much larger than that from diesel engines, although the total mass of PM is smaller than diesel engines.

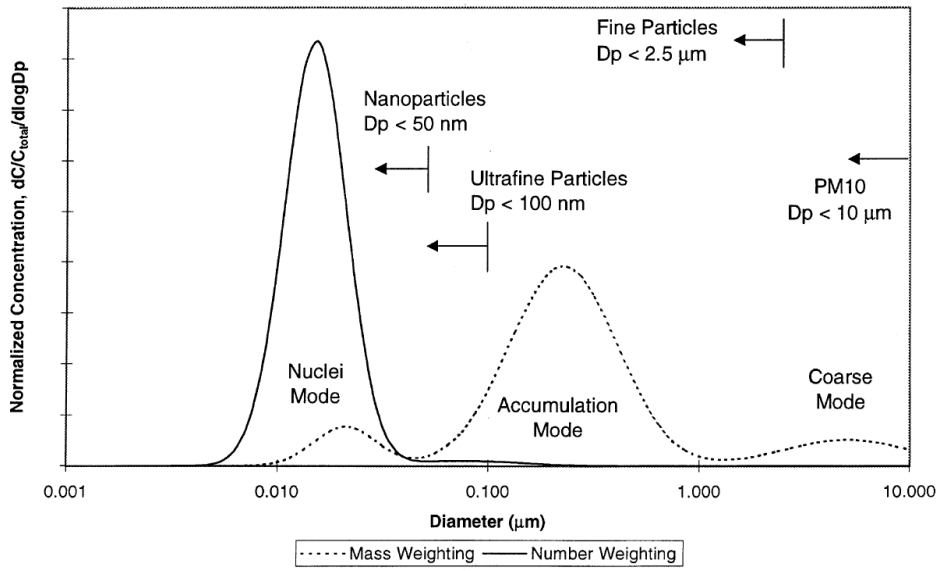

Figure 1.4: Typical size distribution of engine-out PM emissions [9].

1.2.3 Technical Challenges and Research Gap

As the DISI engine technology becomes more and more widespread in the automotive industry and the total number of PM emissions from DISI engines is higher than conventional gasoline engines, stringent emissions standards of engine-out PM emissions, taking into account the total number of PM emissions, are proposed as displayed in Table 1.1. For instance, the European emission regulations (Euro VI) specify a particulate number (PN) limit of 6.0×10^{11} particles/km for new vehicles produced after July 2017[17]. However, the test results of DISI engine in a NEDC cycle has shown that engine-out pollutions from the current DISI engines are higher than the standard of the Particulate number in Euro VI emission regulations [17]. Therefore, further efforts

are required to reduce the number of particulate emissions from the DISI engines in order to meet the emission legislations.

Table 1.1: Summary of European and US light-duty vehicle emission legislations.

Emission Legislations	Date	NOx g/km	PM g/km	PN #/km
Euro IV	2005	0.25	0.025	-
Euro V	2009	0.18	0.005	-
Euro VI	2014	0.08	0.0045	6.0×10^{11}
CARB LEV III	2014-2017	0.012	0.0038-0.0019	3.8×10^{12}-1.9×10^{12}

The combustion of the evaporating liquid wall film on the cylinder wall of DISI engines has been proved to be the major source of PM emissions through the reflection index match (RIM) optical measurement technology [11, 12], which is schematically demonstrated in Figure 1.5. However, due the inaccuracy of evaporation and combustion model of the liquid wall in engines, the discrepancy between the numerical predictions and experimental results of the PM and PN emissions from DISI engines are quite large [18]. Thus, the accuracy of the models for the formation of PM in DISI engines caused by the evaporating liquid wall film need to be improved. As the prerequisites of the modeling of PM formation form the liquid wall film in engines, an accurate evaporation models, to be more specific accurate Sherwood numbers, of the liquid wall film are urgently needed.

Research Gap

Despite of many years research on the modeling of the evaporation of liquid wall film in engines, the understanding of its transient characteristics is still limited. The transient effects of the heating and motion of the liquid phase, large variation of thermos-physical properties, and the variation of

relevant transport phenomena in both the liquid and gas phases have not been investigated. Moreover, mass transfer correlations that can accurately represent the transient evaporation process of the liquid wall film in DISI engines and be able to calculate the evaporation process efficiently are still required.

Since both the evaporation time and initial thickness of liquid wall film in DISI engines is quite small, experimental measurements of the evaporation process in engine conditions are quite challenging considering the high temperature, high velocity in-cylinder gas flows in engines, numerical modeling becomes a useful tool to provide insight into the transient characteristics of the evaporation of liquid wall film in engines. Thus, numerical studies on the transient evaporation process of liquid wall film in DISI engine-like conditions are performed; and the mass transfer correlations that can be used to calculate the evaporation mass rate of liquid wall film in DISI engines are developed based on numerical results.

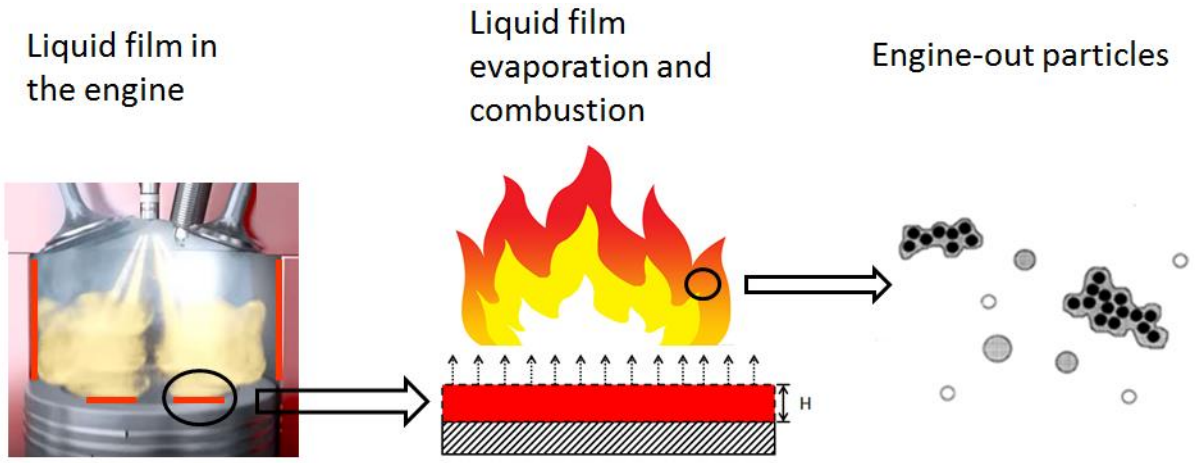

Figure 1.5: Liquid thin wall film as a source of particulate matters of DISI engines.

1.3 Objectives and Scope of the Thesis Research

The major research objectives of this thesis are to:

- provide insight into the evaporation characteristics of the liquid wall film in DISI engine-like flow conditions;
- identify the suitable turbulence model for the direct modeling of the evaporation of liquid wall film in turbulent flow conditions in the range of typical turbulence intensities in DISI engines; and
- develop the mass transfer correlations for the transient evaporation of liquid wall film in DISI engine-like flow conditions.

To achieve these objectives, the whole thesis research is divided into three main stages (stage I, II, III). In stage I, the evaporation of liquid wall film in a stationary gas medium is studied, and three different evaporation boundary conditions (in an infinite space, in a finite space, and with oscillating interfacial vapor in an infinite space) are considered at this stage. The study on the evaporation of liquid wall film in stationary gas medium can help to gain some understanding on the transient evaporation of liquid wall film; and the analytical results obtained in this stage can also serve as benchmark data for the validation of pure species diffusion process of the numerical model. In the second and third stages (stage II, III), numerical study on the evaporation of liquid wall film in laminar and turbulent flows are performed. A two-dimensional, two-phase, transient, non-isothermal, species transport problem representing the evaporation of liquid wall film in DISI engine-like conditions have been developed and studied numerically. The governing equations with their pertinent boundary conditions that mathematically describe the evaporation of liquid wall film are discretized and solved on a Finite Volume Method (FVM) based numerical simulation platform, FLUENT, with its capacity of User Defined Function (UDF) programming and the convenience of providing a framework of multi-phase flow problem. In order to direct simulate the species transport in the turbulent flows over the evaporating liquid wall film, different

turbulence models with near wall modeling methods are examined. The numerical results are validated and verified through comparing with existing analytical and experimental results. Subsequently, numerical study on the evaporation of liquid wall film in DISI engine-like conditions have been performed to characterize its transient evaporation process; and the mass transfer correlations of evaporating liquid wall film are developed.

The thesis is organized as follows: in the current Chapter, a brief overview of DISI engines and the importance of the evaporation of liquid thin wall film on the formation and emission of PM in DISI engines are presented, followed by a description of the objectives and scope of this thesis research. Evaporation models of liquid wall film in engines and the study of the evaporation of liquid wall film through direct numerical simulation are reviewed in Chapter 2. The mathematical model for the evaporation of liquid wall film in DISI engines is described in Chapter 3. The model implementation and numerical techniques involved in the present study are described in Chapter 4. In Chapter 5, results for the transient characteristics and the mass transfer correlations of the evaporating liquid wall film in DISI engine-like conditions are demonstrated. Finally, summary of the present study and some suggestions for the recommendation of future work are described in Chapter 6.

Chapter 2
Literature Review

The evaporation of liquid wall film in engines has attracted numbers of research projects aiming at having a clear understanding on its evaporation characteristics. As numerical simulation is widely used in the engine industry to design the next generation of high-performance, low-emission engines, different types of evaporation models are proposed; and these models can be classified as empirical, analytical and numerical models. A summary of the major evaporation models with their core assumption and methodology of calculating the evaporation rate are listed in Table 2.1.

Table 2.1 Evaporation models of liquid wall film in Engines

Authors	**Core assumptions**				**Evaporation rate calculation**
	Component Of wall film	Flow conditions		Temperature profiles within the wall film	
		Liquid wall film	Gas streams		
Bai *et al.* 1996	Single component	Laminar	Turbulent	3rd polynomial	Semi-empirical correlation

O'Rourke *et al.* 1996	Single component	Laminar	Turbulent	Piecewise linear	Modification of wall function
Han *et al.* 2004					
Foucart *et al.* 1998				Parabolic	Modification of wall function (two categories)
Stanton *et al.* 1998				Piecewise linear	Modification of wall function (wavy)
Descutter *et al.* 2009				3rd polynomial	Modification of wall function (transition)
Zeng *et al.* 2000	Multi-component				Modification of wall function

Torres *et al.* 2006					
Song *et al.* 2015	Single component	Stationary		Transient heating	Mass transfer correlation
Yan *et al.* 2015					

2.1 Evaporation Models in the Engine Industry

2.1.1 Empirical Models

The empirical models for the prediction of the evaporation rate in the turbulent gas stream flowing above the liquid wall film in engines is based on empirical Sherwood number correlations [20,21, 24 - 28], or modified turbulent law of wall with empirical parameters [22,23]. The most general indicator of the evaporation of liquid wall film is the evaporation rate; hence, several attempts have been observed to provide an empirical relation between the evaporation rate of liquid wall film and local evaporating conditions. In addition, in order to model the evaporation rate empirically, factors such as Reynolds number of the gas flows, Schmidt number of the species, interfacial vapor mass fraction and temperature profile within the liquid film are usually considered.

The pioneer work of estimating the evaporation rate of liquid wall film in engines using the empirical mass transfer correlation is reported by Bai and Gosman [20]. With the assumptions that flow condition within the film is laminar and the gas/liquid surface is perfectly flat, the evaporation rate of liquid wall film is predicted using the empirical mass transfer correlation in the form of:

$$\mathrm{Sh}_r = \Phi Re^{1/2} \tag{2.1}$$

$$\Phi = \frac{Sc^{1/2}\left(27.8+75.9\,Sc^{0.036}+657\mathrm{Sc}\right)^{-1/6}}{1+0.94\dot{M}^{1.14}Sc^{0.93}} + \dot{M}Sc \tag{2.2}$$

$$\dot{M} = \frac{\dot{m}_v l_r}{\mu_f Re_r^{1/2}} \tag{2.3}$$

Later, this method is adopted by Stanton and Rutland [27] and the model is extended to study the evaporation of multicomponent wall film. However, the correlations used in these models are developed for two dimensional condensations under forced conditions, which are different from the flow conditions in engines; and validation of these evaporation model are still needed for the application of them into engines.

Another widely used method for the prediction of the evaporation of wall film in engines is based on the one-dimensional species diffusion and modification of turbulent wall functions. Models developed by O'Rourke and Amsden (OA) predict the vaporization of the wall film under turbulent air stream through modifying the standard wall function [22, 23]. In their model, the turbulent diffusivity is considered to vary linearly with the distance from the liquid/gas interface, and the sum of the transport is caused by turbulent diffusion and convection. The evaporation rate is predicted as a function of turbulent species boundary conditions and mass transfer coefficients.

This model provides a framework for the modeling of evaporating wall film in engines, however, the important effects of gaseous temperature on the evaporation of liquid wall film do not include in it. This problem is overcome by Foucart [21], and they develop a wall film evaporation model including the effects of gaseous phase temperature and bulk motion of the liquid wall film induced by evaporation. The expression for the evaporation rate depends on the dominant effects of gas stream (dynamic effects or thermal effects). Afterwards, his methodology is further extended by

Stanton *et al.* [27], and effects of wavy interface on the evaporation of wall film are considered through adding an additional term in the modified wall function in the model. Using the interface roughness method proposed by Sattelmyer *et al*. [28], a constant C, which is a function of the roughness Reynolds number, is introduced into the model to account for the wavy effects.

Since the transition between the fully turbulent sub-layer and viscous laminar sub-layer in the wall of law of the turbulent gas flows is dependent on evaporation rate of the wall film, a flexible transition distance that can reflect the changing of evaporation rate need to be modeled. Descutter *et al.* [29] develop a new wall function for the thermal/species boundary layer using direct numerical simulation (DNS) method, and the new derived wall function is incorporated into a wall film evaporation model using Reynolds Average Navier-Stokes (RANS) turbulence models [30]. However, this model still limited by using a constant distance for the modeling of viscous sublayer and log-law region transition.

Only few models can be found in the open literature for the modeling of the evaporation of multi-component liquid wall film in engines. Torres *et al.* [31] used a discrete approach for the model of both spray development and film evaporation. They generalize the evaporation model of OA [22, 23] to multi-component model through adding the evaporation rate of each component with assumption of same species concentration at different depth of the wall film. Also, Zeng *et al.* [32] propose a continuous thermo-physical evaporation model for the evaporation of multi-component film, in which a third order polynomial curve is employed to model the energy and species transport within the wall film.

Mass transfer correlations are efficient on the calculation of the evaporation rate of liquid wall film, and developing an accurate mass transfer correlation is also one of the major objectives of this thesis research. Therefore, a review on the mass transfer correlations/coefficients is presented in

this section. Based on the physics of the evaporation of liquid wall film, evaporation models and mass transfer correlations can be classified into two major groups according to the regulation physical mechanisms – gaseous phase boundary layer regulated or liquid diffusion regulated.

For gaseous phase boundary layer regulated models, the evaporation of liquid wall film can be considered as the movement of molecules from the gas/liquid interface into the gas stream flowing above the film. Momentum temperature and species concentration boundary layers are developed in the gas flows over the evaporating liquid wall film and the characteristic of these boundary layers can determine the evaporation process of the liquid wall film. In the boundary layer regulated mechanism, the evaporation rate is sensitive to the velocities or turbulence intensities of the gas streams. In addition, the evaporation rate of liquid wall film is limited by the molecular, turbulent diffusion and the saturation state at the gas/liquid interface.

The mass transfer coefficient of air regulated evaporating wall film is a function of transport conditions in the air flows and a function of the molecular diffusion characteristics (i.e. Schmidt number) of the hydrocarbon in the vapor phase. The velocity profile, which can determine the velocity gradient over the evaporating liquid wall film, is critical in controlling the evaporation rate. Two most frequently used velocity profiles are 1) the logarithmic velocity profile and 2) power law velocity profile. In the logarithmic velocity profile, the velocity ratio at two heights is proportional to the logarithm of the height ratio, while in the power law velocity profile, the velocity ratio is proportional to the height ratio to some power [35 - 37].

Based on the assumption that the wind velocity profile follows a power law, Sutton *et al.* propose a correlation for the air boundary regulated evaporating liquid, in which the effects of turbulence level, diffusivity of particular evaporating species and the area of the liquid wall film are considered [35]. Similarly, Mackay *et al.* developed a mass transfer correlation under the same

assumption of power law velocity, and the constants in the correlations are chosen based on experimental results [36]. Later, Yang and Wang take the effects of wavy surface in to consideration, and they have found that the formation and breaking waves greatly increases evaporation rates [37].

For the liquid diffusion regulated model, the evaporation mass rate is regulated by the species diffusion within the liquid film, and the evaporation time and temperature are important. However, the velocity and turbulence level of the gas flows and the length of the liquid wall film do not have significant effects on the evaporation of liquid wall film. A curve fitting methodology is adopted by Fingas *et al.* [38] to develop the liquid diffusion regulated evaporation model for the evaporating oil films in atmosphere conditions without air motions. Their results show that Oils and diesel-like fuels evaporate at two distinct types; the evaporation of oil film flows is a logarithmic function of time and the evaporation of diesel-like fuel is a square root function of time. As the volatile components is able to diffuse in to a thicker liquid wall film, a thickness correction factor is also developed. Further, Fingas *et al.* [39] explain that the overall logarithmic/square root appearance can be attributed to the components evaporating at different linear rates. The evaporation of oils having more than 7 components can be modelled as a logarithmic equation with evaporation time; while oils with 3 to 7 components follows a square root equation with time increasing. Due to the diffusion resistance, the evaporation rate and interfacial mass concentration change greatly with time, Katsuhiro *et al.* [40] developed an evaporating model for evaporating gasoline through experimental measurement and empirically derived constant for each component. It is found that the vapor pressure, the evaporation process can be modeled as a function of weight loss rate; and the evaporation mass can be described by a logarithm function of time in a liquid wall film with five different components.

2.1.2 Analytical Models

The transport phenomena involved in the evaporation of liquid wall film in DISI engines include mass, momentum, species and energy transport in both the liquid and gas phase. All these transport phenomena can be mathematically described by fundamental conservation laws. However, it is infeasible to solve all these equations in the engine design software due to the requirement of grids for turbulence simulation and the rigorous requirement of grids near the gas/liquid interface. Thus, analytical models with certain level of assumptions are usually adopted to predict the evaporation rate of liquid wall film in commercial engine design software.

Due to the strong coupling between heat and mass transfer, the temperature profile within the liquid wall film, especially the gas/liquid interfacial temperature of the liquid wall film, is crucial for the accurate calculation of evaporation rate. Song *et al.* propose an analytical formulation of energy transfer (the variation of temperature profiles) within wall film in DISI engine [33]. An effective interface temperature method is introduced to facilitate the solution process, which is usually used in the modeling of evaporating fuel droplets in engines. Using the same methodology, Yan *et al.* [34] developed a one-dimensional evaporation model for liquid wall film under turbulence flow conditions in DISI engine-like conditions. However, the liquid wall film is assumed to be stationary and the evaporation rate of wall film is estimated by mass transfer correlations based on the assumption of heat and mass transfer analogy and constant Lewis number (equals to one). As the properties varies significantly within the boundary layer over the evaporating liquid wall film and strongly depends on the local temperature and vapor mass fractions, the assumption of constant Lewis number is not validated anymore. Furthermore, the mass transfer correlations used in the existing analytical model only valid for the steady state conditions. Therefore, accurate mass transfer correlations account for the variation of thermos-

physical properties during the transient evaporation process of liquid wall film is needed, which is also one of the major objectives of this thesis study.

2.2 Numerical Simulation of Evaporating Liquid Wall Film

One of the important issues on the direct numerical simulation of the evaporation of liquid wall film under high temperature air streams is the effects of evaporating vapor on the fluid dynamics of the gas flows. Usually, there are two main evaporation mechanisms that are frequently used in the numerical study of the evaporation of liquid wall film. The first mechanism is diffusion through Stagnant Film (DTSF), in which fluid dynamics of the gas flow is affected by the evaporating vapors; and this effect is also known as "blowing effects". The second mechanism is Equi-Molal Counter Diffusion (EMCD), in which the movement of vapor can be balanced by the movement of air in the counter-direction; therefore, the evaporating vapor has no effects on the fluid dynamics of gas flows. The effects of evaporating vapor on the gas flows can be represented by including a source term in the continuity equation in DTSF model; and the diffusion velocity can be obtained explicitly. Therefore, this method is also adopted in this study for the direct simulation of evaporating liquid film in DISI engine-like conditions.

2.2.1 Interface Reconstruction

The gas/liquid interface is crucial for the study of the evaporation of liquid wall film in convective environment, which directly determines the actual interfacial area available for interphase heat and mass exchange. Capturing the gas/liquid interface is quite challenging due to its inherent nature of dynamic and arbitrary. Generally, formulations for the interface tracking or reconstruction are based on two methods: moving grids or moving grids. For the moving grid methodology, the interface grid moves with the fluids and the interface are tracked using Lagrangian algorithm [42,

43]. The application of boundary conditions on the interface is relatively simple, since the interfacial grids are usually directly resolved. However, as an explicit method, the moving grid interface tracking/reconstruction algorithm requires small time steps to ensure the stability. For the fixed grids formulations, the gas/liquid interface can be reconstructed by solving a transport equation of the volume fraction of cell occupied by the liquid, which is also called Volume of Fluid (VOF) method. Apart from the VOF method, commonly employed approaches also include the Front Tracking (FT), and Level Set (LS) methods. Among these gas/liquid interface reconstruction models, the VOF model provides a convenient framework for the numerical study of evaporation form free surface flows. Various interface reconstruction algorithms are needed to construct the accurate sharp interface for the free surface flows. The simple but popular interface reconstructed algorithm is the simple line interface calculation (SLIC) of Noh *et al.* [44] or the SOLA-VOF algorithm of Hirt *et al.* [45]. More accurate reconstruction methods, as developed by Gueyffier *et al*. [46] and Rider *et al*. [47], reconstruct the gas/liquid interface using the Piecewise Linear Interface Calculation (PLIC), which will also be used in the present study.

2.2.2 Evaporation under Laminar Gas Stream

Generally, heat and mass transfer are strongly coupled for the evaporation of liquid wall film in a convective environment; and local temperature and species concentration, especially the temperature and concentration gradient on the gas/liquid interface need to be resolved in the numerical study. Thus, implementing appropriate interfacial boundary conditions for the purpose of calculating the evaporation rate of the liquid wall film is of significant importance.

Since the heat flux discontinuity is caused by the entropy difference in the liquid and gas phase, the evaporation rate of wall film can be evaluated by the energy jump condition and the implementation of interphase mass transfer is achieved by applying energy balance equation on

the gas/liquid interface and the evaporation rate is determined by the net heat flux transferred from the high temperature gas flows to the liquid film. Similar approach can be adopted to study various phase changing problem accounting in different industry applications after some tiny modifications.

Since the evaporation rate of liquid film can be directly determined by the species gradient near the gas/liquid interface, Strotos *et al*. [81] use a simplified form of Fick's law to evaluate the evaporation rate of liquid film with the assumption that thermodynamic equilibrium is obtained on the gas/liquid interface. Later, this method is employed by Banerjee [82] to study the evaporation of methanol and the mixture of ethanol/isooctane in an inclined channel. Then this methodology is extended to three-dimensional by Banerjee *et al.* [83, 84] and Schlottke *et al.* [85] to study the evaporating gasoline in a channel and the evaporation of droplet under convective environment. Also, mass transfer correlation for the evaporation of liquid film is derived based on the method as reported by J. B. Haelssig $et\ al.$ [98]. However, the liquid is assumed to be single component in these, and the effects of multicomponent species transport are ignored.

The species transport phenomena are much more complicated, phenomena like diffusion barrier, osmotic diffusion and reverse diffusion may exist, which make the modeling and simulation of multi-component evaporating liquid film fairy complicated. Based on the VOF multiphase model, R. Banerjee *et al.* [82] investigated the evaporation of a multicomponent liquid film in an inclined channel. The contribution of evaporating vapor is represented by including the source terms in the conservation equations of mass, momentum, energy and species concentrations. In addition, the transport of each species is tracked through solving the species transport equation in both phases. With the same assumptions that Fick's law applies and the effect of thermal diffusion (Soret effect) is able to be neglected, the modified Fick's law is employed to model the diffusion of evaporating

vapors laminar conditions are investigated by Jan B. Haelssig *et al*. [98] and Baumann *et al.* [99]. Another major group model for the multicomponent mass transport modeling is based on the Maxwell–Stefan equation, such as Cui *et al*. [100]. Although the Maxwell–Stefan equation is able to model diffusional interaction in a multicomponent system more clearly, the modified Fick's law is easier to be implemented into the numerical simulation platform with acceptable accuracy for the track of minority components, which will also be employed in this research.

Other methods like kinetic theory approximation, ghost Fluid technique and continuum field representation of source term are also proposed and implemented in the numerical software to simulate the phase changing problem. The methodology of predicting evaporation rate through solving the species transport equation and evaluating the evaporation rate by species gradient on the gas/liquid interface can explicitly reflect the evaporation physics, which will also be employed in the present research.

2.2.3 Evaporation under Turbulent Gas Stream

In the previous two sections, two key techniques involved in the direct simulation of evaporating liquid film are reviewed. A brief review of the direct simulation of evaporating wall film in turbulent flow conditions is presented in this section.

Effects of turbulent mixing are crucial for the species transport in the both liquid and gas phases, which can enhance the evaporation rate significantly and can directly affect the evaporation rate because of the turbulent mixing effects. To include this effect, R. Banerjee *et al.* [84] study the evaporation of single component moving liquid film in a turbulent isothermal system with constant gas-phase molecular viscosity and species diffusivity. The RNG $k-\varepsilon$ model is used in their numerical model to improve the accuracy of the results and the low Reynolds number effects are included through including a damping function in the turbulence kinetic (k) and dissipation rate

(ε) functions. The same turbulence model is also employed by Hassanvand *et al.* [41] to study the unsteady multiphase turbulent flow with interphase heat and mass exchange. The shear stress transport (SST) $k-\omega$ turbulent model, which can model the interface turbulent effects more accurately, was also applied in this problem by Cui *et al.* [100]. The gas flows near the gas/liquid interface is crucial for the correct modeling evaporation of liquid wall film under turbulent gas flows, since the gradients of the species concentration can directly relate to the evaporation rate of liquid wall film. Different types of turbulent models with near wall treatment method have been proposed in the literature and these models are evaluated in Section 5.3.1 of this thesis.

2.2.4 Evaporation of Liquid Wall Film with Wavy Interface

Because of the strong interaction between the gas and liquid at the interface and stephan velocity caused by the blowing effects of evaporation, waves are formed on the gas/liquid interface and this wavy effect is also considered in some mathematical models. For an early trial, Kanatani *et al.* [101] proposed a model to consider the wavy effects, and a long-wave approximation is used in the governing equations of the liquid phase. The linear stability of the film is investigated in their study; and their results show that the maximum wave numbers is a function of film thickness. Similarly, Burelbach *et al.* [102] develop a long-wave evolution equation for the arbitrarily developing of the gas/liquid interface, which govern the nonlinear stability of evaporating interface. Gerendas *et al.* [103] use both experimentally and numerically method to study the evaporation of water and ethanol mixture films. Although the formation of waves on the gas/liquid interface may increase the effective evaporation area which may lead to higher evaporation rate, the effects of wavy surface can be ignore for extremely thin liquid film as presented in the DISI engines [28].

2.3 Mass Transfer Correlations

Different mass transfer correlations are developed to estimate the evaporation rate of liquid wall film in engines. The evaporation models using mass transfer correlations to estimate the evaporation rate in engines is widely used in the engine design software, as the mass transfer correlation can calculate the evaporation rate efficiently given the flow conditions in engines. A summary of the mass transfer correlations used in literature is listed in Table 2.2.

The first group of mass transfer correlations (first three in Table 2.2) is derived based on experimental measurement, but the flow conditions in these experiments are either stagnant or laminar in the gas flows, which are quite different from the flow conditions in engines. Thus, these mass transfer correlations are not considered to be accurate for the estimation of evaporation rate in DISI engines. In the second group of the mass transfer correlations (the remaining correlations in Table 2.2), the Sherwood number correlations are developed based on the similarity between heat and mass transfer. However, the mass transfer correlations developed using this method is only validated for steady mass transfer process, which cannot represent the transient evaporation process of liquid wall film in DISI engines, as the time scale of the evaporation process in DISI engines is quite short (in the order of milliseconds). Furthermore, the Sherwood number correlations derived from heat and mass transfer analogy assume that the thermos-physical properties are constant during the evaporation process, which is not true for the evaporation of liquid wall film in DISI engines, as the gradients of temperature and species concentration is quite large within the thermal and species boundary layers over the evaporating liquid wall film.

Table 2.2 Mass transfer correlations of evaporating liquid wall film in engines

Authors	**Core assumptions**	**Correlations**
Brutsaert, *et al.* 1982	Air boundary regulated	$k_m = 0.0292U^{0.78}X^{-0.78}Sc^{-0.67}$
Finga *et al.* 1997	Liquid diffusion regulated	$E\% = [0.165(\%D) + 0.045(T-15)]\ln(t)$ $E\% = [0.0254(\%D) + 0.01(T-15)]\sqrt{t}$
Bai *et al.* 1996	Sherwood number and mass transfer coefficient determined	$Sh_r = \Phi Re_r^{1/2}, \Phi = \frac{\Psi}{1+0.94\dot{M}^{1.14}Sc^{0.93}} + \dot{M}Sc$
O'Rourke, *et al.* 1996	a) Heat and mass transfer analogy b) Constant thermal physical properties c) Lewis number equal to one	$Sh_x = \begin{cases} 0.332Re_x^{1/2}Sc^{1/3}, & Re_x < 2500, \\ & 0.6 < Sc < 50 \\ 0.0296Re_x^{4/5}Sc^{1/3}, & Re_x > 2500, \\ & 0.6 < Sc < 50 \end{cases}$
Woschni *et al.* 2002		$h = 0.013D^{-0.2}P^{0.8}T^{-0.55}\left[c_1c_m + c_2\frac{V_hT_1}{P_1V_1}(P - P_0)\right]^{0.8}$ (heat transfer coefficient)
Song *et al.* 2015		$Sh = 0.0296Re^{0.8}Sc^{0.3}$
Yan *et al.* 2015		$Sh = 0.0287Re^{0.8}Sc^{0.6}$

2.4 Summary

From the aforementioned literature review, it is clear that the evolution of the modeling of evaporating liquid wall film is increasingly complex with the advancement of engine technologies. However, accurate and efficient mass transfer correlations that can represent the transient evaporation process of liquid wall film in DISI engine-like conditions are still required by the engine industry. Due to capability of dealing with the complicated gas flow conditions in engines and the strong gas/liquid interaction between the gas flow and the evaporating liquid wall film, the direct simulation of evaporating liquid wall film is considered to be an effective way to investigate the transient evaporation process of liquid wall film in DISI engine-like flow conditions.

Chapter 3
Model Formulation

The evaporation of liquid wall film in DISI engines is synonymous to the evaporation from a plane surface under high temperature gas flows. The transport of vapor species is boosted by the convective effects of the gas flows. Therefore, the evaporation of liquid wall film can be characterized by subjecting discrete sample of liquid wall film in a high temperature gas stream as shown in Figure 3.1, in which the liquid wall film evaporates under a high temperature gas stream with evaporation rate per unit area denoted as $\dot{m}''$. Moreover, the flow direction in this study is considered to be parallel to surface of the liquid wall film, since the velocity magnitude in the tangential direction of the gas flow in DISI engines is much larger than the radial direction due to the large in-cylinder swirling motions [106, 107].

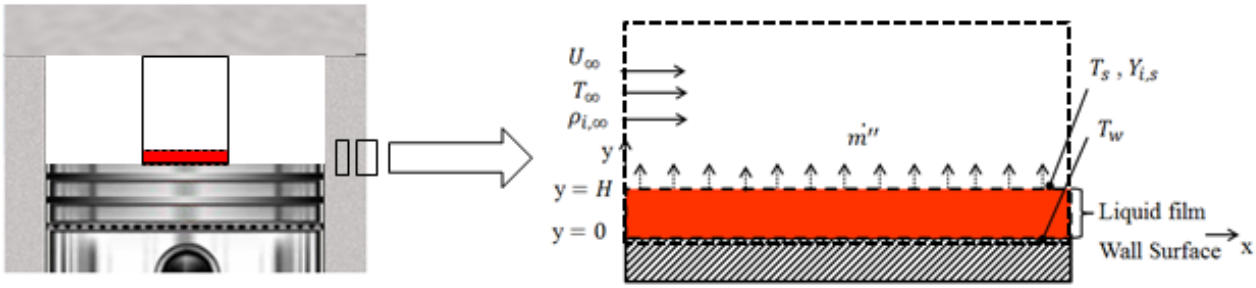

(a) (b)

Figure 3.1: A schematic of the evaporating liquid wall film in DISI engine-like flow conditions.

The flow conditions in the engines are quite complex and varies with the engine speeds and the design of the intake port. Also, the turbulence intensities are depended on the engine speeds, engine output loads and other operating parameters such as ignition timing, intake and exhaust valves overlap [109-111]. The velocity of gas stream in the range from 5m/s to 40 m/s corresponding to the Reynolds number at the inlet in the range from 8.5×10^3 to 6.8×10^4 is studied to examine

the effects of convective motion in the gas flows on the evaporation of liquid wall film in DISI engines. As the variation of the thickness of the liquid wall film at different locations of the wall surface is near negligible, a liquid wall film with constant initial film thickness is introduced on the wall surface as displayed in Figure 3.1 (b). The composition of gasoline used in DISI engines is also quite completed, which even changes from different sources. Here, the n-octane is used as a surrogate of the gasoline, since the main component in gasoline is octane. Typical parameters for the evaporation of liquid wall film in DISI engine-like conditions can be found in Table 3.1.

Table 3.1: Typical parameters of the evaporating liquid wall film in DISI engines

Parameters	Parameter Range
Reynolds number of the gas flow [106-108]	$8.5 \times 10^3 - 6.8 \times 10^4$
Turbulence intensity / % [109-111]	5 - 25
Gas phase temperature/ K [2-5, 105]	300 – 2000
Gas phase pressure/ MPa [2-5, 105]	0.9 –7
Wall surface temperature/ K [2-5, 105]	400 – 500
Initial wall film thickness/ μm [12, 112,113]	10 – 250

Physically, the evaporation of liquid wall film in DISI engines is driven by energy transferred from the high temperature gas stream, $\dot{Q}_g$, and high temperature cylinder wall, $\dot{Q}_w$, to the liquid wall film. After applying energy conservation at the gas/liquid interface, energy transferred from the high temperature air stream and wall surface to the liquid wall film is consumed by liquid film heating $\dot{Q}_l$ and enthalpy difference caused for evaporation (phase change); and the energy balance on the gas/liquid interface can be generally expressed as:

$$\dot{Q}_g + \dot{Q}_l - \sum_{i=1}^{n} \dot{m}_i H_{\mathrm{fg,i}} = 0 \quad (3.1)$$

The mathematical model of the evaporating liquid wall film in DISI engine-like conditions need to consider the multiphase flow, transient liquid motion and heating, blowing effects, surface tension (for deformed gas/liquid interface), variable thermo-physical properties and various gaseous flow conditions (i.e. turbulence flows with different turbulence intensities and oscillating boundary conditions). Due to the advantage of providing a framework of multi-phase problem with sharp gas/liquid interface, the VOF multiphase approach with the PLIC interface reconstruction algorithm is used in this study as the platform of the modeling of the multi-phase problem.

In this Chapter, the evaporation model of liquid wall film in DISI engine-like conditions is presented. Firstly, the necessary assumptions for the simplification of the evaporation model are shown followed by the description of governing equations and their pertinent initial and boundary conditions. Afterwards, the mixing law of the thermo-physical material properties related to local temperature and mass concentration are described. Finally, a short summary of the governing equations is displayed.

3.1 Assumptions

Without losing the major physical characteristics of the evaporating liquid wall film in DISI engine-like conditions, some major assumptions invoked in the model formulation are summarized as follows:

i. The vapor and carrier gas (air) forms an idea gas mixture.
ii. Thermodynamic equilibrium is obtained at the wall film /air interface, and the solubility of the vapor and air in the liquid wall film is negligible.

iii. The top surface of wall film is flat for the study of the transport phenomena of the evaporating liquid wall film; and the liquid wall film directly contact with the wall surface.

iv. The effect of viscous heat dissipation is ignored for the evaporating liquid wall film in the convective environment.

v. The Soret effect and Dufour effect are negligible.

These assumptions are easily to be justified and these effects are usually ignored for the derivation of mass transfer correlation in most of the studies [81-86].

3.2 Govening Equations

Due to the special requirement of simulating a sharp liquid/gas interface and the interphase heat/mass transfer simultaneously, the evaporation model developed in this study is based on the framework of VOF multi-phase model for its convenience of providing an accurate and sharp interface. The one set of conservation equations of mass, momentum, energy and species are employed and solved for the simulation of multi-phase flow problem with interphase heat and mass transfer in the framework of VOF model, and the standard Reynold averaged Naiver-Stokes equations with near wall resolving treatment are adopted for the modeling of turbulence flow.

3.2.1 Conservation of Mass

The mass conservation equation on the VOF framework is defined as:

$$\frac{\partial}{\partial t}(\rho) + \nabla \cdot \left(\rho \vec{U}\right) = 0 \tag{3.2}$$

where ρ represents the volume fraction averaged density, given by $\rho = \alpha_l \rho_l + \left(1 - \alpha_g\right)\rho_g$ with α_l representing the volume fraction of the liquid phase. The velocity is denoted by $\vec{U}$. For turbulent flow conditions, the velocity $\vec{U}$ is the time-average velocity [114], and the over bar representing

the time average is omitted for the consistency of the governing equation for laminar and turbulent flows.

3.2.2 Conservation of Momentum

The momentum conservation equation, on the framework of VOF model, is defined as:

$$\frac{\partial}{\partial t}\left(\rho\vec{U}\right) + \nabla\cdot\left(\rho\vec{U}\vec{U}\right) \;=\; -\nabla P + \;\nabla\cdot(\tau) + B + S_M \tag{3.3}$$

where, τ and B are the viscous forces and body forces, respectively; and P represents the pressure. The body force in this study only includes the gravity force. In general, there are two possible methods to deal with the two-phase liquid/gas flow problem, namely, one fluid approach and two fluid approach. In the one fluid approach, the gas and liquid velocity are considered equally; and a single set of momentum equation is solved in the computational domain for the mixture velocity, which is shared among two phases. Conversely, for the two-fluid method, two sets of momentum equations representing the flow fields of two different phases are solved separately. In addition, the interfacial momentum source term or an expression for the velocity difference between two phases is specified in the momentum equation in the two-fluid method. In the present study, the one-fluid approach is adopted for the convenience of providing a sharp gas/liquid interface.

For laminar flow conditions, the viscous stress τ, taking the example of in the gas phase, can be modeled as:

$$\tau = \;\mu_{g,m}\nabla\vec{U} \tag{3.4}$$

where $\mu_{g,m}$ is the molecular dynamic viscosity in the gas phase, which is a function of local temperature and species concentration, as will be described in Section 3.4.

Similarly, the viscous stress τ for the turbulent flows is calculated by

$$\tau = \left(\mu_{g,m} + \mu_{g,t}\right)\nabla\vec{U} \tag{3.5}$$

where $\mu_{g,t}$ represents the turbulent viscosity in the gas phases. Based on Boussinesq approximation, the Reynolds stress is related to the local velocity gradients by an eddy viscosity μ_t, which is calculated from the turbulence scalar quantities (k and ε or k and ω)) as shown in Equation (3.6) and (3.7).

$$\mu_t = \rho f_\mu C_\mu \frac{k^2}{\varepsilon} \tag{3.6}$$

$$\mu_t = \alpha^* \frac{\rho k}{\omega} \tag{3.7}$$

Since the interphase mass transfer process mainly occurs in the region adjacent to the gas/liquid interface, the turbulence viscosity in the region close to the interface need to be resolved. A comparison has been done with different near wall turbulent viscosity resolve methodologies, a) different low-Reynolds number $k-\varepsilon$ models [118-126], b) $k-\varepsilon$ turbulence model family with enhanced wall treatment [127-129], and c.) SST $k-\omega$ model [130]. Also, four different the low Reynolds number $k-\varepsilon$ models are evaluated to choose the best low Reynolds number turbulence model for the near wall flow modeling.

Turbulence models

Details of the low Reynolds turbulence models are provided in the following section. For the comparison of the $k-\varepsilon$ turbulence model family with enhanced near wall treatment, three different types of $k-\varepsilon$ turbulence models, 1) standard [127], 2) RNG [128] and 3) realizable model are compared [129]. The RNG $k-\varepsilon$ model is derived from the instantaneous Naiver-Strokes equations, and the "renormalization group" (RNG) method is used for the derivation. Different from the standard $k-\varepsilon$ model, the RNG $k-\varepsilon$ model can provide an analytically-

derived differential formulate for calculation of effective viscosity that include the effects of low-Reynolds effects with proper treatment of the near wall regions (fine meshes and special wall functions). Furthermore, the RNG model has an additional term in the $\varepsilon -$ equation, which can improve the accuracy of the rapid strained flows. For the realizable $k - \varepsilon$ model certain mathematical constraints on the Reynolds stresses are satisfied, which ensure the model to be consistent with the physics of turbulent flows. Furthermore, the dissipation rate, ε, has been derived from the solution of the transport of the fluctuation of mean-square vorticity. For the SST $k -$ ω model, the standard $k -$ ω model is used in the near wall region, which can model the low-Reynolds effects; and $k -$ ε model is employed in the region far from the wall. A blending function is developed in the SST $k -$ ω model to combine these two models together, which is activate the standard $k -$ ω model in the near wall region and activate the transformed $k -$ ε model in the region far from the wall. Furthermore, a cross-diffusion term is introduced in the standard $k -$ ε model, as it has been transformed into equation based on k and ω for the fully resolve of flows in the near wall region.

Low Reynolds number $k - \varepsilon$ model

For the low Reynolds number $k - \varepsilon$ model the turbulence kinetic energy , k, and dissipation rate , ε, are governed by:

$$\frac{\partial \rho k}{\partial t} + \frac{\partial (\rho k U_j)}{\partial x_j} = \frac{\partial}{\partial x_j}\left[\left(\mu + \frac{\mu_t}{\sigma_k}\right)\frac{\partial k}{\partial x_j}\right] + G_k - \rho\bar{\varepsilon} \tag{3.8}$$

$$\frac{\partial \rho \varepsilon}{\partial t} + \frac{\partial (\rho \varepsilon U_j)}{\partial x_j} = \frac{\partial}{\partial x_j}\left(\left(\mu + \frac{\mu_t}{\sigma_\varepsilon}\right)\frac{\partial \varepsilon}{\partial x_j}\right) + f_1 C_1 \frac{\varepsilon}{k} G_k - \rho f_2 C_2 \frac{\varepsilon^2}{k} + E \tag{3.9}$$

where, $G_k = \mu_t \left(\frac{\partial U_i}{\partial x_j} + \frac{\partial U_j}{\partial x_i}\right)\frac{\partial U_j}{\partial x_i}$ is the production of turbulence kinetic energy, and $\bar{\varepsilon} = \varepsilon + D$. $C_\mu, C_1, C_2, \sigma_k$ and σ_ε are the same to the conventional $k - \varepsilon$ model. The damping functions f_μ, f_1 and f_2 and the D and E terms are used to resolve the turbulence quantities in the near wall region. The detailed physical meaning and the criteria for examining the validity of these damping functions have been performed in the reference [116 - 129]. Here, the four low Reynolds number $k - \varepsilon$ models are listed in the Table 3.2, Table 3.3 and Table 3.4.

Table 3.2: Numerical values for the constants $C_\mu, C_1, C_2, \sigma_k$ and σ_ε for low Reynolds number $k - \varepsilon$ model

Researchers	Model	C_μ	C_1	C_2	σ_k	σ_ε
Lam and Bremhorst [119]	LB	0.09	1.44	1.92	1.0	1.3
Launder and Sharma [120]	LS	0.09	1.44	1.92	1.0	1.3
Yang and Shih [125]	YS	0.09	1.44	1.92	1.0	1.3
Abe, Kondoh and Nagano [121, 126]	AKN	0.09	1.5	1.9	1.4	1.4

Table 3.3: Summary of damping functions f_μ, f_1 and f_2 for low Reynolds number $k-\varepsilon$ model

Model	f_μ	f_1	f_2
LB	$\dfrac{[1-\exp(-0.0165Re_T)]^2}{[1+20.5/Re_y]}$	$1+\left(0.005/f_\mu\right)^3$	$1-\exp\left(-Re_T{}^2\right)$
LS	$\exp[-3.4/(1+Re_T/50)^2]$	1.0	$1-0.3\exp\left(-Re_T{}^2\right)$
YS	$\dfrac{\left(1+1/\sqrt{Re_T}\right)}{\left[1-\exp\left(aRe_y+bRe_y{}^3+cRe_y{}^5\right)\right]^{1/2}}$	$\dfrac{\sqrt{Re_T}}{1+\sqrt{Re_T}}$	$\dfrac{\sqrt{Re_T}}{1+\sqrt{Re_T}}$
AKN	$\dfrac{\left\{1+5.0/Re_T{}^{3/4}\exp[-(Re_T/200)^2]\right\}}{[1-\exp(-Re_\varepsilon/14)]^2}$	1.0	$\dfrac{\{1-0.3\exp[-(Re_T/6.5)^2]\}}{[1-(Re_\varepsilon/3.1)]^2}$

Note：$a=-1.5\times10^{-4}$, $b=-5.0\times10^{-7}$, $c=-1.0\times10^{-10}$.

Table 3.4: Summary of *D* and *E* terms, interfacial boundary conditions for k and ε in the for low Reynolds number $k-\varepsilon$ model

Model	D	E	Boundary conditions for k and ε
LB	0	0	$k=0, \frac{\partial \varepsilon}{\partial y}=0$
LS	$2v\left(\frac{\partial \sqrt{k}}{\partial y}\right)$	$2\mu v_t\left(\frac{\partial^2 U}{\partial y^2}\right)^2$	$k=\varepsilon=0$
YS	0	$\mu v_t\left(\frac{\partial^2 U}{\partial y^2}\right)^2$	$k=0, \varepsilon=2v\left(\frac{\partial^2 k}{\partial y^2}\right)$
AKN	0	0	$k=0, \varepsilon=2v\left(\frac{\partial^2 k}{\partial y^2}\right)$

Note: $Re_T=\frac{\rho k^2}{\mu\varepsilon}$; $Re_y=\frac{\rho\sqrt{k}y}{\mu}$; $R_\varepsilon=\frac{\rho\eta^3(\mu\varepsilon/\rho)^{1/4}y}{\mu}$.

RNG $k-\varepsilon$ model

The model equations of the RNG $k-\varepsilon$ model is:

$$\frac{\partial \rho k}{\partial t}+\frac{\partial(\rho U_j k)}{\partial x_j}=\frac{\partial}{\partial x_j}\left(\alpha_k \mu_{\text{eff}}\frac{\partial k}{\partial x_j}\right)+G_k-\rho\varepsilon \tag{3.10}$$

$$\frac{\partial \rho \varepsilon}{\partial t}+\frac{\partial(\rho U_j \varepsilon)}{\partial x_j}=\frac{\partial}{\partial x_j}\left(\alpha_\varepsilon \mu_{\text{eff}}\frac{\partial \varepsilon}{\partial x_j}\right)+C_{1\varepsilon}\frac{\varepsilon}{k}G_k-\rho C_{2\varepsilon}\frac{\varepsilon^2}{k}-R_\varepsilon \tag{3.11}$$

where $G_k=-\rho\overline{u_i'u_j'}\frac{\partial U_j}{\partial x_i}$ corresponding to production of turbulent kinetic energy caused by the gradients of mean velocity. The main difference between the RNG k $-\varepsilon$ model and the standard

k − ε model is the R_ε term, which adjust the value of turbulence viscosity based on the low, medium or high strain rates. The model constants are $C_\mu = 0.0845,\ C_{1\varepsilon} = 1.42, C_{2\varepsilon} = 1.68.$

Realizable $k - \varepsilon$ model

The model equations for the realizable $k - \varepsilon$ model is:

$$\frac{\partial \rho k}{\partial t} + \frac{\partial (\rho k U_j)}{\partial x_j} = \frac{\partial}{\partial x_j}\left[\left(\mu + \frac{\mu_t}{\sigma_k}\right)\frac{\partial k}{\partial x_j}\right] + G_k - \rho\varepsilon \tag{3.12}$$

$$\frac{\partial \rho \varepsilon}{\partial t} + \frac{\partial (\rho \varepsilon U_j)}{\partial x_j} = \frac{\partial}{\partial x_j}\left(\left(\mu + \frac{\mu_t}{\sigma_\varepsilon}\right)\frac{\partial \varepsilon}{\partial x_j}\right) + \rho C_1 S\varepsilon - \rho C_2 \frac{\varepsilon^2}{k + \sqrt{\nu\varepsilon}} \tag{3.13}$$

where $C_1 = max\left[0.43,\ \frac{\eta}{\eta+5}\right], \eta = S\frac{k}{\varepsilon}, S = \sqrt{2S_{i,\mathrm{j}}S_{i,\mathrm{j}}}$, S is the mean rate of strain tensor. The other constants in the model are $C_2 = 1.9, \sigma_k = 1.0, \sigma_\varepsilon = 1.2$. Although the equation for the calculation of turbulent viscosity is the same as the standard $k - \varepsilon$ model, the coefficient C_μ is a function of mean strain rate, and the turbulence fields instead of a constant in the standard $k - \varepsilon$ model.

SST $k - \omega$ model

The turbulent kinetic energy and specific turbulent dissipation rate transport equation in shear stress transport (SST) $k - \omega$ model can be written as

$$\frac{\partial \rho k}{\partial t} + \frac{\partial (\rho k U_j)}{\partial x_j} = \frac{\partial}{\partial x_j}\left[\left(\mu + \frac{\mu_t}{\sigma_k}\right)\frac{\partial k}{\partial x_j}\right] + G_k - Y_k \tag{3.14}$$

$$\frac{\partial \rho \omega}{\partial t} + \frac{\partial (\rho \omega U_j)}{\partial x_j} = \frac{\partial}{\partial x_j}\left[\left(\mu + \frac{\mu_t}{\sigma_\omega}\right)\frac{\partial \omega}{\partial x_j}\right] + G_\omega - Y_\omega + D_\omega \tag{3.15}$$

σ_k and σ_ω in the SST $k - \omega$ model is the turbulent Prandtl number for k and ω. G_ω represents the production of ω, Y_k corresponding to the dissipation of k, and Y_ω is the dissipation of ω,

D_ω is the blending function to blend these two equation models. The closure constants are:

$$a_1 = 0.31, \alpha_0^* = 0.024, R_k = 6, \alpha_\infty^* = 1,\ R_\omega = 2.95, \beta_{i,1} = 0.075, \beta_{i,2} = 0.0828,$$

$$\beta_\infty^* = 0.\,09, R_\beta = 8, \sigma_{k,1} = 1.176\,, \sigma_{k,2} = 1.0, \sigma_{\omega,1} = 2.0\,, \sigma_{\omega,2} = 1.168$$

3.2.3 Conservation of Energy

The conservation of energy, neglecting the energy transfer due to pressure work and viscous dissipation, on the framework of VOF can be written for all phase as

$$\frac{\partial}{\partial t}(\rho h) + \nabla \cdot \left(\rho h \vec{U}\right) = \nabla \cdot \left(K^{\text{eff}} \nabla T\right) + \sum_{i=1}^{n} D_{i,j} \vec{\nabla} Y_i \cdot c_{p,i} \nabla T + S_T \tag{3.16}$$

where T is the temperature field shared by both the liquid and gas phases, and h denotes the mass averaged enthalpy defined as

$$h = \frac{\alpha_l \rho_l h_l + (1-\alpha_l)\rho_g h_g}{\alpha_l \rho_l + (1-\alpha_l)\rho_g} \tag{3.17}$$

The entropy of phase k depends on the temperature, species mass fraction and heat capacity according to

$$h_k = \sum_{i=1}^{n} Y_{i,k} h_{i,k} \tag{3.18}$$

$$h_{i,k} = \int_{T_0}^{T} c_{p,i,k}\, dT \tag{3.19}$$

in which $c_{p,i,k}$ represents the heat capacity of species i in phase k.

The second last term in Equation (3.16) accounts for the energy flux transferred along with the diffusion mass fluxes, which would affect the temperature field when the evaporation rate is large.

The effective thermal conductivity K^{eff} is conductivity determined by the sum of material properties and the turbulent flow conditions, and the calculation equation can be written as

$$K^{\text{eff}} = K_m + K_t \tag{3.20}$$

in which, K_m is the molecular thermal conductivity of the species, which can be calculated based on kinetic theory and is a function of local temperature and species concentration as shown in Section 3.4. While K_t is the turbulent thermal conductivity, which is a property of the turbulent flow. And the turbulent thermal conductivity can be calculated as:

$$K_t = \frac{c_p \mu_t}{Pr_t} \tag{3.21}$$

where Pr_t denotes the turbulent Prandtl number, which is of the order of unity in the literature, ranging from 0.5 to 1.0. A value of $Pr_t = 0.9$ is also used in the present study as recommended [133]. c_p is the heat capacity and μ_t is the turbulent viscosity as defined in Section 3.2.2.

The term S_T represents any energy generation and consumption, which is zero inside the flow for both phases, except on the gas/liquid interface. At the gas/liquid interface, the source term represents the energy transfer between the liquid wall film and gas stream due to the evaporation of liquid wall film, which can be calculated as:

$$S_T = A\dot{m}'' H_{fg}/V \tag{3.22}$$

where A is the effective evaporation area at the gas liquid interface, $\dot{m}''$ is the local evaporation mass flux, which can be evaluated by the mass fraction gradient of the vapor species. H_{fg} is the latent heat of the liquid wall film. V is the volume of local grids in the computational grids.

3.2.4 Conservation of Species

A phase-averaged form of the species conservation equations is used in this study, and the species transport equation is solved for each phase separately. A general form of the conservation of species can be written as:

$$\frac{\partial}{\partial t}(\rho Y_i) + \nabla \cdot \left(\rho Y_i \vec{U} + \vec{N}_i\right) = S_i \tag{3.23}$$

where the index i refers to different species either in the gas phase. Y_i is the mass fraction of species i in the gaseous phase and N_i is the diffusion mass flux of species i.

The diffusion mass flux of species i consists, ordinary (concentration) diffusion, pressure diffusion, body force diffusion and thermal diffusion. For this study, pressure diffusion, body force diffusion and thermal diffusion are negligible compared to ordinary diffusion, hence, the diffusion mass flux formulation can be calculated by the Fick's law as:

$$N_i = -\nabla \cdot \left(\rho D_{i,j}^{eff} \vec{\nabla} Y_i\right) \tag{3.24}$$

where $D_{i,j}^{eff}$ is the effective diffusion coefficient, which can be evaluated by the sum of molecular diffusivity , $D_{i,j,m,}$ and the turbulent diffusivity $D_{i,j,t}$.

$$D_{i,j}^{eff} = D_{i,j,m} + D_{i,j,t} \tag{3.25}$$

In the present study, only the main component in the liquid wall film is considered and the liquid wall film is considered to be single component. Thus, only the gaseous binary diffusion coefficient are considered, and the Fuller's method is adopted for the estimation of the molecular diffusion coefficient $D_{i,j,m,}$ written as

$$D_{i,j,m} = \frac{0.0143T^{1.75}}{PM_{ij}^{1/2}[(\sum V)_i^{1/3} + (\sum V)_j^{1/3}]} \tag{3.26}$$

where P and $T$are pressure and temperature, respectively, and $\sum V$ is sum of the atom volumes for each component by summing atomic diffusion volumes. The average molecular weight of species i and j, M_{ij}, is calculated using the value of molecular weight of species i and j as

$$\frac{2}{M_{ij}} = \frac{1}{M_i} + \frac{1}{M_j} \tag{3.27}$$

The turbulent diffusion coefficient, $D_{i,j,t}$, which can be determined by the turbulent viscosity and turbulent Schmidt number, can be written as

$$D_{i,j,t} = \frac{\mu_t}{\rho Sc_t} \tag{3.28}$$

where Sc_t is the turbulent Schmidt number. The value of turbulent Schmidt number is chosen to be the same as turbulent Prandtl number, due to the similarity of mechanism of turbulent heat and mass mixing.

3.2.5 Volume of Fluid

The gas/liquid interface is crucial for the implementation of evaporation model due to the strong coupling between interfacial momentum, heat and mass exchange for the evaporating wall film all occurs at the gas/liquid interface. The VOF model is employed in the present study for the simulation of the two phase problem with large density difference. The volume fraction conservation equation of liquid phase solved in the VOF model can be written as

$$\frac{\partial}{\partial t}(\rho_l \alpha_l) + \nabla \cdot \left(\rho_l \alpha_l \vec{U}\right) = S_\alpha \tag{3.29}$$

where α_l is the volume fraction of the liquid phase; and $S\alpha$ represents mass source exchange between the liquid wall film and gas stream, which can be written as

$$S_\alpha = A\dot{m}''/\rho_l \tag{3.30}$$

in which, A represents the effective evaporation area, and $\dot{m}''$is the evaporation mass flux. Based on the assumption that the gas mixture is insoluble in the liquid phase and the mass transfer is only in one direction, the mass flux at the gas/liquid interface can be calculated as

$$\dot{m}'' = \frac{1}{1-Y_{i,g,s}} \rho_g D_{i,j} \frac{\partial Y_i}{\partial y} \tag{3.31}$$

where $Y_{i,g,s}$ is the interfacial mass fraction of the i^{th} species in the gas phase. Since the interface is assumed to be at thermodynamic equilibrium state and the air-fuel vapor forms an ideal gas mixture, the mass fraction of the i^{th} species at the gas/liquid interface, $Y_{i,g,s}$, can be calculated by Dalton's law of partial pressures as

$$Y_{i,g,s} = \frac{X_{i,g,s} * M_i}{(1-X_{i,g,s}) * M_{air} + X_{i,g,s} * M_i} \tag{3.32}$$

where $X_{i,g,s}$ is the molar concentration of species i, which is determined by the vapor partial pressure on the gas/liquid interface and reference pressure as:

$$X_{i,,g,s} = \frac{P_{vap,i}(T_s)}{P_\infty} \tag{3.33}$$

where $P_{vap,i}(T_s)$ refers to the partial pressure of species i at interfacial temperature (T_s), which can be calculated by the Clausius-Clapeyron equation.

Clausius-Clapeyron equation

By the assumption that a liquid-vapor equilibrium is achieved at the gas/liquid interface of the evaporating liquid wall film, the pressure and temperature of the two phases are equal, and the Gibbs free energy is equal in both side of the phase. Therefore, the Gibbs free energy of vapor will change by the same amount as that of liquid, when the liquid wall film is evaporating, which gives

$$dG_v = dG_l \tag{3.34}$$

After applying the fundamental relations, $dG = Vdp - SdT,$ Equation (3.34) yields

$$-(S_l - S_v)dT + (V_l - V_v)dp = 0 \tag{3.35}$$

After rearranging, Equation (3.35) becomes,

$$dp/dT = (S_l - S_v)/(V_l - V_v) = \Delta S/\Delta V \tag{3.36}$$

Since the change in entropy, ΔS, for the phase change is just mH_{fg}/T,

$$dp/dT = m\,H_{\mathrm{fg}}/(T\Delta V) \tag{3.37}$$

where, H_{fg} is the latent heat of the liquid film, with unit of kJ/kg. Since the change of volume is approximate to that of the vapor produced, and the vapor mixture in the gas phase is assumed to be ideal gas, the expression of vapor pressure in terms of temperature can be written as:

$$dp/dT = H_{\mathrm{fg}}p/\left(T^2\,R/M_{F.g}\right) \tag{3.38}$$

where R is the universal constant $\left(8.314\ \mathrm{j/(mol\cdot K)}\right)$. After the rearrangement of Equation (3.38), the integral of it gives

$$p_{\mathrm{vap,i}}(T_s) = p_0 * \exp\left[-\frac{H_{\mathrm{fg}}}{R/M_{F.g}}\left(\frac{1}{T_s} - \frac{1}{T_0}\right)\right] \tag{3.39}$$

in which p_0 refers to the reference pressure at the reference temperature T_0.

3.3 Boundary and Initial Conditions

The governing equations described in the previous section required boundary conditions to complete the evaporation model formulation. These boundary conditions represent the typical evaporation conditions in DISI engines and varies based on the conditions of gaseous velocity magnitude and temperature, turbulence intensity of the inlet gas flow and wall temperature.

At the inlet of the computation domain, a uniform velocity profile is specified, and the velocity gradient is set to be zero at the outlet. Turbulence boundary conditions are specified as the turbulence intensity and specify turbulence viscosity ratio (typically using 5) at the inlet and the outlet. Non-slip boundary conditions are imposed on the velocity component at the walls and a constant value of gauge pressure is identified at the outlet. A uniformed temperature and mass fraction profiles are also implied at the inlet; and the temperature and mass fraction gradient are set to vanish at the exit of the domain as

$$\frac{\partial \phi}{\partial y} = 0;\ \phi = T \text{ and } Y_i \tag{3.40}$$

As thermodynamic equilibrium is attained at the gas/liquid interface, and the air/vapor mixture is an ideal gas mixture, the interfacial mass fraction of the i^{th} species $Y_{i,g,s}$ can be calculated by Dalton's law of partial pressures as described Equation (3.32).

After applying conservation of species i on the gas/liquid interface, the species conservation equation gives

$$\dot{m}_i'' Y_{i,g,s} - \rho D_i \frac{\partial Y_i}{\partial y} |_{g,s} = \dot{m}_i'' Y_{i,l,s} - \rho D_i \frac{\partial Y_i}{\partial y} |_{l,s} \tag{3.41}$$

On the gas/liquid interface, due to the continuous of velocity, the x – direction velocity of the gas phase is equal to the liquid phase velocity at the gas/liquid interface. The transverse velocity component of the air-vapor mixture at the gas/liquid interface is deduced by the blowing effect of the evaporation mass flux, which is considered in the model through including source terms in the transport of liquid volume fraction equation, Equation (3.29).

Since the temperature is single-valued in both phases and the energy is conserved on the gas/liquid interface, the boundary conditions on the for the temperature equation at the interface are

$$T_{l,s} = T_{g,s} \tag{3.42}$$

$$-k_l \frac{\partial T}{\partial y}|_{l,s} = -k_g \frac{\partial T}{\partial y}|_{g,s} + \dot{m}'' H_{\text{fg}} \tag{3.43}$$

Initially, the velocity and gauge pressure in the computational domain are set to zero and the liquid wall film is introduced in the domain. Uniform velocity, temperature and species equal to that at the inlet of the computational domain are initialed before the calculation according to different flow conditions in DISI engines.

3.4 Material Properties

Table 3.5: Mixing Law of the Thermo-physical Properties of the Gas Mixture

Properties	Gaseous mixture
Density/ ρ	$\rho_{g,m} = \sum_{i=1}^{n} \rho_i$
Viscosity/μ	$\mu_{g,m} = \sum_{i=1}^{n} \frac{X_i \mu_i}{\sum_{j=1}^{n} X_j \varphi_{ij}}$
Thermal conductivity/k	$k_{g,m} = \sum_{i=1}^{n} \frac{X_i k_i}{\sum_{j=1}^{n} X_j A_{ij}}$
Diffusion coefficient/ $D_{i,j}$	$D_{g,i,m} = \frac{1 - X_i}{\sum_{i,j \neq i} X_j / D_{ij}}$
Interfacial mass fraction/ $Y_{\text{i,g,s}}$	$Y_{i,g,s} = \frac{X_{i,g,s} * M_i}{(1 - X_{i,g,s}) * M_{air} + X_{i,g,s} * M_i}$
Interfacial vapor pressure/ $p_{\text{vap,i}}$	$p_{\text{vap,i}}(T_s) = p_0 * \exp\left[-\frac{H_{\text{fg}}}{R/M_{F.g}} (\frac{1}{T_s} - \frac{1}{T_0})\right]$

Note: $\rho_i = \frac{X_i P}{R_i T}$, $\varphi_{ij} = \frac{\left[1+\left(\mu_i/\mu_j\right)^{1/2}\left(M_j/M_i\right)^{1/4}\right]^2}{\left[8\left(1+M_j/M_i\right)\right]^{1/2}}$,$A_{ij} = \frac{\gamma\left[1+\left(K_i/K_j\right)^{1/2}\left(M_j/M_i\right)^{1/4}\right]^2}{\left[8\left(1+M_j/M_i\right)\right]^{1/2}}$, $\gamma = 1.065$, $X_{i,,g,s} = \frac{P_{vap,i}(T_s)}{P_\infty}$

Due to the large gradient in temperature and species concentration within the boundary layer, thermo-physical properties vary dramatically within both the liquid and the gas phases. The mix laws for the mixture thermo-physical properties of gas and liquid phase are tabulated in Table 3.5. Correlations for the evaluation of local thermo-physical properties for pure components as functions of local temperature and concentrations in both phases are listed in Appendix A of this thesis.

3.5 Summary

The mathematical model for the evaporation of liquid wall film in the DISI engine-like conditions is developed in this thesis study for the investigation of its transient transport phenomena and evaporation characteristics. The complete set of governing equations in the model consist of conservation of mass, momentum, energy, species, volume fraction of the liquid phase and the turbulence quantities.

$$\frac{\partial}{\partial t}(\rho) + \nabla \cdot \left(\rho \vec{U}\right) = S_m$$

$$\frac{\partial}{\partial t}\left(\rho \vec{U}\right) + \nabla \cdot \left(\rho \vec{U}\vec{U}\right) = -\nabla P + \nabla \cdot (\tau) + S_M$$

$$\frac{\partial}{\partial t}(\rho h) + \nabla \cdot \left(\rho h \vec{U}\right) = \nabla \cdot (k \nabla T) + \sum_{i=1}^{n} D_{i,j,k} \vec{\nabla} Y_{i,k} \cdot c_{p,i} \nabla T_k + S_T$$

$$\frac{\partial}{\partial t}(\rho Y_i) + \nabla \cdot \left(\rho Y_i \vec{U} + \vec{N}_i\right) = S_i$$

$$\frac{\partial}{\partial t}(\rho_l \alpha_l) + \nabla \cdot \left(\rho_l \alpha_l \vec{V}\right) = S_\alpha$$

$$\rho \frac{\partial \kappa}{\partial t} + \rho U_j \frac{\partial \kappa}{\partial x_j} = \frac{\partial}{\partial x_j}\left[(\mu + \frac{\mu_t}{\sigma_k})\frac{\partial \kappa}{\partial x_j}\right] + G$$

$$\rho \frac{\partial \varepsilon}{\partial t} + \rho U_j \frac{\partial \varepsilon}{\partial x_j} = \frac{\partial}{\partial x_j}\left[(\mu + \frac{\mu_t}{\sigma_\varepsilon})\frac{\partial \varepsilon}{\partial x_j}\right] + C_1 f_1 \left(\frac{\varepsilon}{k}\right) G - C_2 f_2 \rho \left(\frac{\varepsilon^2}{k}\right)$$

In total, 8 variables need to be determined in order to study the evaporation process of liquid wall film in engine-like conditions through numerical simulation. These equations are strongly coupled through intensive interphase mass, energy and momentum transfer.

The transient motion and heating of the liquid phase, the blowing effects caused by evaporation, and the variation of thermo-physical properties are all included in the numerical evaporation model as displayed in this chapter. In addition, boundary and initial conditions with the correlations of the thermo-physical properties are also presented in this chapter.

Chapter 4
Numerical Implementation

4.1 Numerical Methodology

As elucidated in Chapter 3, the evaporation of liquid wall film in DISI engine-like flow conditions are governed by a set of non-linear partial differential equations with their pertinent source terms originated from the phase changes and gas/liquid interactions at the gas/liquid interface. Furthermore, the thermo-physical properties in these governing equations are functions of the unknown variables which need to be solved in these equations. Consequently, the model of evaporating liquid wall film in DISI engine-like flow conditions is highly nonlinear and difficult to be implemented and solved in the numerical simulation platform. In this chapter, the implementation of the evaporation model and some techniques for the stability of the numerical model will be presented.

4.1.1 Numerical Procedure

The computational domain of this study, as displayed in Figure 5.8 in Chapter 5, is divided in to a set of structured non-uniform grids in this study, and a pre-processing software, ICEM 15.0, is employed in this study for the generating of computational grids. The governing equations of the evaporating liquid wall film model are discretized and solved in the Computational Fluid Dynamics (CFD) software, FLUENT 15.0, based on the Finite Volume Method (FVM). The platform of FLUENT has provided the framework of solving the energy and species transport equation together with the continuity and momentum equations, and a VOF model with Piecewise Linear Interface Construction (PLIC) algorithm is also included [44, 45]. However, due to the limitation of the software, the PLIC variables in it cannot be accessed directly by users.

Furthermore, the VOF model in the FLUENT platform is not capable to simulate the phase change and to reconstruct the sharp gas/liquid interface simultaneously. Therefore, some User Defined Functions (UDFs) programs are developed for the implementation of the phase change process on the sharp gas/liquid interface using the programming language C, and the flow chart of the UDF for the numerical model implementation is displayed in Figure 4.1. Moreover, the temperature and composition dependent physical properties in the governing equations of the evaporation models are also incorporated and updated in the numerical model using the UDF programs.

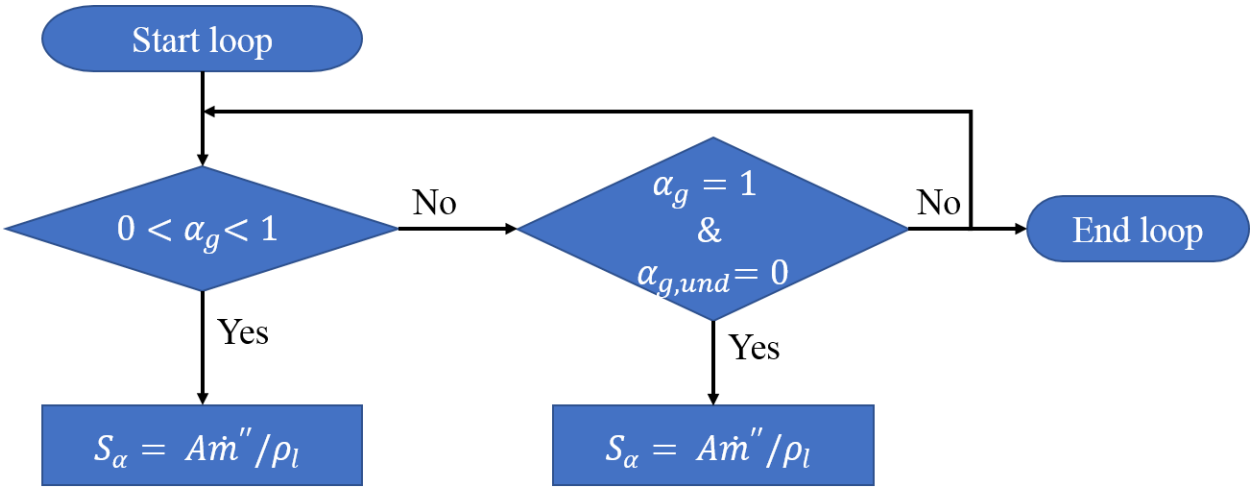

Figure 4.1: Illustration of the numerical implementation of the evaporation model

The discretized governing equations are solved in a pressure-based segregated solver in the numerical simulation platform in this study. The coupled momentum, energy and mass transfer processes are decoupled in the segregated solver, and the governing equations are solved one by one for the unknown variables (such as velocity, temperature and species mass concentrations) involved in the evaporation models representing the transport of momentum, energy and species. Furthermore, the PISO algorithm is employed for the velocity and pressure coupling in this thesis study, in which the velocity field is verified and corrected by the pressure values to make sure that the numerical results can meet the constraint of the conservation of mass.

Since much smaller number of iterations is needed in the PISO algorithm for a transient simulation problem, this method is considered to be more efficient than the SIMPLE family algorithm.

Outer loop

During the numerical solving process, two different loops (outer loop and inner loop) are involved due to the complexity of the governing equations. In the outer loop, the decoupled partial differential equations are solved consequently and interactively until the numerical residual error meet the converge criteria, while in the inner loop, the individual governing equations are also solved iteratively. The details of the outer and inner loops during the numerical solving procedure are given in the following sections.

The numerical solution procedure in the outer loop of the segregated loop is illustrated in Figure 4.1; and the major steps of the solution procedure are outlined as follows:

1. Initialize the computational domain with the initial conditions.
2. Update the thermos-physical properties of the materials (liquid or gas mixtures) using the solutions from the most current iteration.
3. Solve the momentum equations at different directions sequentially based on the newest value of pressure and mass fluxes.
4. Solve the continuity equation (pressure correction) with the velocity and pressure coupling algorithm using the most updated values of velocities.
5. Update the values of mass fluxes, pressure, and velocities.
6. Solve other related transport equations, (i.e. energy, species concentration, turbulence kinetic energy and turbulence kinetic energy dissipation rate) based on the new value of velocities and pressures.

7. Calculate the source terms originating from the phase change occurring on the gas/liquid interface and interaction between two phases.
8. Check for the convergence of all the calculated equations using the convergence criteria.

The outer loop of the numerical solution procedure continues until the correction error of each equation meets (lower than) the convergence criteria.

Inner loop

In the inner loop of the numerical procedure, the governing equations are solved separately one after another. The FVM is employed in this study for the discretization of each governing equations; and the discretization procedure can be illustrated using the transport equation of a general variable Θ. The integral form of the transport equation in a control volume, V, can be written as:

$$\int_V \frac{\partial \rho \Theta}{\partial t} dV + \oint \rho \Theta \vec{U} \cdot d\vec{A} = \oint \Gamma_\Theta \nabla \Theta \cdot d\vec{A} + \int_V S_\Theta \, dV \quad (4.1)$$

where ρ represents the density of the fluid, $\vec{U}$ the velocity vector, $\overrightarrow{A}$ the vector of the surface in the control volume, Γ the general form of diffusion coefficient, and S_Θ the source term in each control volume.

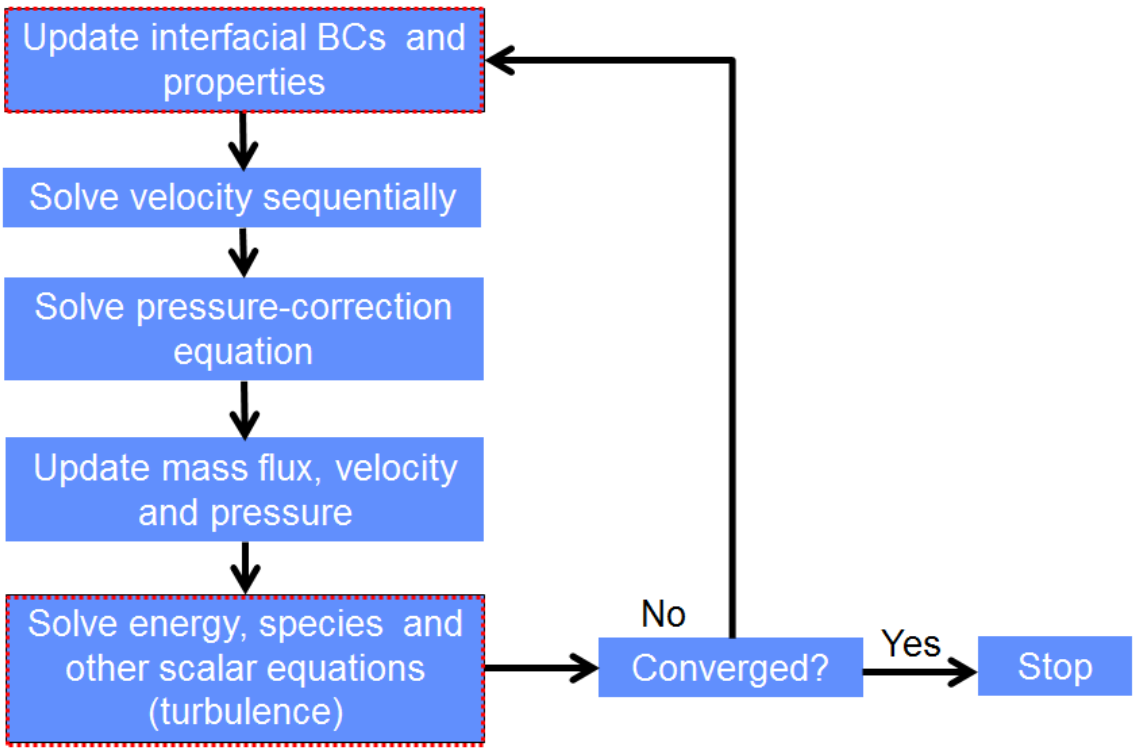

Figure 4.2: Illustration of the consequently solving procedure in a segregated numerical solver.

After performing the integral on Equation (4.1) for a given cell in the computational domain, the transport equation of Θ can be written as:

$$\frac{\partial \rho \Theta}{\partial t} V + \sum_{f}^{N_{faces}} \rho_f \vec{U}_f \cdot \vec{A}_f = \sum_{f}^{N_{faces}} \Gamma_\Theta \nabla \Theta_f \cdot \vec{A}_f + S_\Theta V \tag{4.2}$$

In this discretized equation, the values of variable,Θ, are unknown both at the cell center and on the surrounding faces in each computational cell; and the equation is usually non-linear with these unknown variables. Therefore, proper discretization schemes are required for the linearization of the discretized equation.

Equation (4.3) shows the linearized discretized equation after perform linearization using suitable discretization schemes.

$$a_P \Theta = \sum_{nb} a_{nb} \Theta_{nb} + b \tag{4.3}$$

where nb represents the nodes around the central nodes, P is the central nodes for the current calculation, a denotes the linearized coefficient for each cell involved in the discretization, and b represents a source term in each cell.

In the discretized continuity equation, the density at each cell in the computational domain is discretized using the second order upwind scheme; whereas the pressure value in the center of each cell is estimated based on the pressure values of its surrounding cells using a standard linearization method. For other transport equations, such as energy, species and turbulent kinetic energy, which are typically in the convention-diffusion form. The convection terms in these equations are discretized using the second order upwind scheme, which has high stability performance and low numerical errors; while the diffusion terms are discretized using the central difference method, which also has the second order accuracy in terms of the numerical errors. For the unsteady term in the governing equation, a backward difference scheme is used for the discretization of time derivative, which has the first order accuracy. Furthermore, the whole equations are calculated in an explicit manner at each iteration of time step, due to the requirement of the VOF model with PLIC interface construction algorithm. Hence, the time steps are adjusted to maintain a Courant–Friedrichs–Levy (CFL) number less than one to ensure the stability of the numerical simulation.

After performing the discretization of all the computational cells in the computational domain, a matrix of linearized coefficients from each cell in the domain is formed, which can be solved afterwards. In this thesis study, an implicit Gauss-Seidel linear equation solver is used for the solving of the coefficients matrix; and the details of this method can be also find at the theory of solver in the manual of the CFD software [114].

4.1.2 Under-relaxation Schemes

The evaporation model of liquid wall film in DISI engine like conditions are hard to implement on the numerical platform due to the strict requirement of simulating the sharp gas/liquid interface and phase changes between two different phases at the same time. Furthermore, the source terms originating from the intensive interaction between two phases reduce stability of the numerical models. Thus, two different under relation schemes are adopted in the present study to increase the stability and robustness of the evaporation model.

In order to mitigated the effects of the source term at the gas/liquid interface and the highly non-linear variables in the governing equations, the classical Gauss-Seidel successive Under-Relaxation (SUR) scheme is used in this thesis study; and this under relaxation scheme can be written as:

$$S_{\Theta}^{n} = S_{\Theta}^{n} + \alpha(S_{\Theta}^{new} - S_{\Theta}^{n-1}) \tag{4.4}$$

$$\Psi^{n} = \Psi^{n-1} + \alpha(\Psi^{new} - \Psi^{n-1}) \tag{4.5}$$

In which, α denotes the under-relaxation factor ranging from 0 to 1, $()^{n-1}$ represents previous iteration results, and $()^{new}$ denotes the current iteration values. This kind of under-relaxation technique is considered to be the first kind of under relaxation scheme, which is mainly for the solving process of each equations in the inner loop.

Also, the second type of under-relaxation scheme used for the limitation of variable changes between two close iterations in the outer loop is also included in the present study to avoid the divergence caused by the large changes between two close iterations. An implicit under-relaxation scheme proposed by Patankar [132] is adopted as the second under relaxation scheme, and this scheme can be written as:

$$\frac{a_P\Theta}{\alpha} = \sum_{nb} a_{nb}\Theta_{nb} + b + \frac{1-\alpha}{\alpha} a_P\Theta^{n-1} \quad (4.6)$$

The evaporation model is very sensitive to the under-relaxation factors, especially for the second under-relaxation schemes. Typically, a very small under-relaxation factor is used at the beginning stage of the transient numerical simulation, and a more aggressive value can be chosen after certain amount of iterations. Also, increase the under-relaxation values can cause the increase of residual of the numerical results, but these residuals can gradually disappear as numerical calculation proceed.

4.1.3 Convergence Criteria

The residuals of each variables are calculated at the end of each outer-loop iteration, and the numerical solving process stops when the residuals of all the equations meet the convergence criteria. A non-dimensioned residual is used in this study due to the small values of species concentration, and the definition of the residuals can be written as:

$$R^{\Psi} = \frac{\sum_{cells}|\sum_{nb} a_{nb}\Psi_{nb} + b - a_P\Psi_P|}{\sum_{cells}|a_P\Psi_P|} \quad (4.7)$$

It indicates that the residuals of the variables are calculated by the ratio between the summations of imbalance in the linearized equation normalized by the representative values at the central of the computational grids in the whole domain. An extremely small residual value, 1×10^{-6}, has been chosen as the convergence criteria in the present study, which is considered to be accurate enough.

4.2 Multi-phase Flow Problem

For the implementation of multi-phase flow problems in the numerical platform, special requirement on the data types are needed in order to account for the flow in each phase and the interphase interactions. In the platform of FLUENT, three are three different types of domain that

are used for the simulation of multi-phase flow problems. The first type of domain is referred as ‘super domain’, which represents the sum of all the phases. In the super domain, the properties and variables of the mixture are stored and solved. Specifically, the momentum and energy conservation equation are solved in the super domain in the present study. The second type of domain in the multiphase problem is the ‘sub domain’, which is used to account for the simulation of each phase. In the third type of domain, the interaction between different phases are considered, which is used for momentum, energy and mass transfer between different phases.

The solver information stored in the Thread, which is a type of data structures in FLUENT, and the threads of the super domain are associated with the sub-domains. Some of the information stored in the super-domain are also shared with the sub-domains. The domain and thread hierarchy are demonstrated in Figure 4.2, in which the concept of the domain id and phase domain index are displayed. The domain id is used to distinguish the super domain from the sub-phase domains and the interaction domains.

The data structures of a multiphase problem depend on the type of different multiphase model, the property or term that need to calculated, the implementation methodology of the source terms, and the phase domain that is affected. In the present study, the VOF multiphase model is used, and a single set of momentum and energy conservation equations are solved for a mixture in the super-phase domain. The interphase interaction is implemented in the numerical simulation model through including a source term in the secondary phase, the evaporating liquid wall film, in the transport of volume fraction of the liquid phase.

The boundary conditions of momentum and energy conservation equations are implied in the thread of super domain, and the stored information are shared with the threads in the sub domains.

Since the species transport only occurs in the gaseous phase, the boundary conditions for the species transport only implied in the gaseous phase using the UDF programs.

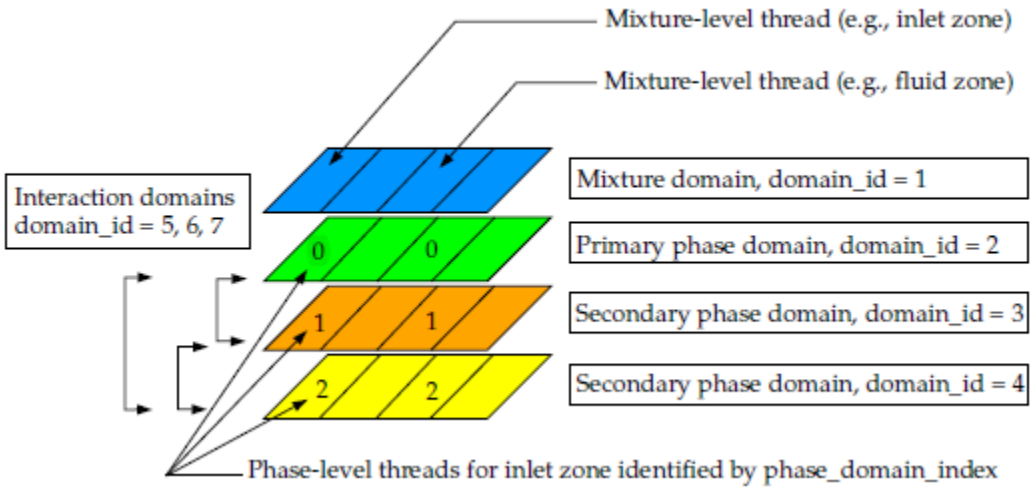

Figure 4.3 Domain and thread structure hierarchy [114].

4.3 Grid Independency

The proper number of grids in the computational domain is crucial for the numerical study, and a grids independent test has been performed in the present study to identify the suitable grids numbers. Since a two-dimensional numerical model is established in this study, so the grids independent test is divided into two steps for two different flow directions. In each test step, the girds number only changes in one direction, while grids number on the other geometry direction is unchanged. Also, the thickness of first layer grids in both of the liquid and gas phases is the same besides the gas/liquid interface. In the first step of the grids test, the grids number in the x directions keeps as a constant, while a series numbers of grids in the other direction is generated.

Due to the intensive gas/liquid interaction within the boundary layers both in the liquid and gas phase and phase change process occurring on the interface, a non-uniform grid scheme is used for

the consideration of computational cost and efficiency. The grids adjacent to the gas/liquid interface are refined and an increasing factor is adopted for the grid generation in the y direction. The test results, as displayed in Figure 4.3, demonstrate that increasing the grids numbers within the boundary layer in the y direction can enhance the accuracy of the numerical results, while when the grids are too coarse, the discretization error becomes very large and the solution is very likely to be diverging. However, adding too many grids in one-direction may also leads to instable numerical results because of the large aspect ratio.

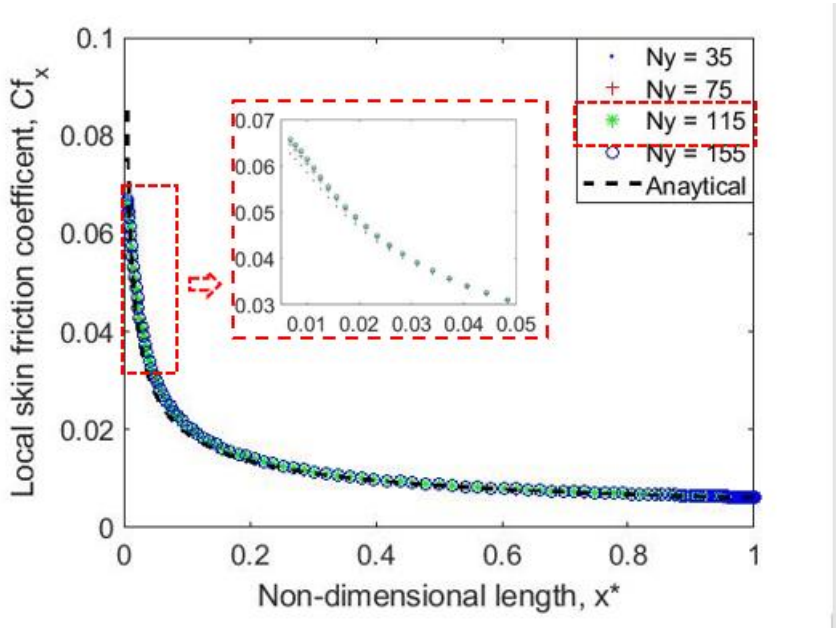

Figure 4.4 Grid sensitivity test results of different grids number in y-direction of the gas phase

In the second step, the number of grids in the x-direction (N_x) is determined similar to the test procedure in the first step. A suitable number of grids in the x direction are also very important for the successfully capture of the bubble developed in the small steps at the beginning and ends of the liquid wall film. Finally the grids of $131 \times 26\ (x \times y)$ in the liquid phase and $131 \times 115\ (x \times y)$ in the gas phase with increase factor of 1.05 staring from the gas/liquid interface can provide accurate numerical results, which is also employed in this thesis study.

4.4 Time Step Independency

The proper time steps are also important for the unsteady numerical study. In theory, using an extremely small time step is always safe to obtain accurate numerical results for a transient simulation, however, the small time step will also cause the tremendously increase of computational cost and time spending. On the other side, using a larger time step can save some computing time but can also obviously reduce the accuracy. In the present study, multiple time step algorithm is used to ensure the accuracy of the numerical results with the optimum computational cost. In the early stage of the transient simulation, a smaller time step is used and a relative larger time step is used after the numerical calculation becomes more stable.

After the time step sensitive test, a minimum time step of 10^{-7}s is able to generate accurate and stable numerical results at the beginning of all the numerical calculation process. Thus, 10^{-7} s has been chosen as the lower limit of the time step range. In addition, the maximum time step size, 10^{-5} s, is defined as the upper limit.

4.5 Summary

In this chapter, the numerical implementation of the evaporation mode and some numerical techniques developed during the implementation process are explained. Also, girds independent and time step independent test are performed for the identification of the proper grid numbers of different geometry directions and suitable time steps for the transient simulation of the evaporation process. The numerical results show that the numerical techniques developed in this study can handle the stiffness of the evaporation model properly, and accurate numerical results can be obtained in the numerical study. Furthermore, the non-uniform grids both in all the geometry

directions are effective on the saving of computational resources, and an adaptive time step algorithm can save the computational cost as well.

Chapter 5
Mass Transfer Correlations of Evaporating Liquid Wall Film

With the evaporation model and numerical implementation techniques have been presented in the previous chapters, the transient evaporation characteristics of the liquid wall film in DISI engine-like conditions are investigated; and the mass transfer correlations of the wall film are determined. The evaporation of liquid wall film is quite complex considering the strong coupling among the transport of momentum, energy and species along with the complex gas flow conditions in engines. Hence, the evaporation characteristics of evaporating liquid wall film in three different evaporation conditions, 1) in a stagnant gas medium, 2) in laminar flow conditions and 3) in turbulent flow conditions are investigated; and the results of the transient evaporation characteristics and mass transfer correlations of evaporating liquid wall film in DISI engine-like conditions are presented in this Chapter.

5.1 Evaporation in a Stagnant Gas Medium

The evaporation of liquid wall film in a stationary gas medium is studied in this study to provide some benchmark data for the verification of the numerical implementation due to the sparseness of the experimental data. An analytical model for the evaporating liquid wall film in a stagnant gas medium is developed and solved; and the results are displayed in this section.

5.1.1 Analytical Model

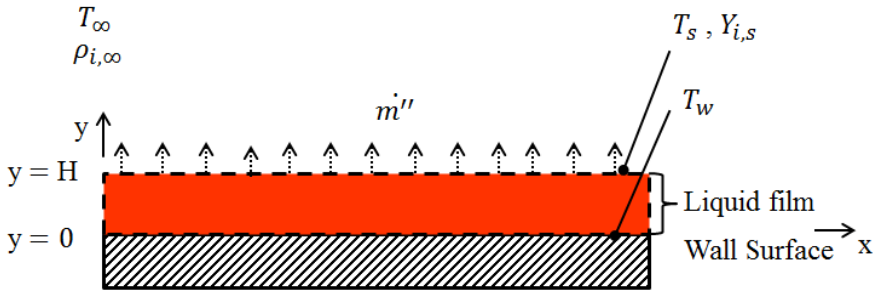

Figure 5.1: Schematic of evaporating liquid wall film on the wall surface in a stationary gas medium.

Figure 5.1 displays the schematic figure of the evaporating wall film on the surface of cylinder wall in a stationary gas medium along with the coordinates. Here, the gas/liquid interface is assumed to be perfectly flat and the initial thickness of the liquid film is set to be a constant H at different locations on the wall surface. Since only the transport of species in the gas phase is considered, and the evaporation process is assumed to be isothermal; the general governing equations developed in Chapter 3 can be simplified to a species transport equation on the gas phase as written in Equation (5.1).

$$\frac{\partial Y_i}{\partial t} = D \frac{\partial^2 Y_i}{\partial y^2} \tag{5.1}$$

where Y_i mass fraction of species i, t is time, D is the binary diffusion coefficient of the wall film vapor in the air, and y is the space dimension as shown in Figure 5.1.

As stated in Chapter 3, the interfacial mass fraction of species i $Y_{i,s}$ can be determined using the Dalton's law of partial pressure as:

$$Y_{i,s} = \frac{M_v X_i}{(1 - X_i) M_a + M_v X_i} \tag{5.2}$$

Where M_v and M_a are the molecular weight of the fuel vapor and air respectively. X_i is the molar concentration of species i, in which the interfacial partial pressure for species i is estimated by the Clausius-Clapeyron equation, as shown in Section 3.2.5.

In the present study, three different boundary conditions representing three typical evaporation conditions are considered, which are evaporation in an infinite space denoted as case-I, evaporation in a finite space denoted as case-II and evaporation with oscillation boundary conditions denoted as case-III. Pertinent initial and boundary conditions for these conditions are tabulated in Table 5.1.

Table 5.1: Initial and boundary conditions for evaporating liquid film in a stationary gas medium

Cases	Initial and boundary conditions
Case-I	*I.C:* $at\ t \leq 0, \quad Y_i(y,0) = 0$
	B.C.1: $at\ y = H,\ Y_i = Y_{i,s}$
	B.C.2: $at\ y \to \infty,\ Y_i = 0$
Case-II	*I.C:* $at\ t \leq 0,\ Y_i(y,0) = 0$
	B.C.1: $at\ y = H,\ Y_i = Y_{i,s}$
	B.C.2: $at\ y = y_b,\ \frac{\partial Y_i}{\partial y} = 0$
Case-III	*I.C:* $at\ t \leq 0,\ Y_i(y,0) = 0$
	B.C.1: $at\ y = H,\ Y_i = Y_{i,m} + Y_{i0}\mathcal{R}(e^{i\omega t})$
	B.C.2: $at\ y \to \infty,\ Y_i = 0$

The evaporating process of wall film can be characterized by evaporation mass flux on the gas/liquid interface. Analytical results for these different boundary conditions presented in the

following section show a considerable insight on how the wall film species concentration distribution profile, evaporation rate, mass transfer correlations and film thickness changes with different boundary conditions as time increases. The n-octane (C_8H_{18}) is used as the surrogate for the study of evaporation of liquid wall film in stationary gas medium, and parameters used in the analytical study are tabulated in Table 5.2.

Table 5.2: Parameters used in the analytical solutions of evaporating liquid wall film in a stationary medium

Parameters	Values
Ambient gas temperature, $T_\infty\ (K)$	550 - 630
Density of the liquid, $\rho_l\ (kg/m^3)$	889
Viscosity of vapor, $v_{vap}\ (kg/(m \cdot s))$	6.75e-6
Thermal conductivity of vapor, $K_{vap}\ (W/(m \cdot K))$	1.78e-2
Heat capacity of vapor, $C_{p_{vap}}\ (j/(kg \cdot k))$	2467
Viscosity of liquid, $v_{liq}\ (kg/(m \cdot s))$	5.4e-4
Thermal conductivity of liquid, $K_{liq}\ (W/(m \cdot K))$	0.147
Heat capacity of liquid, $C_{p_{liq}}\ (j/(kg \cdot k))$	2420
Molar weigh of air, $M_a\ (kg/kmol)$	29
Diffusivity coefficient of fuel vapor, $D\ (m^2/s)$	1e-8
Boiling temperature of the liquid film, $T_{boil}\ (K)$	633
Saturated pressure of the vapor, $P_{sat}\ (Pa)$	2.67e-4

The governing equation and pertinent boundary conditions for the evaporation of wall film in a stationary gas medium are solved analytically, and results are presented in this section. For all of these three cases, species is considered transporting in y- direction in the gas medium as shown in Figure 5.1.

5.1.2 Evaporation Characteristics in the Stationary Gas Medium

Case-I (evaporation in the infinite space)

For the liquid wall film evaporating in the infinite space, a dimensionless vapor mass fraction $\varphi = \frac{Y_i}{Y_{i,s}}$ and similarity variable $\eta = y/\sqrt{4Dt}$ are introduced for the convenience of solving the governing equation analytically. The mathematical expression of the final analytical solution is presented as Equation (5.3), and the detailed solving process is attached as Appendix B in the proposal. The non-dimensional vapor concentration distribution profiles are displayed in Figure 5.2.

$$Y_i = Y_{i,s}\left(1 - erf\left(y/\sqrt{4Dt}\right)\right) \tag{5.3}$$

Since the only species crossing the liquid wall film surface is the vapor of the liquid wall film, the mass flux on the gas/liquid interface can be obtained through applying the Fick's law at the gas/liquid interface and being related to the concentration gradient as:

$$\dot{m}'' = -\frac{\rho_g D}{1-Y_{i,s}}\frac{dY_i}{dy}\Big|_{y=y_s} = \frac{\rho_g D Y_{i,s}}{(1-Y_{i,s})\sqrt{\pi Dt}} \tag{5.4}$$

Knowing the evaporation rate of liquid wall film, the variation of film thickness over evaporation time can be determined by applying the overall mass conservation to the whole wall film as

$$\frac{d(\rho_l A h)}{dt} = -\dot{m}'' A \tag{5.5}$$

where A represents the effective evaporation area and h stands for the instantaneous film thickness. For a short time interval Δt, the wall film thickness as a function of evaporation rate and time can be written as

$$h_{new} = h_{old} - \frac{\dot{m}''}{\rho_l}\Delta t \tag{5.6}$$

where h_{new} and h_{old} represents the film thickness at the current time step and previous time step, respectively.

The local mass transfer correlation $h_{m,x}$ and the corresponding Sherwood number Sh_x can also be developed based on local concentration gradient. The conventional definition of local mass transfer correlation and Sherwood number can be written as

$$\left[h_m\left(Y_{i,s} - Y_{i,\infty}\right)\right]_x = \left[-\rho_{g,s} D_s \frac{dY_i}{dy}|_{y=y_s}\right]_x \tag{5.7}$$

$$Sh_x = \frac{h_{m,x}\, x}{\rho_r D_r} \tag{5.8}$$

where the subscript x denotes the local position along the evaporating liquid wall film, h_m represents the mass transfer coefficient. The thermo-physical properties of the gaseous mixture are evaluated at the reference state r, according to:

$$T_r = T_s + r(T_\infty - T_s) \tag{5.9}$$

$$Y_{i,r} = Y_{i,s} + r(Y_{i,\infty} - Y_{i,s}) \tag{5.10}$$

The average mass transfer coefficient and Sherwood number can be obtained as

$$\overline{h}_m = \frac{1}{L}\int_0^L h_m dx \tag{5.11}$$

$$\overline{Sh} = \frac{\overline{h}_m\, L}{\rho_r D_r} \tag{5.12}$$

where L represents the typical length of the wall film and the reference state is chosen as r equals to 0.5.

As shown in Figure 5.2 (a), the vapor of the wall film is penetrating into the stationary gas medium as time increasing for case-I. Each line in Figure 5.2 is plotted along the y-axis through the midpoint of wall film in x-direction, and five different times are considered. The length of vapor diffusing into the gas medium can be with time increasing, vapor species mass fraction, Y_i, in the stagnant air monotonically approaches to the gas/liquid interface mass fraction $Y_{i,s}$. As the magnitude of the interfacial mass fraction gradients decrease over time, the interface mass flux decreases, as displayed and proved by Figure 5.2 (b).

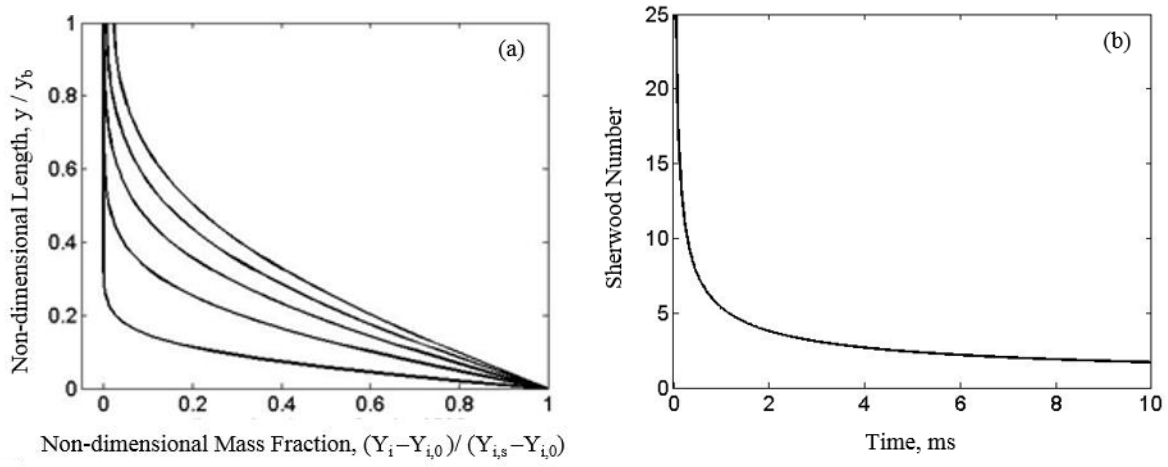

Figure 5.2: Non-dimensional mass fraction profiles and Sherwood number for the evaporation of wall film in a stationary gas medium with an infinite space with y_b the referenced length of the air space above the liquid film at five different non-dimensional time $t^* = Dt/y_b^2 =$ $11.52, 57.60, 115.20, 178.20$ and 230.40

Case-II (Evaporation in a finite space)

For the evaporation of liquid wall film in a finite space, dimensionless variables $\varphi = \frac{Y_i}{Y_{i,s}}$, $\eta = \frac{y}{y_b}$ and $\tau = \frac{Dt}{y_b^2}$ are introduced and the separation variable method are employed to solve the governing equation for the evaporation of liquid wall film in a finite space. The detailed solution process are shown in Appendix B.2, and the finial expression for the non-dimensional mass fraction φ is

$$\varphi = 1 - \sum_{n=1}^{\infty} \frac{4}{(2n-1)\pi} exp\left(-\left(\frac{(2n-1)\pi}{2}\right)^2 \tau\right) sin\left(\frac{(2n-1)\pi\eta}{2}\right), \text{ with } n = 1,2,3 \ldots \quad (5.13)$$

Then, the mass flux at the gas/liquid interface can be then obtained as

$$\dot{m}'' = -\frac{\rho_g D}{1-Y_{i,s}} \frac{dY_i}{dy}\Big|_{y=y_s} = \frac{\rho_g D Y_{i,s}}{1-Y_{i,s}} \sum_{n=1}^{\infty} \frac{2}{y_b} exp\left(-\left(\frac{(2n-1)\pi}{2}\right)^2 \tau\right) \quad (5.14)$$

Through overall mass conservation of the wall film, we can get the thickness of the liquid film using the same method as described for the evaporation of liquid wall film in an infinite stationary gas medium (Case - I).

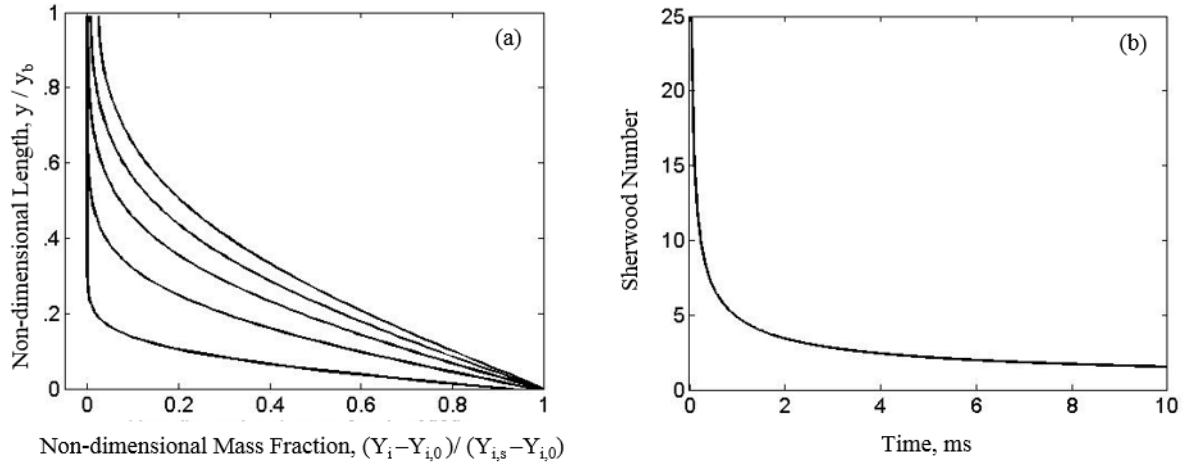

Figure 5.3: Non-dimensional mass fraction profiles and Sherwood number for the evaporation of liquid wall film in a stationary gas medium with a finite space with y_b the air space above the

liquid film at five different non-dimensional time $t^* = Dt/y_b^2 =$

$11.52, 57.60, 115.20, 178.20$ and 230.40

Figure 5.3 (a) shows the non-dimensional vapor mass fraction profile as time increasing for the evaporation of liquid wall film in a finite space, case-II. Each of these lines is plotted along the y-axis through the midpoint of wall film in x-direction and five different times are considered in this case. The general trend of the non-dimensional vapor species mass fraction profile for this evaporation boundary condition is almost the same as case I, in which the vapor species propagate into the stationary gas phase and the mass transfer number decreases as time increases.

Case- III (Evaporation with oscillating boundary conditions)

For the evaporation of wall film under oscillating boundary conditions (interfacial vapor mass fractions), the analytical solution, as shown in Appendix B.3, of the vapor mass fraction profile can be written as a function of oscillating frequency and phase shift as

$$Y_i(y,t) = Y_{i,m} + Y_{is} e^{-\sqrt{\omega/2D}y} cos(\,\omega t - \sqrt{\omega/2D}\,y) \tag{5.15}$$

The exponential term in expression 5.15 describes the attenuation of the oscillatory. In the argument of the cosine, the quantity $-\sqrt{\omega/2D}$, is called the phase shift, which describes how much of the vapor mass fraction oscillations at the distance y from the interface are out-of-step with the oscillating interfacial vapor mass fraction. The mass penetration depth δ_p can be defined as the depth at which significant mass fraction propagate in the stationary gas with penetration depth at the location where$Y_i - Y_{i,s}\,/Y_{i,0} - Y_{i,s} = 0.9$ in the y direction. It is obvious that as time increasing the mass penetration depth for vapor species diffusion in the stationary gas medium is also increase as $t^{1/2}$ as also displayed in Equation (5.3).

The instantaneous mass flux is obtained as

$$\dot{m}'' = -\frac{\rho_g D}{1-Y_{i,s}}\frac{dY_i}{dy}|_{y=y_s} = \frac{\rho_g D Y_{i,s}}{1-Y_{i,s}}\sqrt{\omega/2D}\,[cos(\omega t) - sin(\omega t)] \quad (5.16)$$

Using the same method as described in Case-I, the film thickness and evaporation rate as a function of time for the evaporation of wall film with oscillating boundary conditions can be obtained.

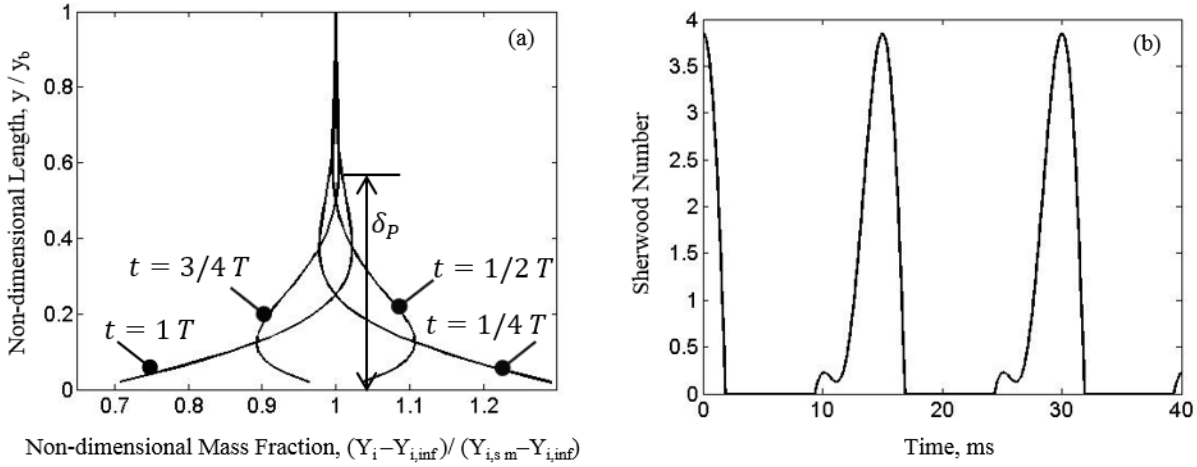

Figure 5.4: Non-dimensional mass fraction profiles and Sherwood number for evaporation of wall film in a stationary gas medium with oscillating boundary conditions with y_b the referenced length of the air space above the liquid film at four different evaporation time t = ¼T, ½T, ¾T and 1T

Figure 5.4 shows the non-dimensional vapor mass fraction profiles as time increasing for case-III, in which wall film is evaporating with oscillating boundary conditions. In this figure, the vapor mass fraction is normalized by the average mass fraction of the vapor on the gas/liquid interface, and each of this line is plotted along the y-axis through the midpoint of wall film in x-direction. In this study, the interfacial mass fractions are oscillating at a period of 20 milliseconds; and it is can be seen form the figure that the vapor mass fraction in the stagnant air medium fluctuates periodically with the same oscillating frequency of the interfacial mass fraction.

At location in the stationary air, the fluctuations have a time lag relative to the interfacial mass fraction and the amplitude of the fluctuations within the stagnant air decays exponentially as shown in Equation (5.15). Consistent with the early definition of the mass penetration depth, the mass penetration depth for case-III can be calculated as a function of diffusion coefficient and oscillating frequency as $\delta_p = 4\sqrt{D/\omega}$.

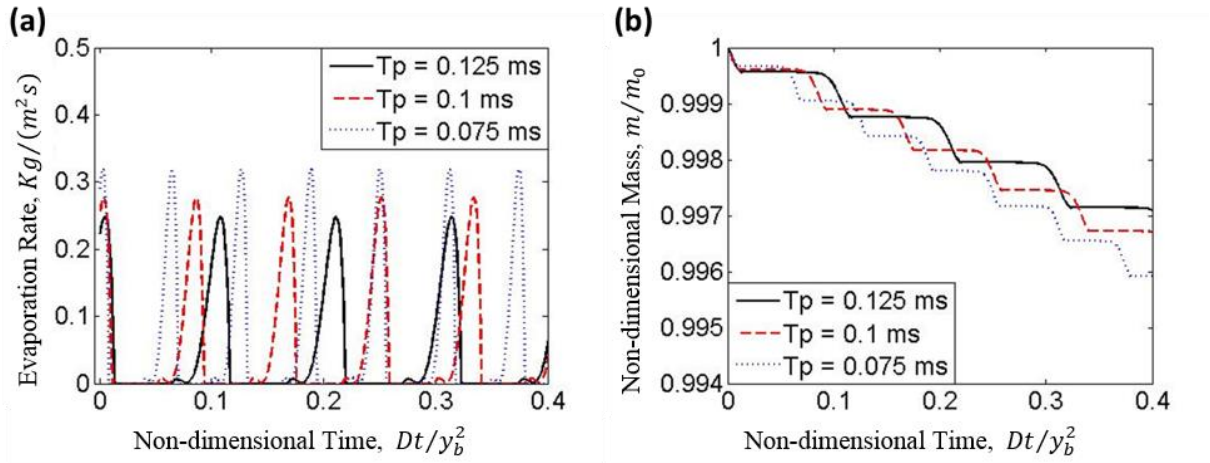

Figure 5.5: Effects of oscillating period on the (a) evaporation rate and (b) non-dimensional evaporation mass rate of evaporating liquid wall film in a stationary gas medium with oscillating interfacial vapor mass fractions. Each line represents different oscillating period as indicated in the legend.

Figure 5.5 illustrates the effects of oscillation period on the evaporation rate and non-dimensional mass of evaporating liquid wall film with oscillating interfacial vapor mass fractions. Three different oscillating periods are considered in this study as indicated in the legend. As oscillating period decreases, the maximum evaporation rate of wall film shows an inverse trend, which can be attributes to the decrease of effective evaporation time in a period of oscillation. In Figure 5.5 (b), the non-dimensional mass of liquid wall film is plotted as non-dimensional time with three

different oscillating periods. It can be observed that decreasing the oscillating period can enhance the evaporation and reduce the evaporation life time of the liquid wall film. With smaller oscillation period, the wall film thickness decreases more quickly. Since the wall film can only evaporate when the interfacial vapor mass fraction gradient is positive, and decreasing the oscillating period can increase the effective time for the evaporation with a certain time interval.

5.1.3 Comparison of Evaporation among Different Boundary Conditions

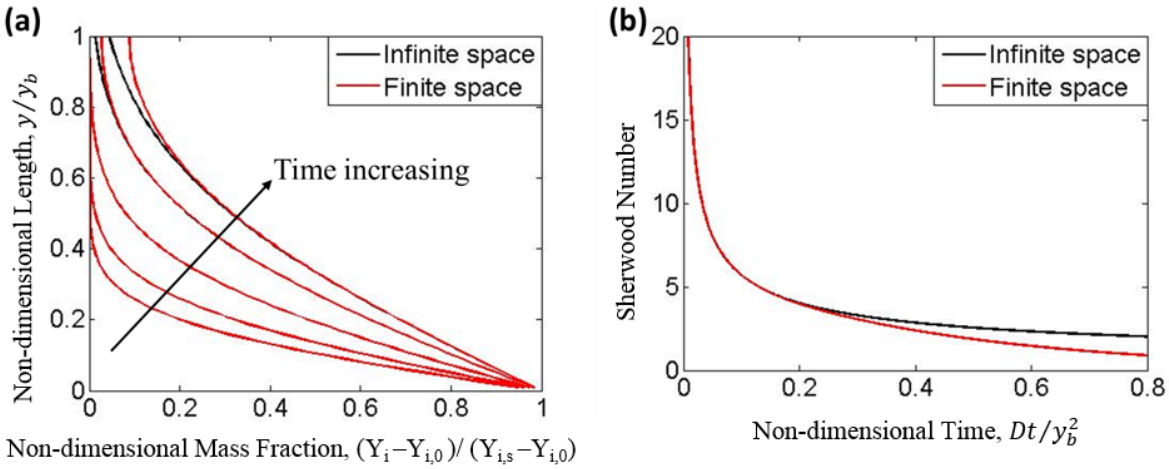

Figure 5.6. Comparison of (a) non-dimensional mass fraction profiles and (b) Sherwood number for evaporation of liquid wall film in an infinite stationary gas medium (case-I) and a finite stationary gas medium (case –II).

Figure 5.6 compares the non-dimensional mass fraction profiles (a) and Sherwood number (b) as time increasing. It can be observed that in the early stage of the transient evaporation process when the non-dimensional evaporating time interval is very small, the vapor species is only diffused into the stationary air in a very short distance close to the gas/liquid interface; thus the vapor cannot feel the presence and limitation of the wall over it and vapor mass fraction profile for these two cases are overlapping. However, after the vapor is transported to the upper wall, the mass fraction

profile for the vapor species is perpendicular to the upper wall, which represents the physics that no vapor of wall film pass through the bounded wall and mass flux is equal to zero, and the evaporation rate of wall film decreases due to this restriction as indicated in Figure 5.6 (b).

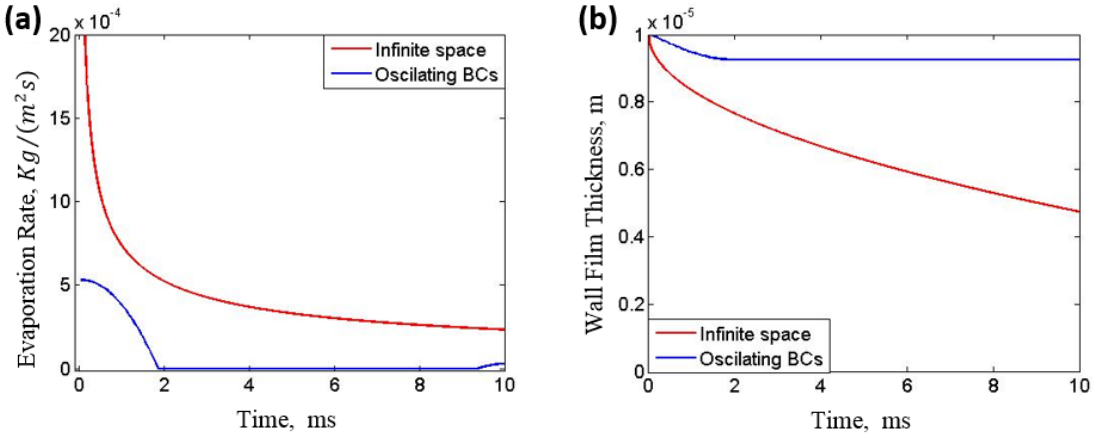

Figure 5.7: Comparison of evaporation rate and wall film thickness for the evaporation of liquid wall film in an infinite stationary gas medium (case-I) and with oscillating boundary conditions (case –III).

The evaporation rate and wall film thickness as function of time for case-I and case-III are compared in Figure 5.7. The average of evaporation rate for case – III is smaller than case-I, which can be proved by the thicker film thickness with same evaporation time interval as shown in Figure 5.7 (b). Due to the oscillation of vapor mass fraction on the gas/liquid interface, negative vapor mass fraction gradient can appear in a fraction of the oscillation period, which can prevent the evaporation of wall film into the ambient gas medium.

5.2 Evaporation in Laminar Flow Conditions

5.2.1 Computational Problem

A two dimensional numerical simulation is carried out for the study of the evaporation of liquid wall film in laminar flow conditions in the present study, and the computational domain is displayed as the dash rectangle in Figure 5.8. A liquid wall film with initial thickness of H_0 is introduced into the computational domain under the high temperature gas stream. The width of the computational domain is chosen to be more than ten times larger than the boundary layer thickness in the gas stream flowing over the whole length of evaporating liquid wall film, and this domain is considered large enough to ensure the development of the boundary layer over the evaporating liquid wall film.

The flow conditions in the engines are quite complex and varies with the engine speeds and the design of the intake port. The velocity of gas stream varies in the range of 5m/s to 40 m/s depending on the rotating speed of engines, and here the Reynolds number of the gas stream at the inlet of the computational domain, $Re_{g,\infty}$, equals to 1.7×10^4 is chosen to examine the evaporation characteristics under laminar flow conditions. Other parameters used for this numerical study can be found in Table 5.3.

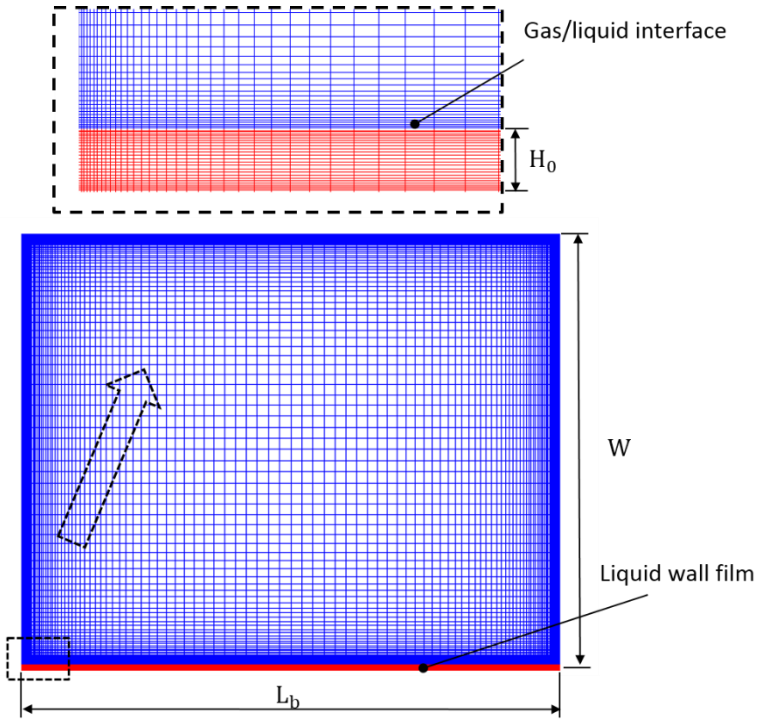

Figure 5.8: A schematic of the computational domain and meshes of evaporating liquid wall film in laminar flow conditions

Table 5.3: Parameters used for the numerical study of the evaporation of liquid wall film in laminar flow conditions

Parameters	Values
Initial film thickness, H_0 (mm)	0.25
Length of the liquid wall film, L_b (mm)	25
Width of the gas stream in the computational domain, W (mm)	20.25
Reynolds number of the gas flow at the inlet, $\mathrm{Re}_{g,\infty}$	1.7×10^4
Initial gas phase temperature, T_g (K)	1000
Initial liquid wall film temperature, T_l (K)	300
Wall surface temperature, T_W (K)	400

5.2.2 Laminar Evaporation Model Validation

The evaporation model of liquid wall film under a laminar air stream is validated, and three different cases are employed for the model. Firstly, the evaporation of liquid wall film in a stationary gas medium is used for the validation of the species diffusion process in the stagnant environment. Then, the experimental results of flow fields of the laminar air stream over the evaporating liquid wall film in a rectangular flow channel [148, 149] are employed for the validation of the momentum transport of the air stream. Finally, the experimental results of the evaporation mass fraction of oil film under a laminar air stream in the flow channel are used to validate the laminar evaporating model.

For the validation of the transient species transport process of the evaporating liquid wall film, the liquid wall film is considered evaporating in a stationary air environment in a finite space (Case a) and with oscillating boundary conditions (Case b). The surface of wall film is assumed to be flat; and the evaporation process is simplified to a one-dimensional species diffusion from the instantaneous gas/liquid interface (at $y = H$) to into the gas phase. The analytical evaporation model with its pertinent initial and boundary conditions of the validation cases can be found in Section 5.1.

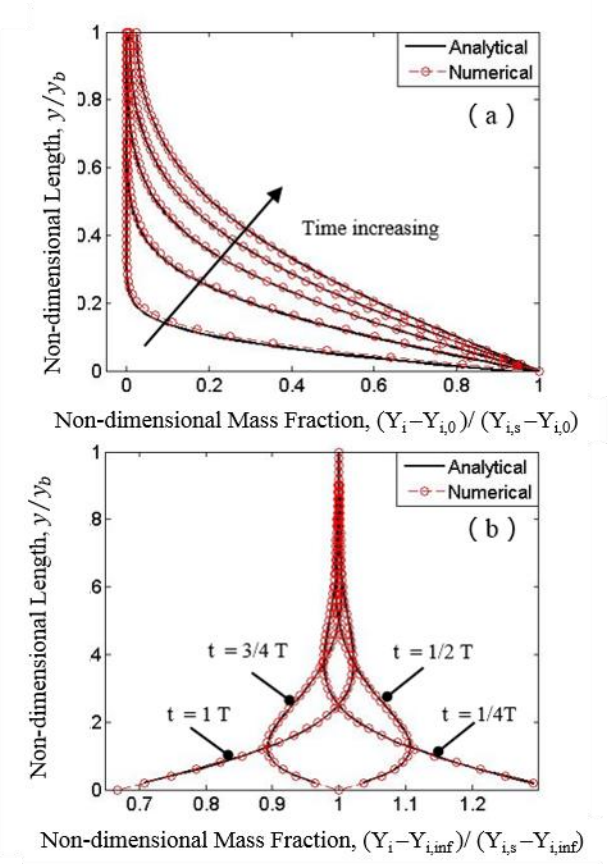

Figure 5.9: Non-dimensional vapor mass fraction profiles for the evaporation of wall film in a stationary air environment with diffusion coefficient equals to D in a finite space (a) with y_b the width of the air space above the liquid film at five different non-dimensional time $t^* = Dt/y_b^2 = 11.52, 57.60, 115.20, 178.20$ and 230.40; with oscillating boundary vapor concentration at oscillation period of T at the gas/liquid interface and the y direction in the air medium extended to infinity (b) at four different time t = ¼T, ½T, ¾T and 1T. Line represents the analytical results whereas symbols represent numerical results.

Figure 5.9 compares the numerical and analytical non-dimensional vapor mass fraction profiles for the evaporation of one component wall film in a stationary air environment in a finite space (a) and with oscillating boundary condition on the gas/liquid interface (b). As observed, for both of these two cases, the present numerical results show good agreement with the analytical results at all the

evaporation time instants. It may therefore be concluded that the present numerical model is reasonably accurate for the study of the evaporation and species transport of evaporating wall film.

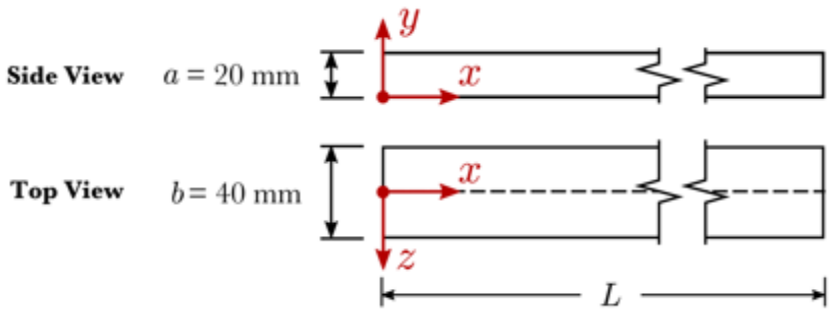

Figure 5.10: Geometry dimension and coordinates of the experimental set up of the experimental measurement of the flow filed in the flow channel [149].

The characteristics of the flow field over the evaporating liquid wall film is crucial for the study of the evaporation process of the liquid wall film under the high speed air stream, and thus the momentum transport in the evaporation model is also validated through comparing the experimental results of velocity fields from the work of Bruck [148] with that of numerical predictions. Figure 5.10 shows the schematic figure of experimental set up and geometry parameters of the measurement of the flow field. In the experimental study, the flow field in a rectangular flow channel with the width/ height ratio 0.5 is measured using both the PIV and hot-wire methods. The experimental measurement is conducted at a constant temperature at both the wall and air temperatures of 19 ± 1 ℃. The detailed of geometry parameters of the experimental set up and the experimental conditions are tabulated in Table 5.4.

Table 5.4: Geometry parameters and experimental conditions for the experimental measurement of flow field under a laminar air stream [148,149].

Parameters	Values
Length of the flow channel, $L\ (mm)$	900
Height of the flow channel, $a\ (mm)$	20
Width of the flow channel, $b\ (mm)$	40
Temperature of inlet air flow, $T_a\ (K)$	292 ± 1
Inlet velocity of the air flow, $U_\infty\ (m/s)$	10 ± 0.45
Turbulence intensity of the air flow, $I_\infty\ (\%)$	0.68 ± 0.000136

The numerical study is carried out with the same geometry set up as the experimental measurements; and the properties of dry air at temperature of 19 ℃ is used in the numerical simulations, which is listed in Table 5.5. The numerical model is validated through comparing the numerical predicted non-dimensional velocity profiles and the shape factors of the gas flows along the flow channel with that of experimental results as displayed in Figure 5.11 and Figure 5.12.

Table 5.5: Properties of dry air at 19 ℃

T (K)	ρ $(\mathrm{kg/m^3})$	v $(10^{-5}\mathrm{m^2}/s)$	μ $(10^{-5}\,\mathrm{kg}/ms$	k $(10^{-5}\mathrm{W/mK}$	c_p $(\mathrm{kJ/kgK})$	Pr
292	1.211	1.496	1.807	2.561	1.0045	0.709

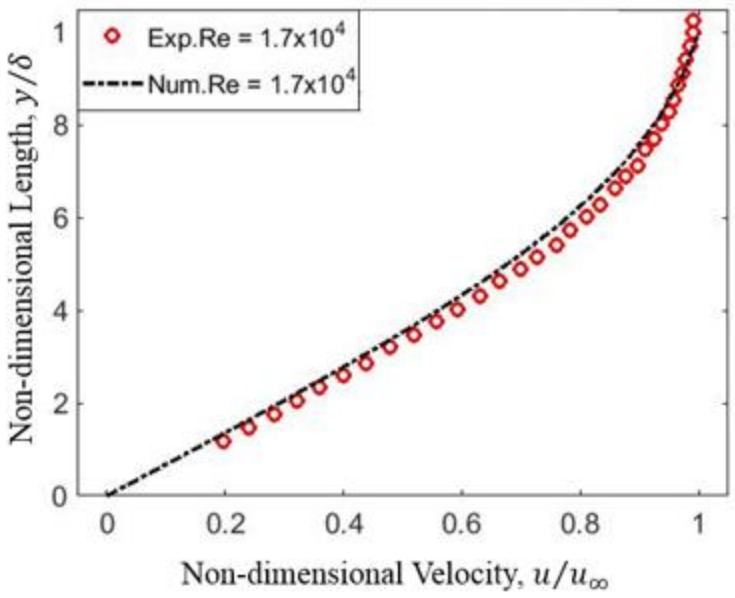

Figure 5.11: Model validation: non-dimensional velocity profiles for the laminar flow conditions in the flow channel at Reynolds number of 1.7×10^4 with symbols representing experimental results and dash line representing numerical simulation as indicated in the legend.

Figure 5.11 compares the non-dimensional velocity profile predicted from the numerical predictions with the corresponding experimental results. As observed, the numerical results can match the experiential results very well, which demonstrate that the numerical model used in the present study can predict the velocity field accurately.

Conventionally, the shape factor can be used in the boundary layer flow to determine the nature of the flow, which is defined as

$$\mathrm{H} = \frac{\delta^*}{\theta} \tag{5.17}$$

in which, $\delta^* = \int_0^\infty (1 - \frac{u(y)}{u_0}) dy$, representing the displacement thickness; and $\theta = \int_0^\infty \frac{u(y)}{u_0} (1 - \frac{u(y)}{u_0}) dy$, standing for the momentum thickness. Typically, $\mathrm{H} = 2.59$ represents a typical laminar

flow, while H $= 1.4 - 1.65$ stands for a turbulent flow. In the present study, the presence of turbulence intensity in the air flow over the evaporating liquid wall film, which is characterized by the shape factor, has been considered to be a significant factor that can affects the evaporation of the liquid wall film. Thus, the shape factor is used, in the present study, to characterize the air flows over the evaporating liquid wall film and to validate the numerical simulation models.

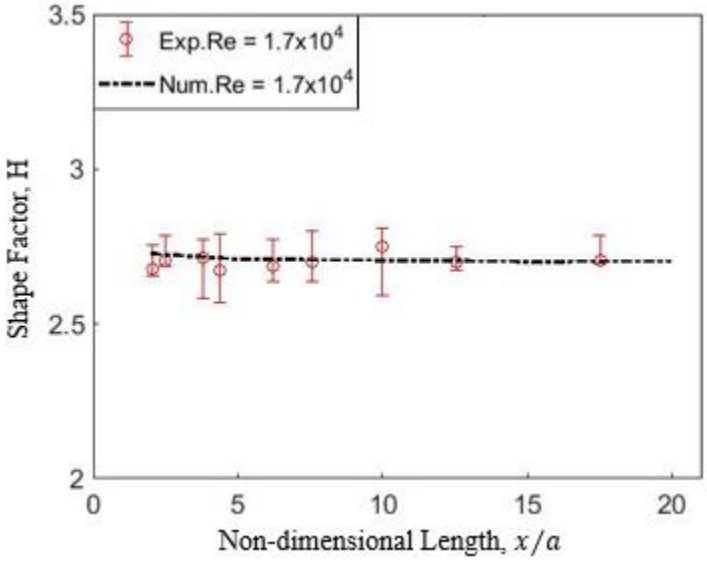

Figure 5.12: Model validation: shape factors along the flow channel for laminar flow conditions at Reynolds number of 1.7×10^4 with symbols representing experimental results and dash line representing numerical simulation as indicated in the legend.

Figure 5.12 compares of numerical results of shape factors along the flow channel for laminar flow conditions with relevant experimental results with the flow conditions as displayed in the legend. It is clear that the numerical model can match the experiential results accurately, which further prove that the numerical model adopted in this study is suitable for the prediction of flow field of laminar flow conditions over the evaporating liquid wall film.

Finally, the evaporation model is validated through comparing the predicted evaporation mass fraction of evaporating Lub oil under a laminar air stream with that of experimental results from Stephen et.al [148, 149]. In the experimental measurement, the oil film sample with thickness of 50 μm is placed under a laminar air stream in a rectangular flow channel. The oil film is heated by a cartridge heater (Omega CIR- 1014/120) and the temperature of oil sample is uniform along the film thickness and keeps constant at , T_f , which is controlled by a PID controller with an FPGA (NI-cRIO - 9074) and a digital IN module (NI 9375). The evaporation mass loss of the oil sample is measured by the Sartorius analytical balance (MSE125P -10_DU) with the accuracy of 10 µg. The experimental set up is displayed in Figure 5.13 and the detailed geometry parameters can be found in Table 5.5. In the numerical simulation, the geometry of the numerical model are the same as the experimental set up, and the numerical results of evaporation mass fraction of oil film under three different air stream velocity (Reynolds number) are compared with that of experimental results as shown in Figure 5.14.

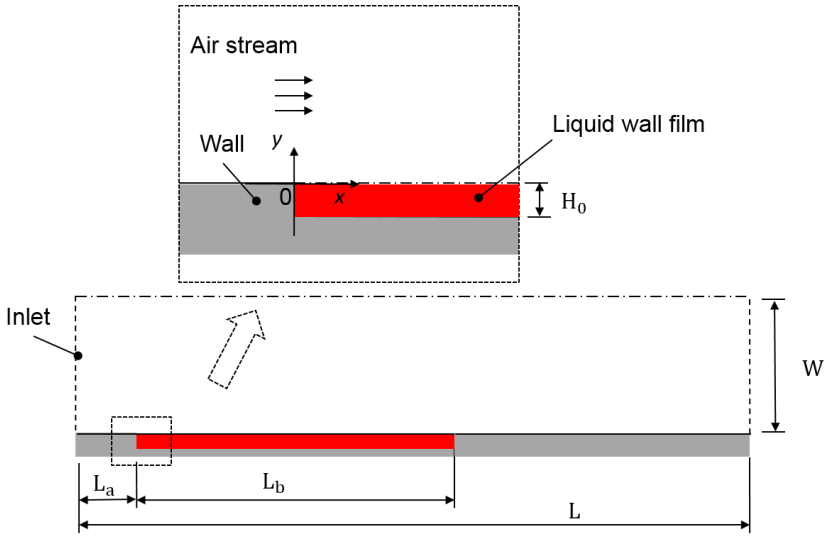

Figure 5.13: Geometry dimension and coordinates for the experimental measurement of the evaporation of oil film in the flow channel with DISI engine-like flow conditions [149].

Table 5.6: Geometry parameters and experimental conditions for the experimental measurement of oil evaporation under a laminar air stream [149].

Parameters	Values
Initial film thickness, $H_0(mm)$	0.05
Length of the liquid wall film, $L_b(mm)$	25
Length of the leading edge, $L_a(mm)$	40
Length of the gas stream in the computational domain, $L\ (mm)$	900
Width of the gas stream in the computational domain, $W(mm)$	20
Width of the liquid wall film in the flow channel, $c(mm)$	25
Temperature of air flow, $T_a\ (K)$	292 ± 2
Temperature of oil film, $T_f\ (K)$	423 ± 2.5
Temperature of thermal base, $T_b\ (K)$	$481\ \pm 2.5$
Inlet velocity of the air flow, $U_\infty\ (m/s)$	$5 \pm 0.225, 10 \pm 0.45,$ 15 ± 0.675
Turbulence intensity of the air flow, $I_\infty\ (\%)$	0.68 ± 0.000136

Figure 5.14 compares numerical predictions and experimental results of the evaporation mass fraction of oil film under a laminar gas flow conditions with three different Reynolds number, $\mathrm{Re} = 1.0 \times 10^4,\ 1.7 \times 10^4$ and 3.5×10^4. It is clear that the numerical model can predict the experiential results with good accuracy for all three flow conditions, which indicate that the numerical model is capable for the study and characterization of the evaporating liquid wall film under laminar flow conditions.

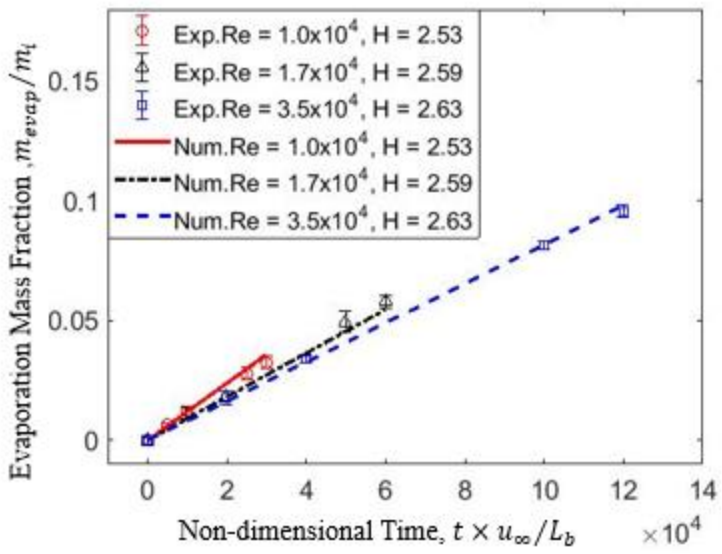

Figure 5.14: Model validation: evaporation mass fraction of oil under laminar flow conditions with c the width of the experimental flow channel at three different Reynolds number$\mathrm{Re} = 1.0 \times 10^4,\ 1.7 \times 10^4$ and 3.5×10^4.

5.2.3 Evaporation Characteristics in Laminar Flow Conditions

Figure 5.15 shows stream lines, isothermals and mass fraction contours at two different evaporation phases $t^* = 0.4$ (a) and 2.0 (b) with temperature ranging from 300K to 1000K and vapor mass fraction ranging from 0 to 0.9. It can be seen from the stream lines and flow field vectors in the liquid phase that the liquid wall film starts to move and to evaporate after the high temperature air stream flow over it; and the temperature and species boundary layers are developed along the wall film with time increases.

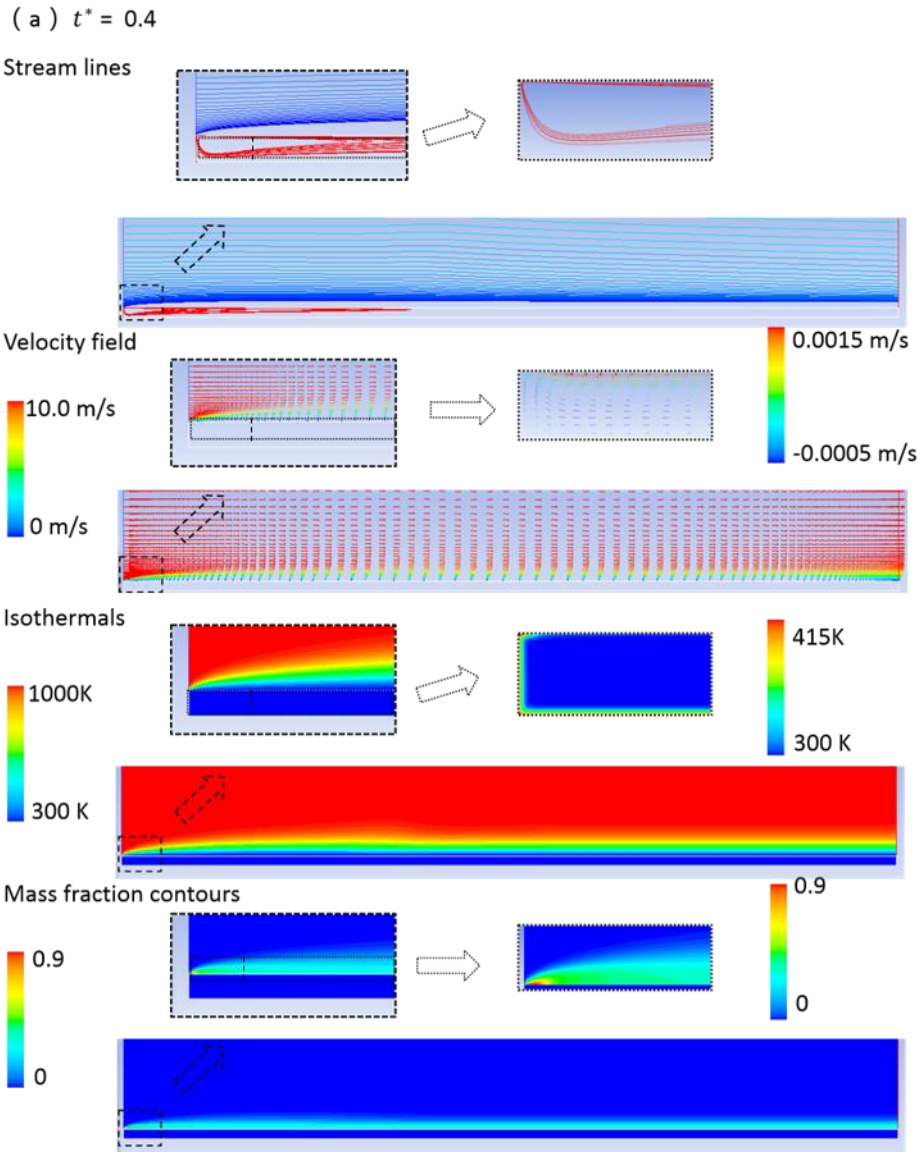
(a) t^* = 0.4
Stream lines
Velocity field
10.0 m/s
0 m/s
0.0015 m/s
-0.0005 m/s
Isothermals
1000K
300 K
415K
300 K
Mass fraction contours
0.9
0
0.9
0

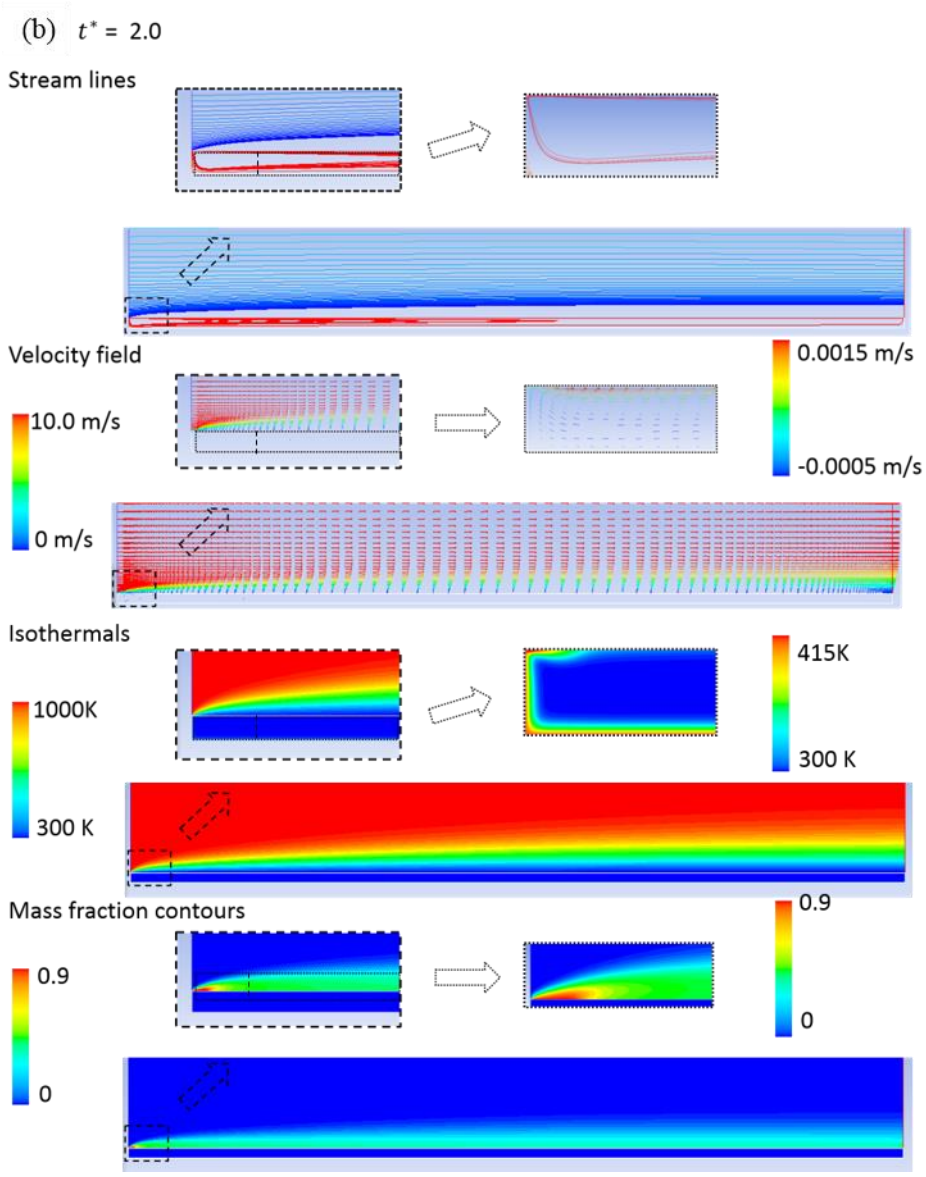

Figure 5.15: Stream lines, isothermals and mass fraction contours of the evaporation of liquid wall film in a laminar flow at $\mathrm{Re}_{g,\infty} = 1.7 \times 10^4$ and $T_\infty = 1000\mathrm{K}$ in two different evaporation phase at two different non-dimensional time of $t^* = 0.4$ (a) and 2 (b) with temperature ranging from 300K to 1000K and vapor mass fraction ranging from 0 to 0.9.

As observed in the contour plot of the temperature of vapor mass fractions, the thickness of thermal and species boundary layer increase along the evaporating wall film, especially at the late phase of the evaporation ($t^* = 0.4$), which indicates the species gradient and consequently evaporation

mass flux is non-uniform and decreases along the wall film in the stream-wise (x) direction. Also, a stable thermal and species boundary layer are built up at the late phase of evaporation, which means that the wall film vaporizes in a quasi-steady state with constant evaporation rate at the late phase of the transient evaporation process. High concentration of vapor is formed at the gas/liquid interface compared to the free gas stream; and a large mass fraction gradient is observed within the species boundary layer near the interface. It is worthy to mention that the liquid phase wall film starts to move based on the streamlines in Figure 5.15 even at the early stage of evaporation, which can enhance the liquid heating, which would further boost the evaporation as shown in following section.

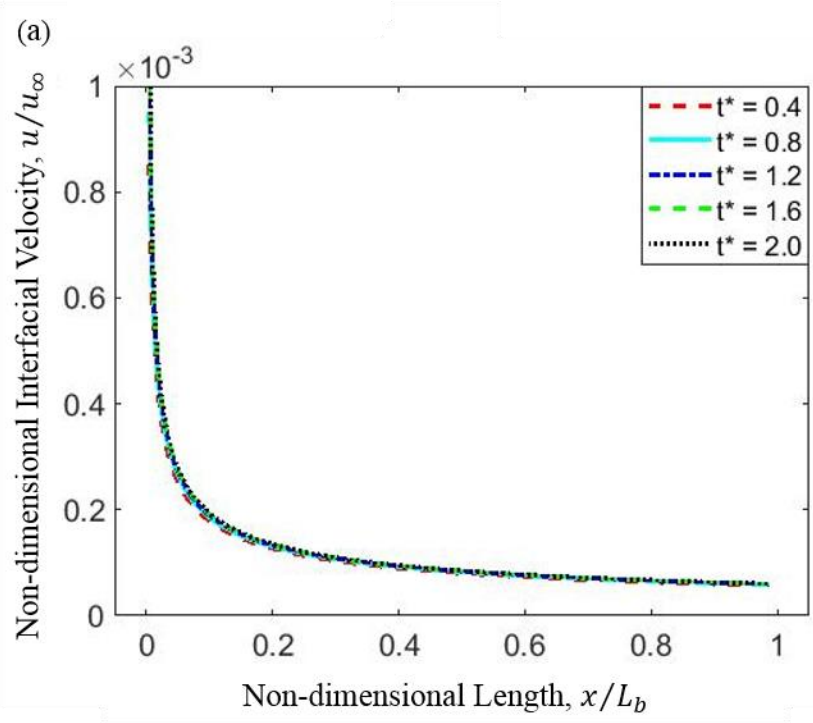

(b)

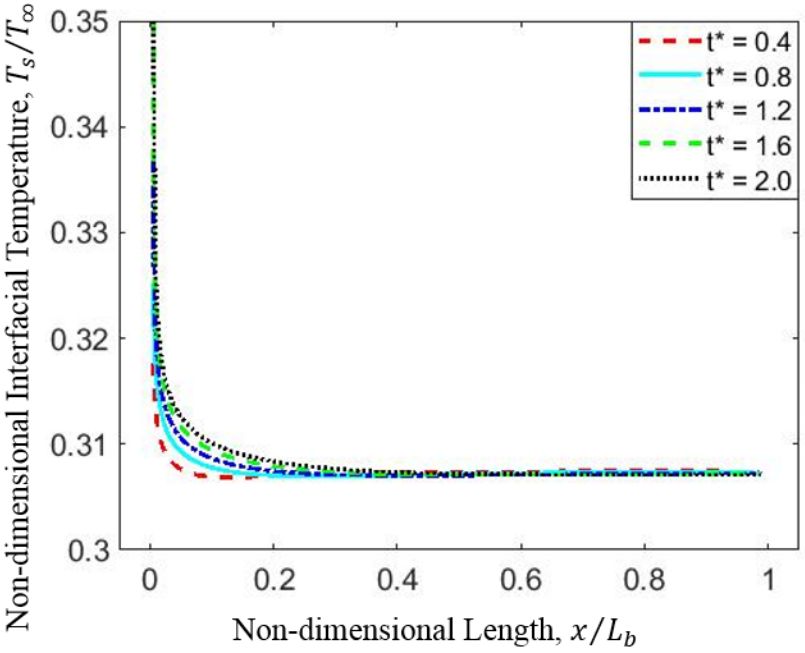
Non-dimensional Interfacial Temperature, T_s/T_∞
0.35
0.34
0.33
0.32
0.31
0.3
0
0.2
0.4
0.6
0.8
1
Non-dimensional Length, x/L_b
t* = 0.4
t* = 0.8
t* = 1.2
t* = 1.6
t* = 2.0

(c)

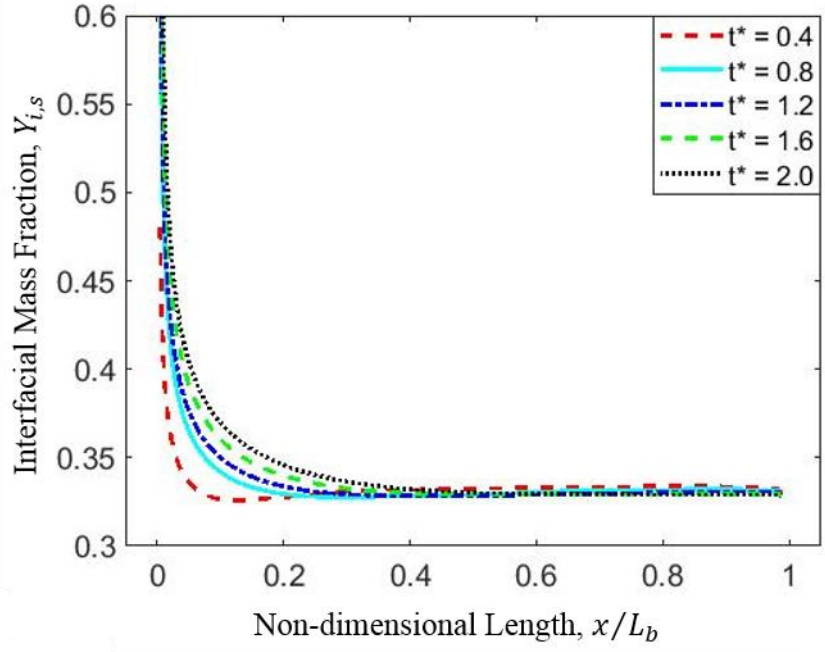
Interfacial Mass Fraction, $Y_{i,s}$
0.6
0.55
0.5
0.45
0.4
0.35
0.3
0
0.2
0.4
0.6
0.8
1
Non-dimensional Length, x/L_b
t* = 0.4
t* = 0.8
t* = 1.2
t* = 1.6
t* = 2.0

Figure 5.16: Non-dimensional local interfacial velocity at x-direction (a), temperature (b) and mass fraction (c) histories along the evaporating liquid wall film at five different time $t^* = 0.4, 0.8, 1.2, 1.6 \text{ and } 2.0$.

Figure 5.16 (a) demonstrates that local interfacial velocity at x-direction decrease along the evaporating liquid wall film at all five different time points in this study. This is reasonable, since the temperature gradients within the thermal boundary layer of the gas phase, representing the energy transfer rate from the high temperature air flow to the low temperature liquid wall film, declines along the evaporating liquid wall film. It can be also observed that the liquid wall film closer to the inlet of the high temperature air stream is heated up more quickly, which further led to relatively higher local interfacial temperature. Moreover, with evaporation time increasing, the interfacial temperatures increase as a results of heat transfer from the gas phase to the liquid wall film, which would also increase the interfacial vapor mass fraction as demonstrated in Figure 5.16 (b).

Figure 5.16 (c) shows that the local interfacial mass fractions of fuel vapor decrease along the evaporating liquid wall film at five different evaporation time points; and the peak value of the mass fraction along the evaporating liquid wall film is close to the leading point of the evaporating liquid wall film. This is because that evaporation process is a self-inhibit process; and at the leading point of the evaporating wall film, the high heat transfer rate would lead to higher evaporation rate, and the increased evaporation rate can consume more energy caused by the enthalpy difference of the evaporating liquid wall film, thus the peak values of interfacial mass fraction occurs close to the leading edge of the liquid wall film according to the thermodynamics equilibrium.

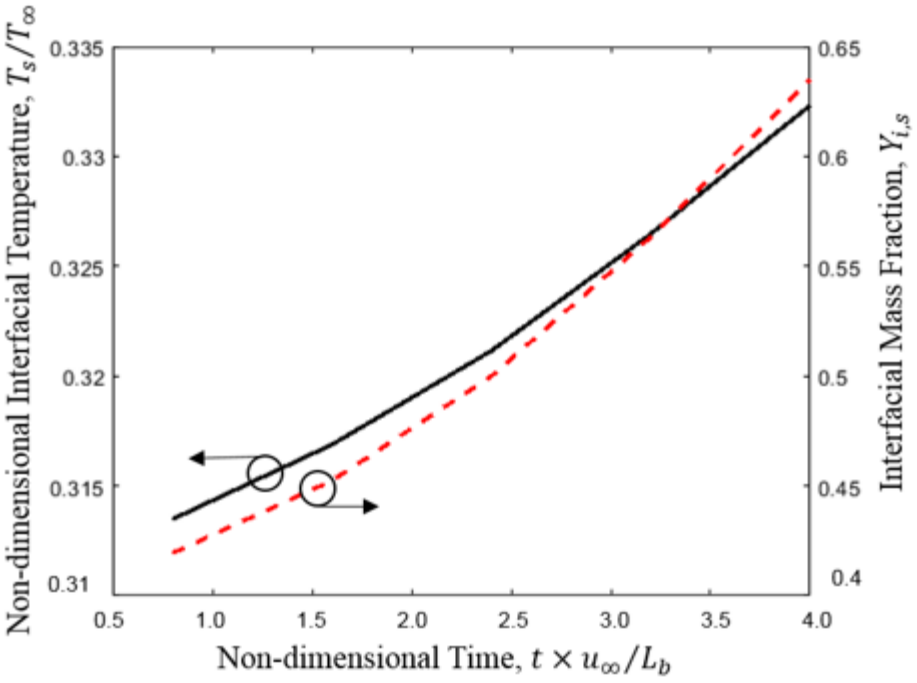

Figure 5.17: Averaged interfacial temperature and vapor mass fraction histories. Black line representing the averaged interfacial temperature whereas red dash line representing averaged interfacial mass fraction.

Figure 5.17 shows that the averaged interfacial vapor mass fraction and temperature have a similar trend with time increasing, and the averaged valued of temperature and mass fraction increases with time increasing. Also, the increasing extent of mass fraction is much more significant than that of the interfacial temperature. This is reasonable, since the interfacial vapor pressure is an exponent function of local temperature as shown in the Clausius-Clapeyron equation, Equation (3.39); and the vapor mass fraction increases slowly when temperature is much lower than the boiling temperature, while it increases very quickly when the temperature of liquid wall film close to the boiling temperature (at the late phase of evaporation).

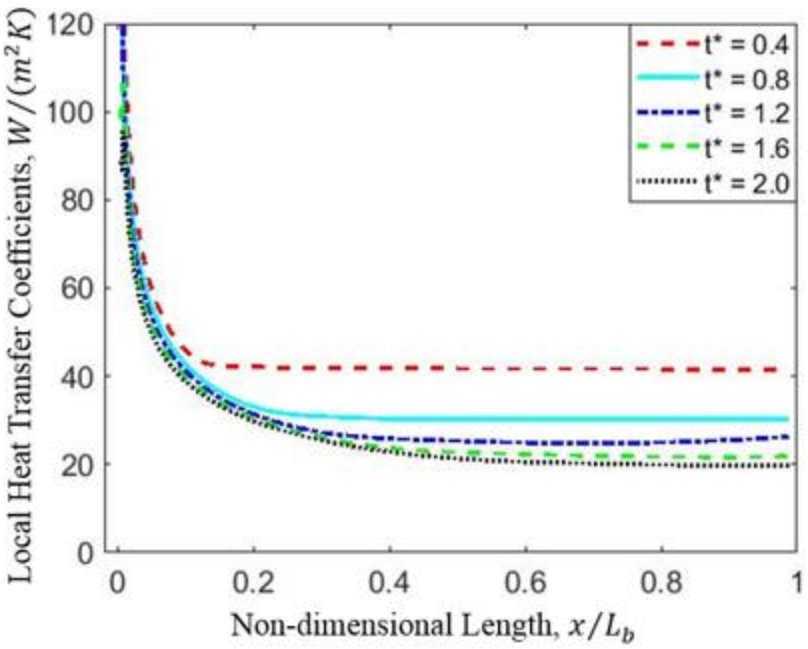

Figure 5.18: Local heat transfer coefficient h_x along the evaporating liquid wall film at five different time $t^* = 0.4, 0.8, 1.2, 1.6$ and 2.0.

Figure 5.18 shows that the local heat transfer coefficients, as an indicator of heat transfer rate from the gas phase to the liquid phase, decreases along the evaporating liquid wall film, which is consistent with the results of isothermal contour in Figure 5.15. Also, as time increasing, the heat transfer rate from the gas phase to the liquid increases, but the increasing magnitude is small due to the inherent self-inhibit phenomena of evaporation.

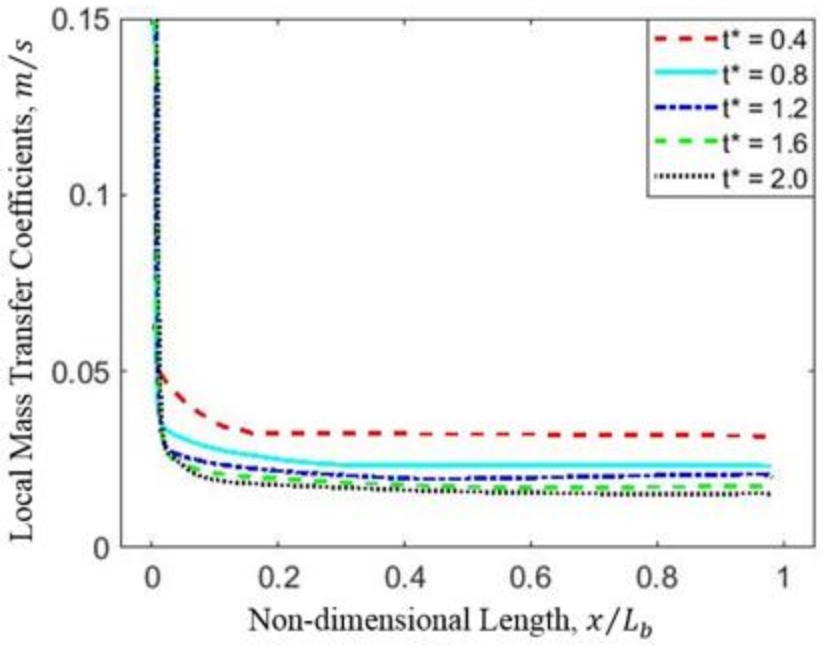

Figure 5.19: Local mass transfer coefficient h_m along the evaporating liquid wall film at five different time $t^* = 0.4, 0.8, 1.2, 1.6$ and 2.0.

Figure 5.19 shows that the trend of mass transfer coefficients along the evaporating liquid wall film at different time points is similar to that of heat transfer coefficients, which can be attribute to the analogy between heat and mass transfer. Also, it is also obvious that the increasing magnitude of mass transfer coefficient is more significant than that of heat transfer as time increasing; and this is because the interfacial mass fraction increases much quickly at the late phase of evaporation, and liquid heating and liquid motion can also contribute to the enhance of the evaporation.

Based on physical reasoning and theoretical justification, the mass transfer results of evaporating liquid wall film under air streams with different flow conditions could be correlated in the form of [139, 179 - 188]

$$\mathrm{Sh_f}\, E_M = \mathrm{C} + \ C_M \mathrm{Re_g^m Sc_g^n} \tag{5.18}$$

in which, E_M represents the "blowing effects", which is caused by the motion of evaporating vapor from the gas/liquid interface to the gaseous flows. E_M is a function of and primarily depends on the mass transfer number, B_M, which can be defined as

$$B_M = \left(\mathrm{Y_{i,s}} - \mathrm{Y_{i,\infty}} \right) / \left(1 - \mathrm{Y_{i,s}} \right) \tag{5.19}$$

which indicates the ratio of driving to resisting potentials for vaporization and strongly dependents on the interfacial temperature, T_s . The thermo-physical properties of the gas mixture are evaluated at a reference temperature and concentration, which can be estimated by:

$$T_f = T_s + r\,(T_\infty - T_s) \tag{5.20}$$

$$X_{i,f} = X_{i,s} + r\,(X_{i,\infty} - X_{i,s}) \tag{5.21}$$

In this study, the widely used film condition, denoted by subscript f, is used for the calculation of the reference temperature and concentration; and the r value is chosen to be 0.5 in both Equation (5.20) and (5.21). The mixing law for the calculation of the properties of the gas mixture is tabulated in Appendix A.

The local mas transfer coefficient, $\mathrm{h_{m,x,}}$ and the corresponding averaged mass transfer coefficient over the length of the liquid wall film, $\overline{\mathrm{h}}_{\mathrm{m,L}}$ are defined in the conventional manner as

$$\left[\mathrm{h_{m,x}} \rho_s \left(Y_{i,s} - Y_{i,\infty} \right) \right]_x = \left[-\rho_s D_s (\partial Y_i / \partial y) \right]_x \tag{5.22}$$

$$\overline{\mathrm{h}}_{\mathrm{m,L}} = \frac{1}{\mathrm{L}} \int_0^{\mathrm{L}} \mathrm{h_{m,x}}\, \mathrm{dx} \tag{5.23}$$

where the subscript x denotes the local location in the flow direction along the evaporating liquid wall film. The local mass transfer coefficients are calculated from the local vapor concentration gradients, which can be obtained from the numerical results. Afterwards, the averaged mass

transfer coefficients over the evaporating liquid wall film with the length of L can be calculated using Equation (5.23). Then, the averaged Sherwood number can be computed as:

$$\overline{\mathrm{Sh}_\mathrm{f}} = \frac{\bar{\mathrm{h}}_{\mathrm{m,L}}\,\mathrm{L}}{\mathrm{D}_\mathrm{f}} \tag{5.24}$$

in which, the diffusion coefficient of the fuel vapor in the gas mixture is estimated with the referenced temperature, T_f .

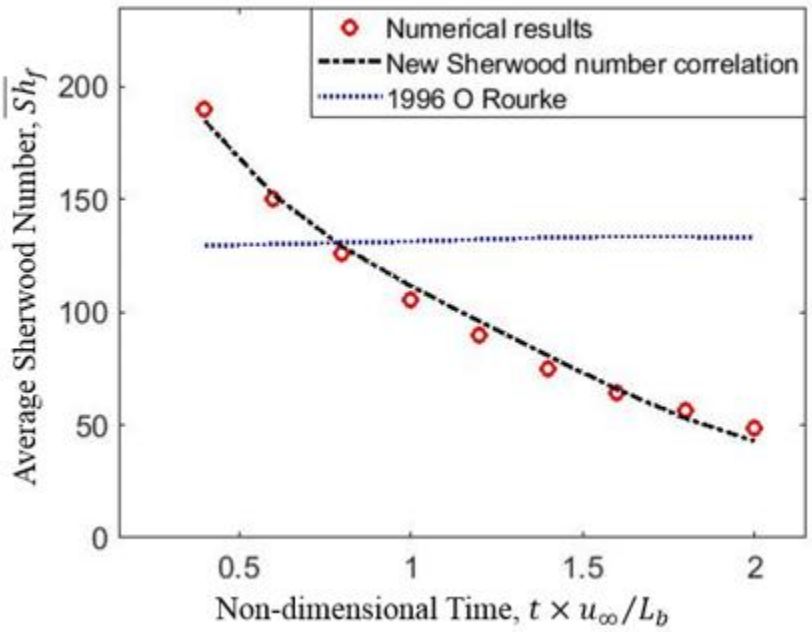

Figure 5.20: Comparison of the averaged Sherwood number history of the evaporation of liquid wall film in laminar gas flow at $\mathrm{Re}_{g,\infty} = 1.7 \times 10^4$ and $T_\infty = 1000\mathrm{K}$ with existing mass transfer correlation and numerical results at the same flow condition; the new and existing Sherwood number correlations shown in the figure are given in Equation (5.25) and Equation (5.26), respectively

Five different flow conditions are considered in this study for the development of the mass transfer correlation of evaporating liquid wall film in laminar flow conditions; and the case numbers and flow conditions are listed in Table 5.7. The gaseous phase averaged Sherwood number at nine

different non-dimensional time instants are calculated during the transient evaporation process of the liquid wall film; and the numerical results are listed in Table E.1.1 and E.1.2.

Table 5.7: Calculated cases and flow conditions of the evaporating liquid wall film in laminar gas flows studied in the present study.

Case Number/ #	1	2	3	4	5
$\mathrm{Re}_{g,\infty}$	8.5×10^3	1.7×10^4	3.4×10^4	5.1×10^4	6.8×10^4

Figure 5.20 compares the history of the newly developed averaged mass transfer correlation, $\overline{\mathrm{Sh}_\mathrm{f}}$, with the existing mass transfer correlation proposed by O Rourke (1996) and the numerical results at the same flow condition. The newly developed Sherwood number is calculated using the instantaneous values to represent the transient evaporation process of the liquid wall film; therefore, the new mass transfer correlation is plotted as a function of time to explicitly show the physically meaningful of the comparison. It can be seen that the Sherwood number correlation shown in the figure,

$$\overline{\mathrm{Sh}_\mathrm{f}}[\,\mathrm{B_M}/(1+\,\mathrm{B_M})]^{3.7} = 1 + \,0.0155\mathrm{Re}_\mathrm{g}^{0.534}\mathrm{Sc}_\mathrm{g}^{1/3} \tag{5.25}$$

agrees very well (within 5%) with the numerical results of the transient evaporation of liquid wall film in laminar gas flows. However, the existing mass transfer correlation, displayed in Equation (5.26), cannot capture the variation of the averaged Sherwood number of the evaporating liquid wall film during its evaporation process; and the mass transfer Sherwood numbers predicted by the existing mass transfer correlation

$$\overline{\mathrm{Sh}_\mathrm{f}} = 0.664\mathrm{Re}_\mathrm{g}^{0.5}\mathrm{Sc}_\mathrm{g}^{1/3} \tag{5.26}$$

remains almost a constant. Specifically, the existing mass transfer correlation under-predicts the Sherwood number by around 34.2% at the beginning of the evaporation process, and it over-predicts the Sherwood number by around 144.2% at the non-dimensional time point t^* equals to 2. This is reasonable, since the existing mass transfer correlation is only valid for steady state, and the variation of blowing effects during the transient evaporation process are totally ignored.

In Equation (5.26), the effects of blowing, convection and variable properties are all taken into account. Furthermore, the effects of liquid phase heating are also implicitly included in the newly developed mass transfer correlation, since all the thermo-physical properties are estimated at the reference temperature and concentration; and the mass transfer number B_M strongly depends on the gas/liquid interfacial temperature, which is directly affected by the liquid phase heating.

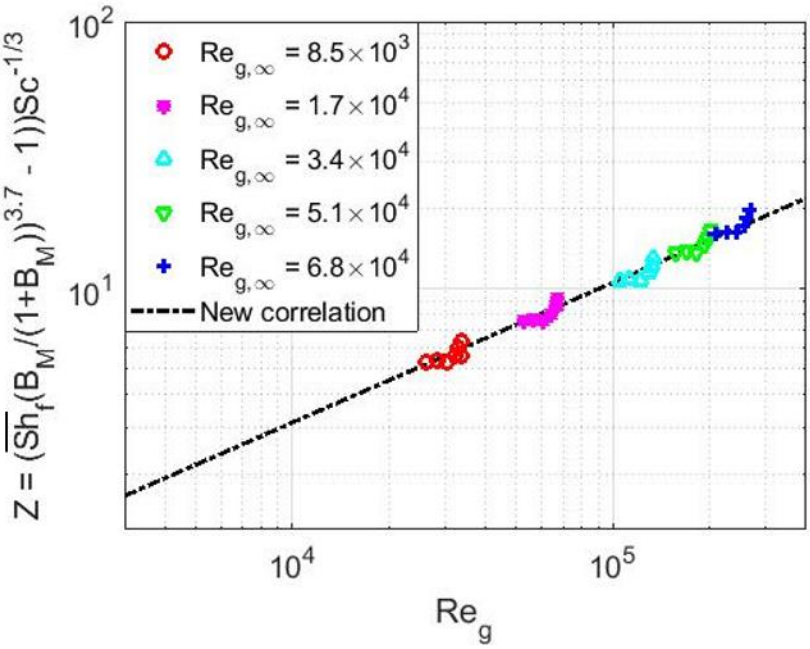

Figure 5.21: Comparison of the new Sherwood number correlation, $\overline{Sh}_f$, of the evaporating liquid wall film in laminar gas flows with numerical results; --: $Z = 0.0155Re_g^{0.534}$; symbols: data of numerical results.

Figure 5.21: compares the newly developed mass transfer correlation with the numerical results of the evaporation of liquid wall film in laminar flows at five different flow conditions as shown in Table 5.7. It is clear that the newly developed correlation can match the numerical results very well for all the five different flow conditions at all the different non-dimensional time instants. Also, it can be observed that for a certain flow condition, the averaged mass transfer number in the gas phase varies with time changing, which can be attributed to the variation of thermos-physical properties is nonlinear during the transient evaporation process.

5.3 Evaporation in Turbulent Flow Condtions

A two dimensional numerical simulation of the evaporating liquid wall film under a turbulent stream is carried out for the present study to characterize its evaporation process and determine its mass transfer correlation. The geometry parameters of the computational domain are the same as displayed in Figure 5.8, and the detailed of the domain can be also found in Table 5.3. One thing worth mentioning is that the near wall mesh needs to be fine enough (typically at $y^+ \approx 1$) and 10 – 20 layers of grids are needed within the viscous sublayer in order to resolve the transport of momentum, energy and species within the viscous sublayer.

Before performing the numerical study of the evaporation of liquid wall film under a turbulent air stream. An evaluation of the exiting near wall modeling approaches is conducted to identify the most suitable turbulence model for this numerical study, and the experimental results of the wall function of a steady turbulent air flow in a rectangular flow channel are employed for the turbulence model evaluation. Four different low-Reynolds number turbulence models, three different form of $k-\varepsilon$ models with enhanced wall treatment and the SST $k-\omega$ turbulent model is considered in the evaluation study of the turbulence models. The governing equations of these turbulence models

are described in Section 3.2.2; and the results are presented in Section 5.3.1. After the identification of the most suitable turbulence model, the turbulent evaporation model is validated though comparing the experimental results of non-dimensional velocity profiles, shape factors along the rectangular flow channel and the evaporation mass fraction of oil film under the characterized turbulent air flow with that of the numerical predictions. Finally, the evaporation of liquid wall film under the turbulent air stream is studied and the mass transfer correlation is derived based on the numerical results.

5.3.1 Turbulence Model Evaluation

In the low Reynolds number $k-\varepsilon$ turbulence model, the damping functions are introduced into to governing equations and the formula for the calculation of the turbulent viscosity to model the near viscosity properly. For the evaluation of low Reynolds number $k-\varepsilon$ turbulence models, four different turbulent model that are accessible to the numerical platform are considered, and they are Lam and Bremhorst (LB) [119], Launder and Sharma (LS) [120], Yang and Shih (YS) [125], Abe, Kondoh and Nagano (AKN)[126]. And the results for the evaluation of the low Reynolds number $k-\varepsilon$ turbulence models are presented in Figure 5.22.

The experimental results of law of the wall of a turbulent flow similar to that of our numerical study is employed here to help to identify the most suitable turbulence model. In the viscous sublayer ($y^+ \leq 5$), the viscous effects dominant the flows in the region and the velocity profiles is actually laminar, which can be written in a non-dimensional form as:

$$u^+ = y^+ \tag{5.27}$$

in which, u^+ is the non-dimensional stream-wise velocity, written as:

$$u^+ = \frac{u}{u_\tau} \tag{5.28}$$

u_τ is the normalized shear velocity at the wall, defined as:

$$u_\tau = \sqrt{\frac{\tau_w}{\rho}} \tag{5.29}$$

$y^+$is the non-dimensional distance from the wall, defined as:

$$y^+ = \frac{yu_\tau}{v} \tag{5.30}$$

In the region of $30 \leq y^+ \leq 200$, the turbulent effects dominant the flow and the expression of non-dimensional velocity profile collapses to a universal profile, known as log-law velocity profile. The experimental results of the velocity profiles in the logarithmic region is [149]:

$$u^+ = \frac{1}{\kappa}\ln(y^+) + B \tag{5.31}$$

in which, $\kappa = 0.41$ and $B = 5$.

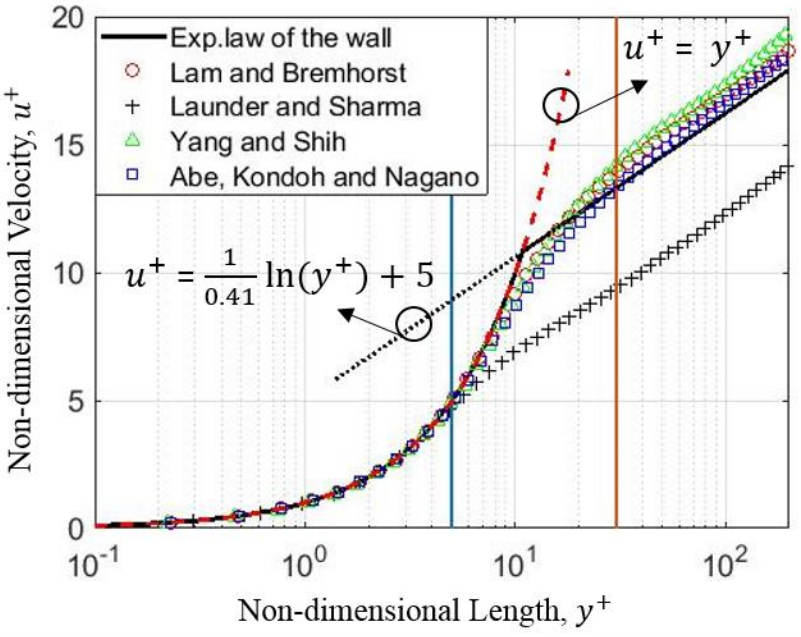

Figure 5.22: The comparison of the law of wall predicted from Lam and Bremhorst (LB), Launder and Sharma (LS), Yang and Shih (YS), Abe, Kondoh and Nagano (AKN) low Reynolds number turbulent model with the experimental data [149].

Figure 5.22 compares the law of wall predicted from four different low Reynolds number $k-\varepsilon$ model: Lam and Bremhorst (LB), Launder and Sharma (LS), Yang and Shih (YS), Abe, Kondoh and Nagano (AKN) with the experimental results [149]. It can be seen that the low Reynolds number $k-\varepsilon$ model can predict the law of wall very well in this study, and the only one exception is the Launder and Sharma (LS) model, which cannot predict the transient region (buffer region) in the law of wall properly. Moreover, the numerical results from AKN low Reynolds number model can match the experimental results with the best accuracy, which is considered to be the most suitable low Reynolds number $k-\varepsilon$ turbulence model for this study.

Since the standard $k-\varepsilon$ turbulence model is derived based on the assumptions that the flow is fully turbulence flow and the effects of molecular viscosity are negligible, some modifications

have been introduced to improve its performance. In this section, three most popular $k-\varepsilon$ models (Standard, RNG and Realizable) with enhanced wall treatment are evaluated, and the results are displayed in Figure 5.23.

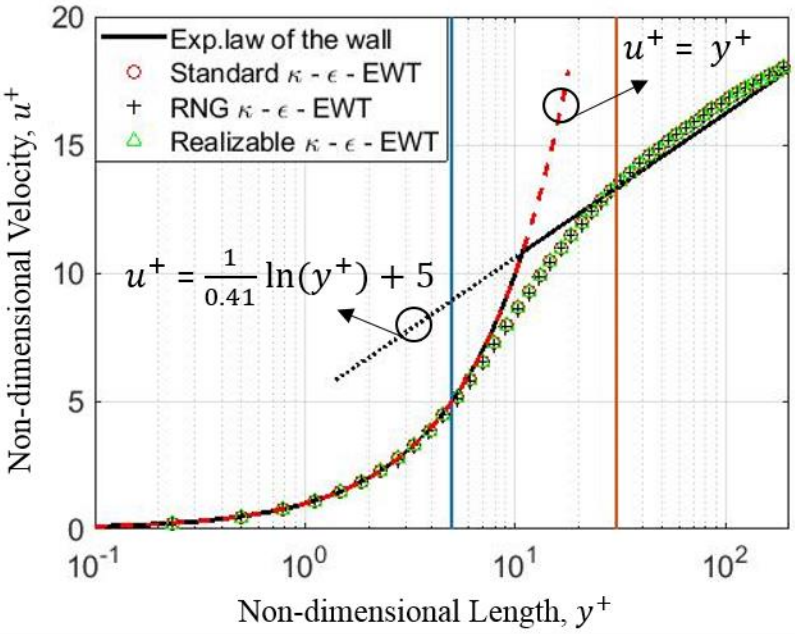

Figure 5.23: Comparison of the law of the wall predicted from Standard, RNG and Realizable $k-\varepsilon$ model turbulent model with the experimental data [149].

Figure 5.23 compares the law of wall predicted from Standard, RNG and realizable $k-\varepsilon$ model turbulent model with the experimental data. As observed, all the $-\varepsilon$ model with enhanced near wall treatment used in this study can give an accurate result of the law of the wall for the velocity. And the Standard $k-\varepsilon$ model with enhanced wall treatment is used in the present study, due to the simplicity of its numerical implementation.

Afterwards, a comparison between Standard $k-\varepsilon$ turbulent model with enhanced wall treatment, AKN low Reynolds number turbulence model and SST $k-\omega$ turbulent model is made to identify

the most suitable turbulence model to resolve the near wall turbulence viscosity in the present study.

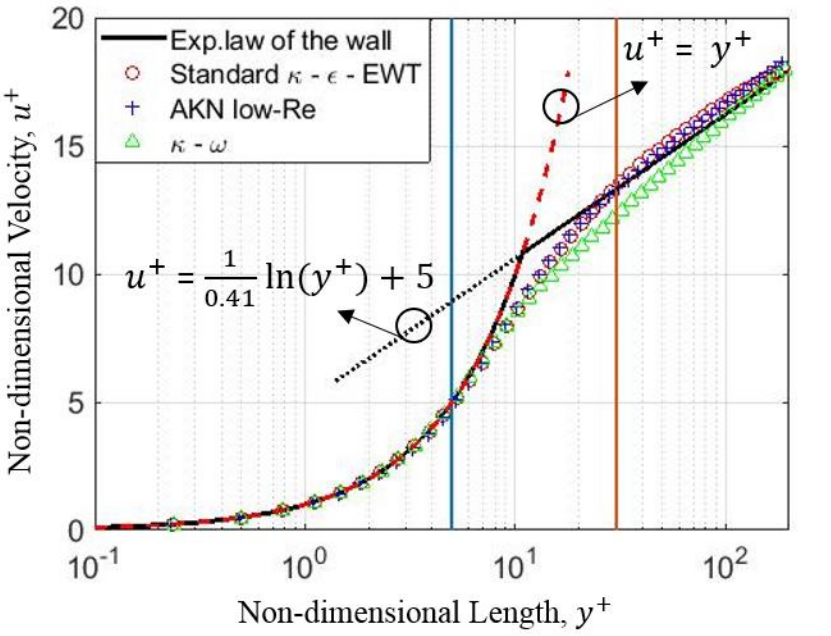

Figure 5.24: Comparison of the law of the wall predicted from Standard $k-\varepsilon$ turbulent model with enhanced wall treatment, AKN low Reynolds number turbulence model and SST $k-\omega$ turbulent model with the experimental results [149].

Figure 5.24 Comparison of the law of wall predicted from the Standard $k-\varepsilon$ turbulent model with enhanced wall treatment, AKN low Reynolds number turbulence model and SST $k-\omega$ turbulent model with the experimental results. It is clear that the standard model with enhanced wall treatment and AKN low Reynolds number turbulence model can predict the law of wall velocity profiles more accurately than the SST $k-\omega$ turbulent model. However, since the result of the Standard $k-\varepsilon$ model with enhanced wall treatment and AKN low Reynolds number

turbulence model are almost the same, a turbulence intensity sensitivity test are performed to identify the robustness of the these two turbulence model to identify the better model.

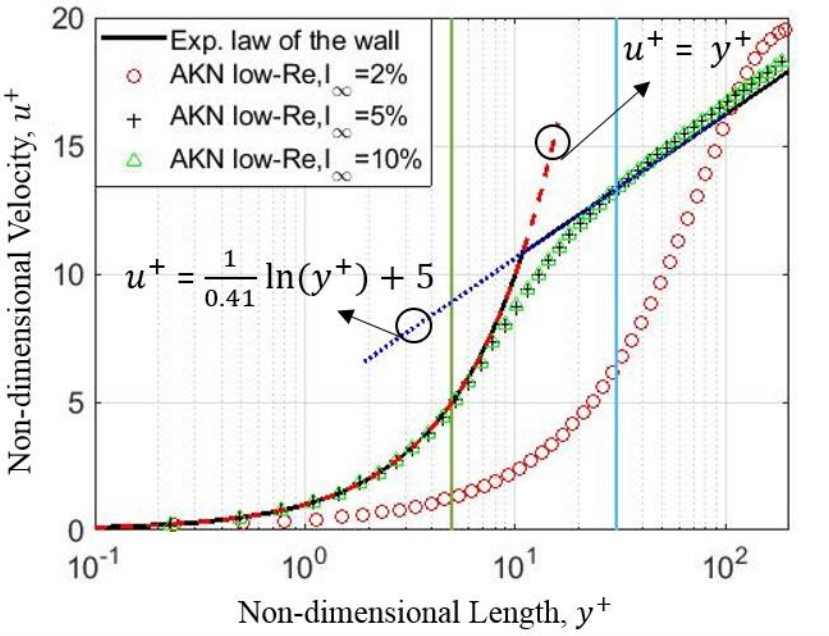

Figure 5.25: Turbulence intensity sensitivity test of the AKN low Reynolds number turbulence model with three different turbulence intensities 2%, 5%, 10% as indicated in the legend.

Figure 5.25 shows the turbulence intensity sensitivity test results of the AKN low Reynolds number turbulence model with three different turbulence intensities 2%, 5%, 10%. It is clear that the prediction of law of wall of velocity profiles from the AKN low Reynolds number turbulence model at turbulent intensity of 2% is not reasonable; thus, the AKN model is not considered to be the best model in this study.

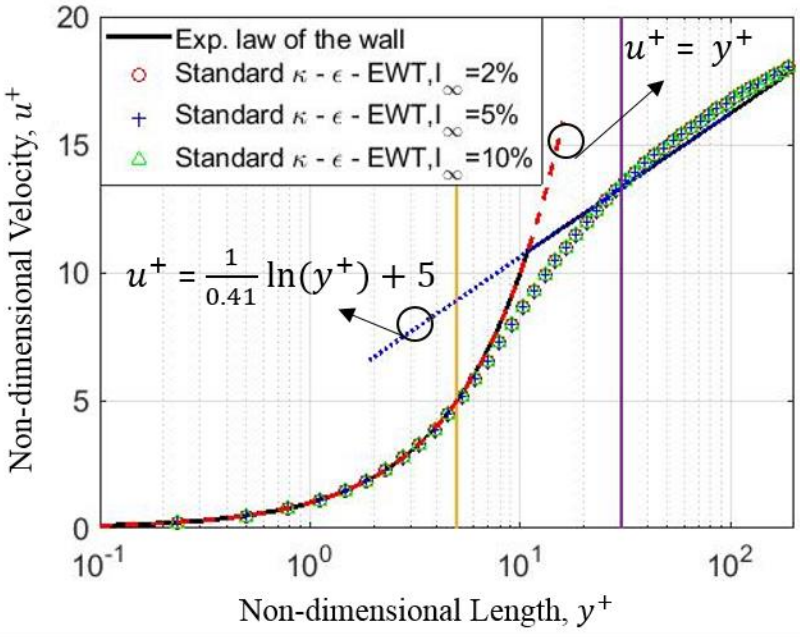

Figure 5.26: Turbulence intensity sensitivity test of Standard $k-\varepsilon$ turbulent model with enhanced wall treatment at three different turbulence intensities 2%, 5%, 10% as indicated in the legend.

Figure 5.26 displays the turbulence intensity sensitivity test results of the Standard $k-\varepsilon$ turbulent model with enhanced wall treatment at three different turbulence intensities 2%, 5%, 10%. The figure shows the Standard $k-\varepsilon$ turbulent model with enhanced wall treatment is insensitive to the turbulence intensity in this test study, and thus the Standard $k-\varepsilon$ turbulent model with enhanced wall treatment is adopted to model the turbulent flow in the present study.

5.3.2 Turbulent Evaporation Model Validation

The evaporation model of liquid wall film under a turbulent air stream is validated through comparing the numerical predictions of the velocity profiles and the evaporation mass fractions of evaporating oil film under a turbulent air flows in a rectangular flow channel with that of the experimental results [148, 149]. The geometry parameters and the measurement techniques of the

velocity field and the evaporation mass fractions are the same as described in Section 5.2.2. The turbulence at the inlet of the flow channel is generated and is tuned by mounting a screen mesh with different wire diameters and porosities at the inlet [149].

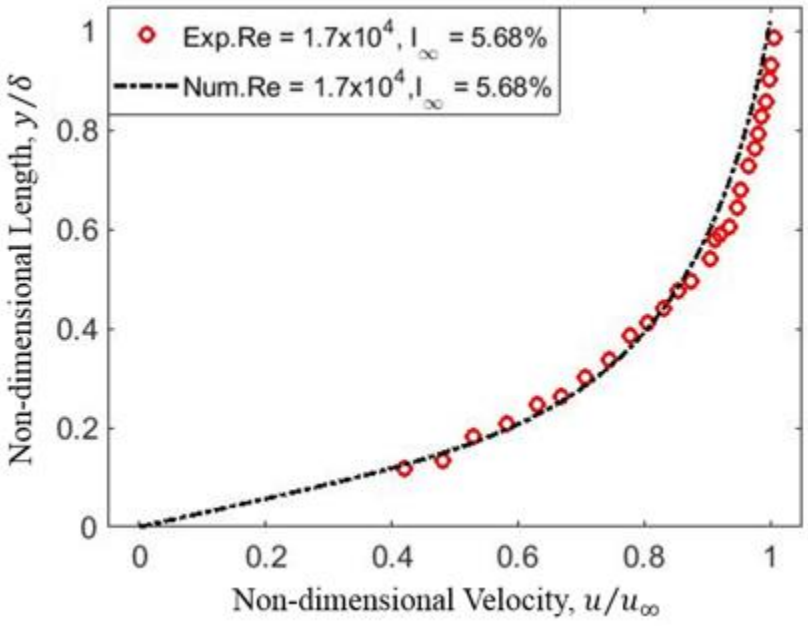

Figure 5.27: Model validation: non-dimensional velocity profiles for the turbulent air flow in a rectangular flow channel at Reynolds number of 1.7×10^4 and turbulence intensity of 5.68%.

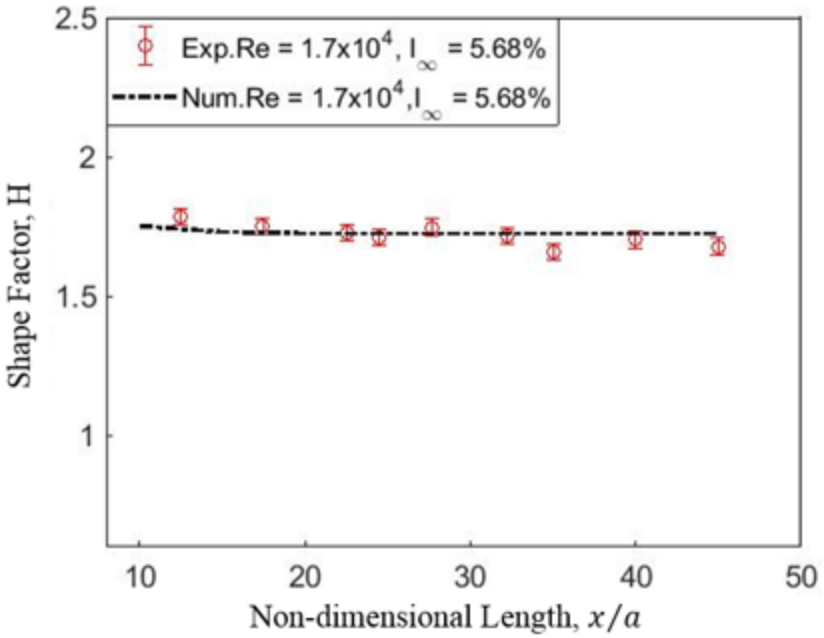

Figure 5.28: Model validation: shape factors along the flow channel for the turbulent air flow in a rectangular flow channel at Reynolds number of 1.7×10^4 and turbulence intensity of 5.68%.

For the validation of the numerical model, the experimental results of non-dimensional velocity profiles and shape factors along the flow channel at Reynolds number of 1.7×10^4 and turbulence intensity of 5.68% are used for the validation of the numerical results of the velocity profiles as displayed in Figure 5.27 and 5.28; As observed, the numerical results of both the non-dimensional velocity profiles and the shape factors along the flow channel can match the experimental results very well; therefore, the turbulent model used in the present study is considered to be accurate for the prediction flow fields of turbulent air stream flowing over the evaporating liquid wall film.

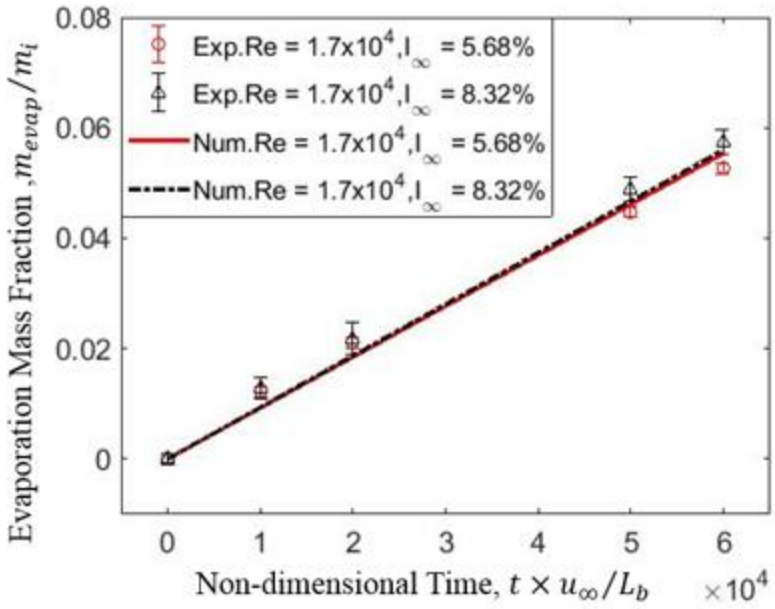

Figure 5.29: Model validation: evaporation mass fraction of oil film under turbulent gas flow conditions at 1.7×10^4 with two different tuebulence intensity at the inlet I_∞ = 5.68% and I_∞ = 8.32%.

Furthermore, the experimental results of evaporation mass fraction of oil film under a turbulent air stream at Reynolds number of 1.7×10^4 and turbulence intensity of 5.68% and 8.32% are employed for the validation of the turbulent evaporation model, and the validation results as presented in Figure 5.29, in which c is the width of the experimental flow channel. It is clear that the numerical predictions and the experiential results match very well for both flow conditions, which indicates that the numerical model is suitable for the prediction of evaporation of liquid wall film under turbulent flow conditions.

5.3.3 Evaporation Characteristics in Turbulent Flow Conditions

After the model validation, the transport phenomena relevant to the evaporating liquid wall film under a high temperature turbulent air stream are studied using the validated evaporation model;

and the results are presented in the Section. The stream lines, velocity fields, isothermals and mass fraction contours at two different evaporating phases are presented followed by the results of the local interfacial velocities, temperatures, mass fractions, and local heat/mass transfer coefficients at different times along the evaporating liquid wall film. Finally, the mass transfer correlation of the evaporating liquid wall film under a turbulent air stream with different turbulence intensities are determined.

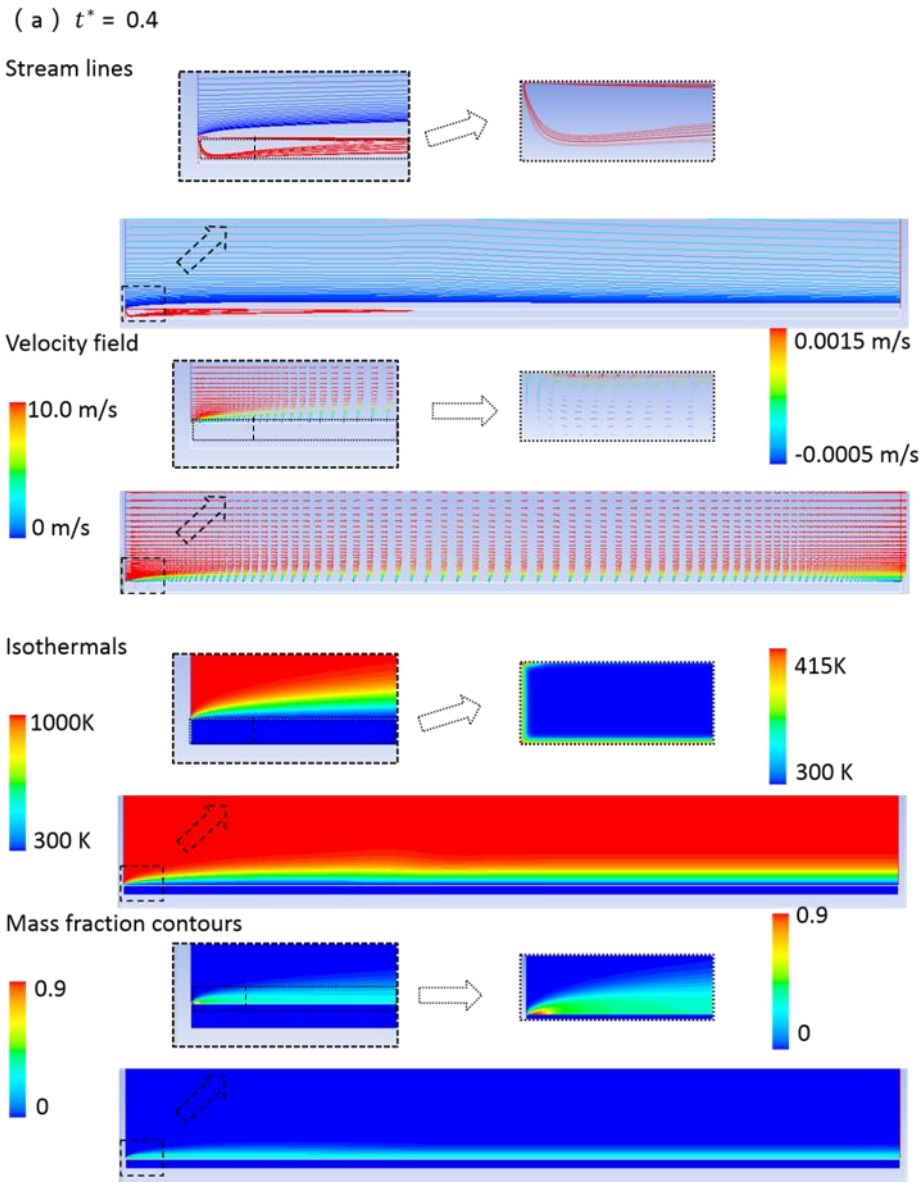

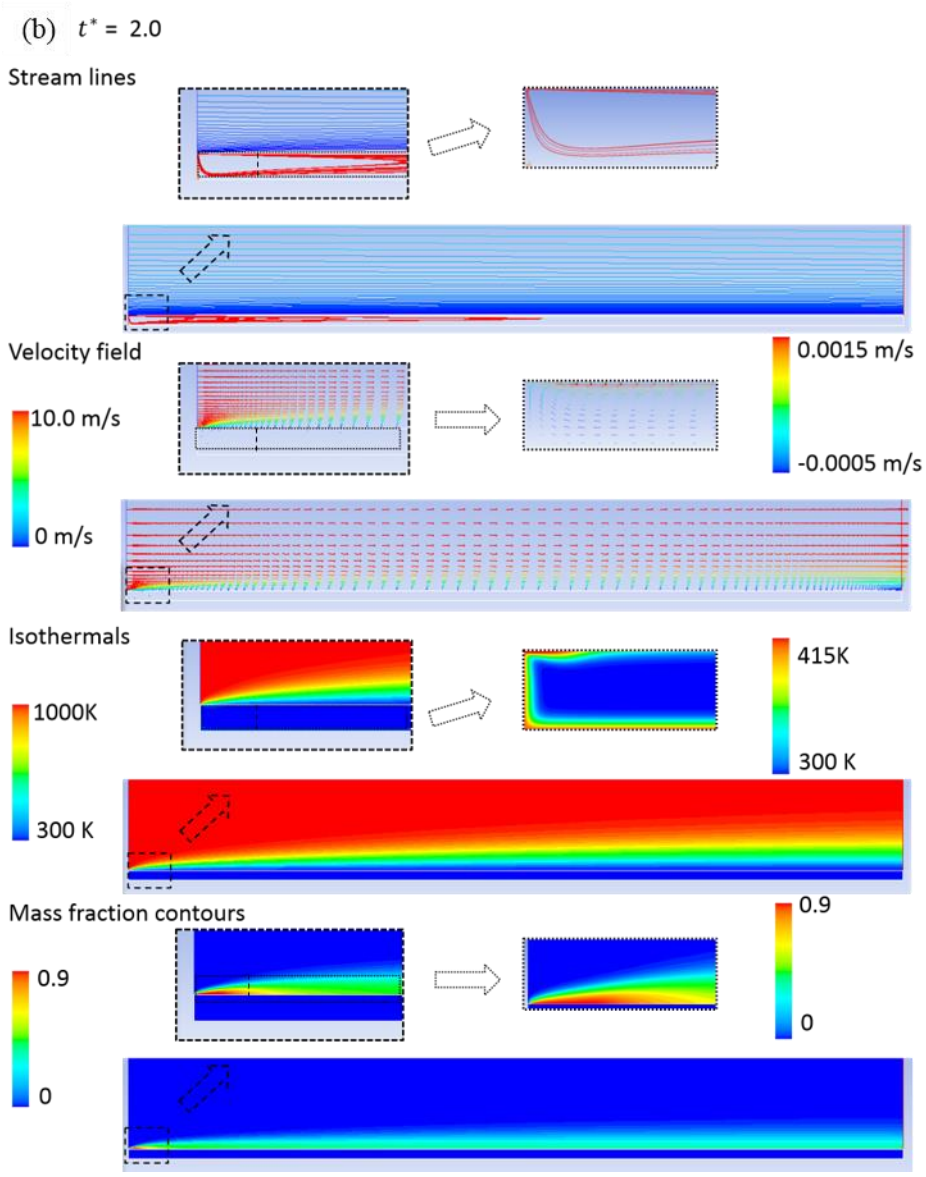

Figure 5.30 Stream lines, flow fields, isothermals and mass fraction contours of the evaporation of liquid wall film in a laminar flow at $\mathrm{Re}_{g,\infty} = 1.7 \times 10^4, T_\infty =$ 1000K and $\mathrm{I}_\infty = 5\%$ at two different evaporation phases at non-dimensional time $t^* = 0.4$ (a) and 2.0 (b) with temperature ranging from 300K to 1000K and vapor mass fraction ranging from 0 to 0.9.

Figure 5.30 shows that a vortex is formed and a velocity boundary layer is developed in the liquid wall film as indicated in the stream lines and flow fields of the liquid phase, which can be attributed to the strong interfacial shear stress caused by the large velocity difference between the liquid wall

film and gas stream. The liquid motion due to the gas/liquid interaction can enhance the liquid heating, which would further boost the evaporation as shown in following sections.

Also, thermal and species boundary layer thickness are increasing along the wall film, especially at the late phase of evaporation ($t^* = 2.0$), which indicates the species gradient and consequently evaporation mass flux is non-uniform, which decreases along the wall film in the stream-wise(x) direction. Moreover, the stable thermal and species boundary layers are built up at the late phase of evaporation process imply that the wall film vaporizes in a quasi-steady state with almost constant evaporation rate at the late phase of the transient evaporation process.

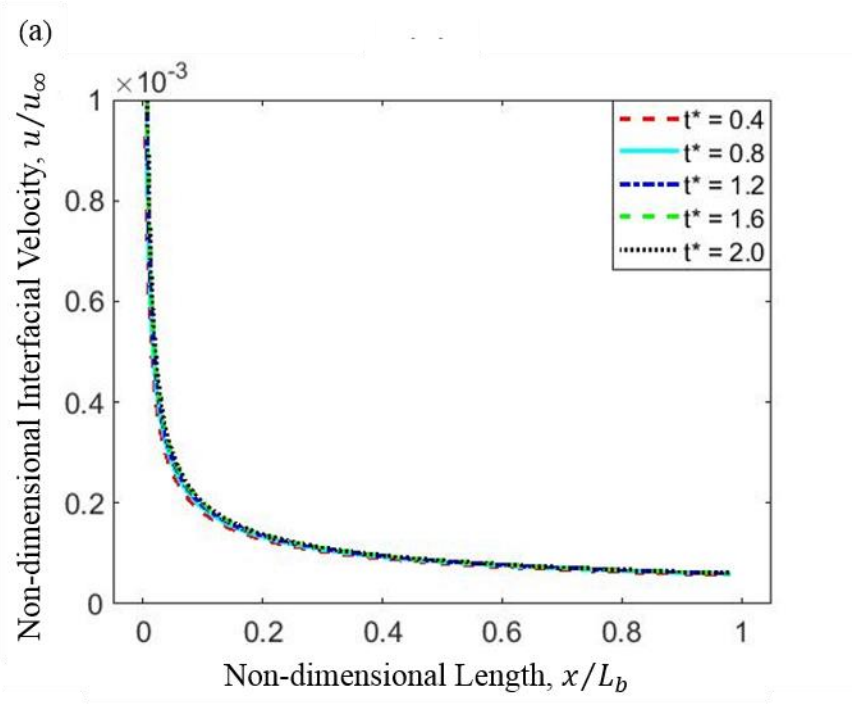

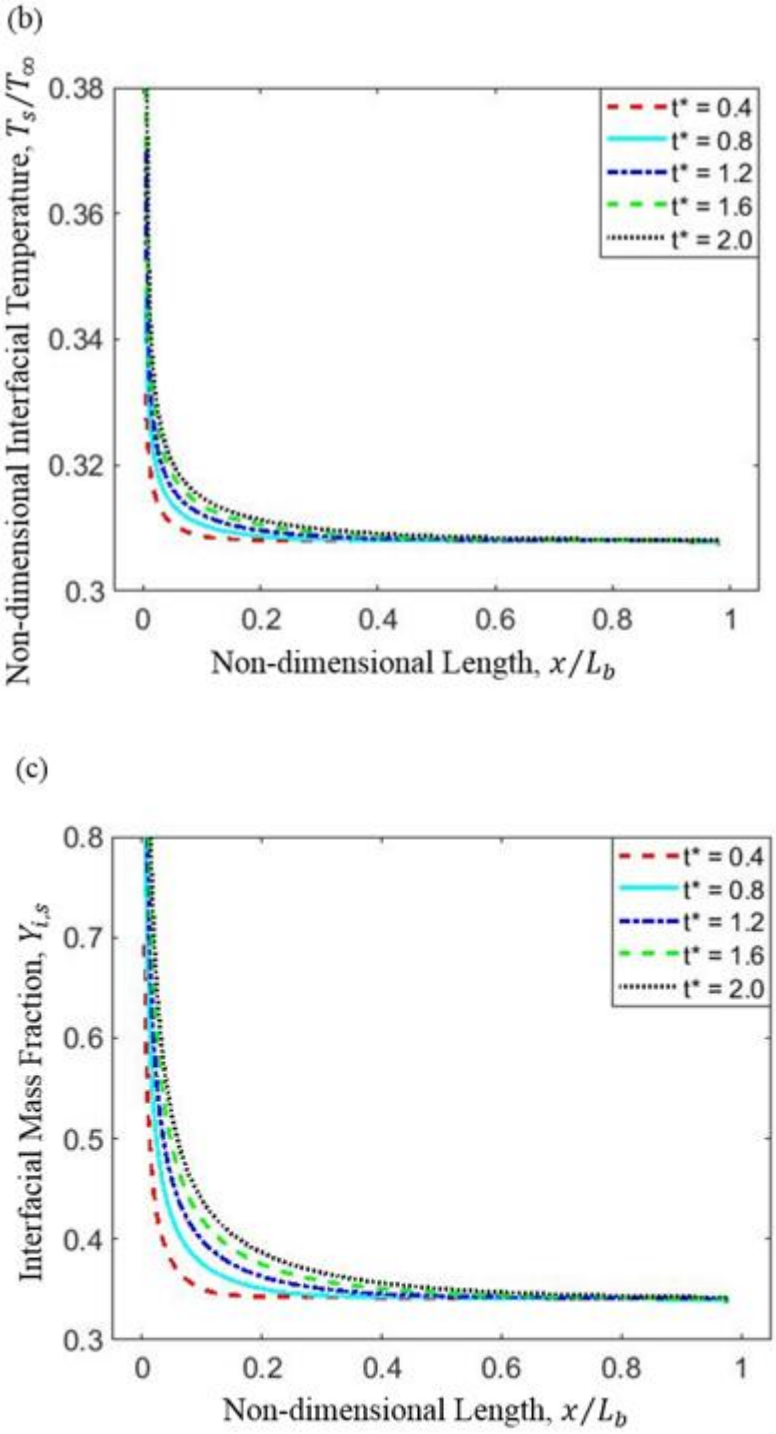

Figure 5.31 Non-dimensional local interfacial velocity profiles in the stream-wise (x) direction (a), temperature (b), and mass fraction (c) histories along the evaporating liquid wall film at five different time $t^* = 0.4, 0.8, 1.2, 1.6$ and2.0.

Figure 5.31 presents the transport phenomena of the evaporating liquid wall film under a turbulent air stream at different time instants. In Figure 5.32 (a), it can be observed that the local interfacial velocities decrease along the evaporating liquid wall film at all five different time instants as indicated in the legend. These results are reasonable, because liquid wall film is accelerated by the shear stress at the gas/liquid interface, which decreases along the evaporating liquid wall film as a result of the growth of velocity boundary layer and the decrease of velocity gradient. It is worthy to mention that the interfacial velocity is around one thousand times smaller than the velocity of the gas stream, which is reasonable due to the large density difference between the liquid wall film and air flows. It can be also seen that the interfacial velocity increases with time, but the increasing magnitude is insignificant. As a strong shear stress can act on the gas/liquid interface as the high speed air flows flowing over the liquid wall film, the liquid wall film start to move and the interfacial velocity at the liquid and gas phase are the same.

Figure 5.31 (b) demonstrates that local interfacial temperatures also decrease along the evaporating liquid wall film similar to the trend of interfacial velocities. The temperature gradients within the thermal boundary layer in the gas stream, as an indicator of the energy transfer rate from the high temperature air stream to the liquid wall film, decline along the evaporating liquid wall film; therefore, the liquid wall film closer to the inlet of the high temperature air stream is heated up more quickly than the rest of the liquid wall film. Moreover, the interfacial temperatures increase with time increases as a results of heat transfer from the gas phase to the liquid wall film, which would further enhance the interfacial vapor mass fraction as shown in Figure 5.32 (c).

Figure 5.31 (c) presents that the local interfacial mass fraction decreases along the evaporating liquid wall film at five different evaporation time points; and the peak value of the mass fraction along the evaporating liquid wall film is close to the leading point of the evaporating liquid wall

film. This is because that at the leading point of the evaporating wall film, the high heat transfer rate would lead to higher evaporation rate, and the increased evaporation rate can consume more energy caused by the enthalpy difference for the phase change of the evaporating liquid wall film, thus the peak values of interfacial mass fraction occurs close to the leading edge of the liquid wall film according to the thermodynamics equilibrium.

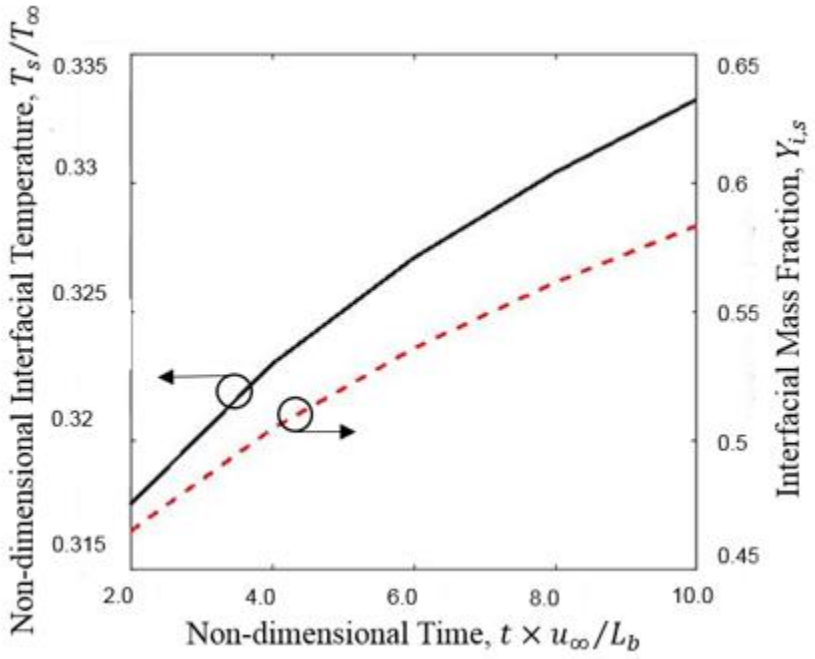

Figure 5.32: Averaged interfacial temperature and vapor mass fraction histories. Black line represents the averaged interfacial temperature whereas red dash line represents averaged interfacial mass fraction.

Figure 5.32 presents that the arithmetic averaged interfacial vapor mass fractions and temperatures over time have a similar trend; and the averaged value of temperatures and mass fractions increase with time increasing. It is can be also found that the increasing extent of mass fraction is much more significant than that of the interfacial temperature. This is reasonable, since the interfacial vapor pressure is an exponent function of local temperature as shown in the Clausius-Clapeyron equation;

and the vapor mass fraction increases slowly when temperature is much lower than the boiling temperature, but it increases very quickly when the temperature of liquid wall film is close to the boiling temperature (at the late phase of evaporation).

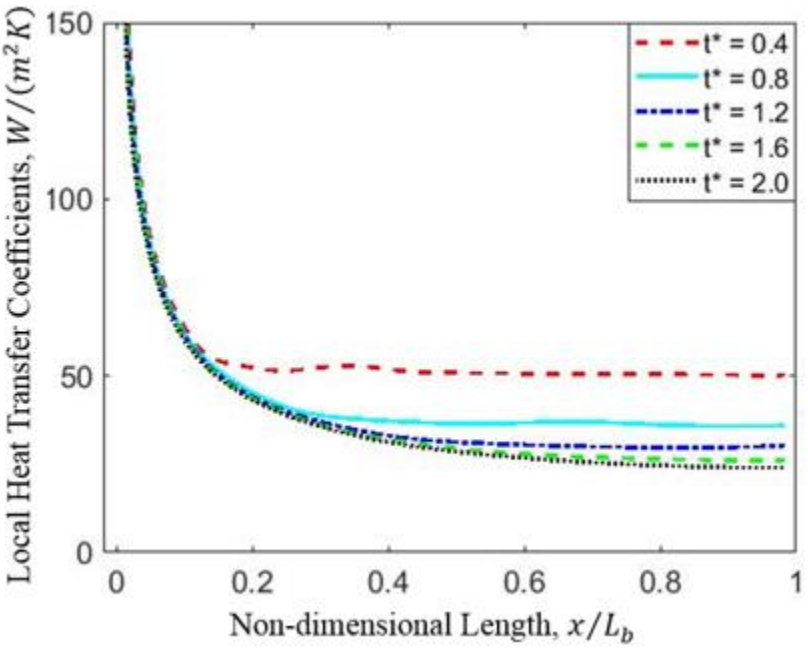

Figure 5.33 Local heat transfer coefficient h_x along the evaporating liquid wall film at five different non-dimensional time $t^* = 0.4, 0.8, 1.2, 1.6$ and2.0.

Figure 5.33 shows that local heat transfer coefficients decreases along the evaporating liquid wall film, which is consistent with the results of isothermal contour in Figure 5.31. Also, as time increases, the heat transfer rate from the gas phase to the liquid increases, which can be attributed to the liquid motion; however, the increasing magnitude is very small due to the inherent self-inhibition of the evaporation process and the growth of thermal boundary layers with time.

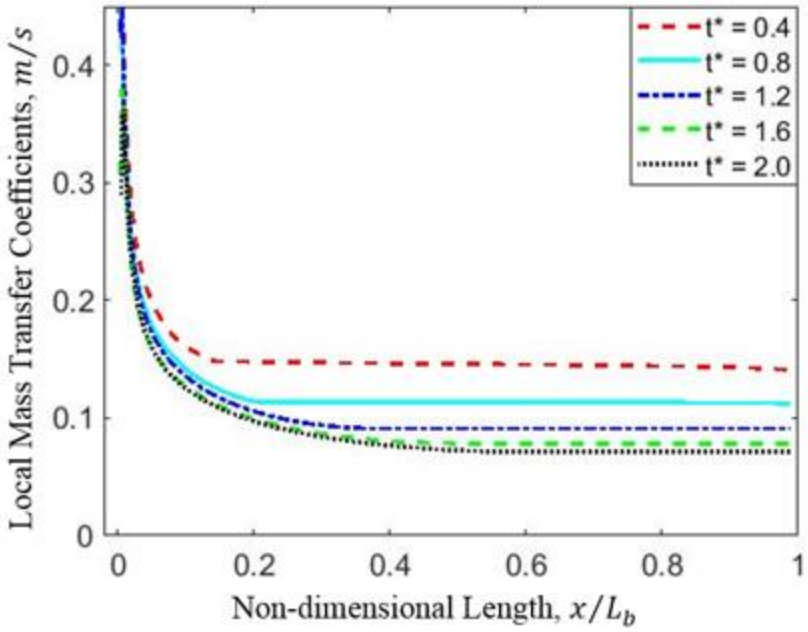

Figure 5.34 Local mass transfer coefficient h_m along the evaporating liquid wall film at five different non-dimensional time $t^* = 0.4, 0.8, 1.2, 1.6$ and2.0.

Figure 5.34 shows that the trend of mass transfer coefficients along the evaporating liquid wall film at different non-dimensional time is similar to that of the heat transfer coefficients, which can be explained by the similarity between heat and mass transfer. It can be also observed that the increasing magnitude of mass transfer coefficient with time increasing is more significant than that of the heat transfer coefficients. This is reasonable, since the interfacial mass fraction increases much more quickly at the late phase of evaporation, and the heating and motion in the liquid phase can also enhance the evaporation process at late phase of the evaporation process.

The evaporation of liquid wall film in turbulent flows at different flow velocities and turbulence intensities at the inlet are considered for the derivation of its mass transfer correlation; and the case numbers of the numerical study with their flow conditions are listed in Table 5.8. The gaseous phase averaged Sherwood number at nine different time instants during the transient evaporation process

of the liquid wall film in turbulent air flows are calculated; and the numerical results are listed in Table E.2.1 and E.2.2.

Table 5.8: Calculated cases and parameters of the evaporation of liquid wall film in turbulent air flows studied in the present study.

Case Number/ #	Reynolds number at the inlet / $\mathrm{Re}_{g,\infty}$	Turbulence Intensities/ I_∞
1	8.5×10^3	5%
2	8.5×10^3	10%
3	8.5×10^3	15%
4	8.5×10^3	20%
5	8.5×10^3	25%
6	1.7×10^4	5%
7	1.7×10^4	10%
8	1.7×10^4	15%
9	1.7×10^4	20%
10	1.7×10^4	25%
11	3.4×10^4	5%
12	3.4×10^4	10%
13	3.4×10^4	15%
14	3.4×10^4	20%
15	3.4×10^4	25%
16	5.1×10^4	5%
17	5.1×10^4	10%

18	5.1×10^4	15%
19	5.1×10^4	20%
20	5.1×10^4	25%
21	6.8×10^4	5%
22	6.8×10^4	10%
23	6.8×10^4	15%
24	6.8×10^4	20%
25	6.8×10^4	25%

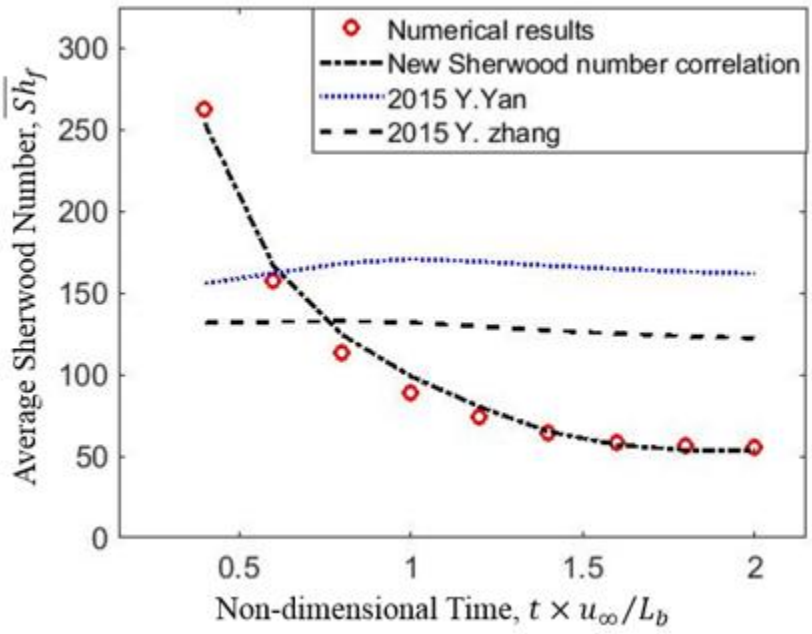

Figure 5.35 Comparison of the averaged Sherwood number history of the evaporation of liquid wall film in turbulent air flow at $\mathrm{Re}_{g,\infty} = 1.7 \times 10^4$, $T_\infty =$ 1000K and $\mathrm{I}_\infty = 5\%$ with existing mass transfer correlations and numerical results at the same flow condition; the new and existing Sherwood number correlations shown in the figure are given in Equation (5.32), (5.33) and (5.34), respectively.

Figure 5.35 compares the history of the averaged mass transfer correlation, $\overline{\mathrm{Sh}_{\mathrm{f}}}$, of the evaporating liquid wall film in turbulent air flow at $\mathrm{Re}_{\mathrm{g},\infty} = 1.7 \times 10^4$, $T_\infty = 1000\mathrm{K}$ and $\mathrm{I}_\infty = 5\%$ calculated using Equation (5.32) with the existing mass transfer correlations and the numerical results at the same flow condition. The newly developed Sherwood number is calculated using the instantaneous values to represent the transient evaporation process of the evaporating liquid wall film; therefore, the new Sherwood number correlation is plotted as a function of time to clearly demonstrate the physical meaning of the comparison. It shows that the Sherwood number correlation shown in the figure,

$$\overline{\mathrm{Sh}_{\mathrm{f}}}[\,\mathrm{B_M}/(1+\,\mathrm{B_M})]^{3.7} = 2.3 + \,0.0018\mathrm{Re}_{\mathrm{g}}^{0.797}\mathrm{Sc}_{\mathrm{g}}^{1/3} \tag{5.32}$$

can match very well (within 5%) with the numerical results of the transient evaporation of liquid wall film. However, existing mass transfer correlations cannot represent the variation of the Sherwood number during the transient evaporation process of the liquid wall film; and the Sherwood number predicted by the existing mass transfer correlations remain almost a constant with time changing. Specifically, the existing mass transfer correlation proposed by Y. Yan (2015), Equation (5.33), and Y. Zhang (2015), Equation (5.34), under-predicts the mass transfer rate by 34.15% and 36.12% respectively at the beginning of the evaporation process, while they over-predicts the evaporation rate by around 171.5% and 134.9% respectively at the non-dimensional time point t^* of 2. These discrepancies are reasonable, since the traditional mass transfer correlations only validated for steady flow conditions; however, the variation of blowing effects, which have significant effects on the evaporation of liquid wall film, are ignored.

$$\overline{\mathrm{Sh}_{\mathrm{f}}} = \,0.0296\mathrm{Re}_{\mathrm{g}}^{0.8}\mathrm{Sc}_{\mathrm{g}}^{1/3} \tag{5.33}$$

$$\overline{\mathrm{Sh}_{\mathrm{f}}} = \,0.0287\mathrm{Re}_{\mathrm{g}}^{0.8}\mathrm{Sc}_{\mathrm{g}}^{0.6} \tag{5.34}$$

The blowing effects along with effects of convection and variable properties are taken into account in Equation (5.32). In addition, the effects of liquid phase heating are included in the newly developed mass transfer correlation through estimating the thermo-physical properties using the reference temperature and concentration; and the mass transfer number B_M, which are directly affected by the liquid phase heating.

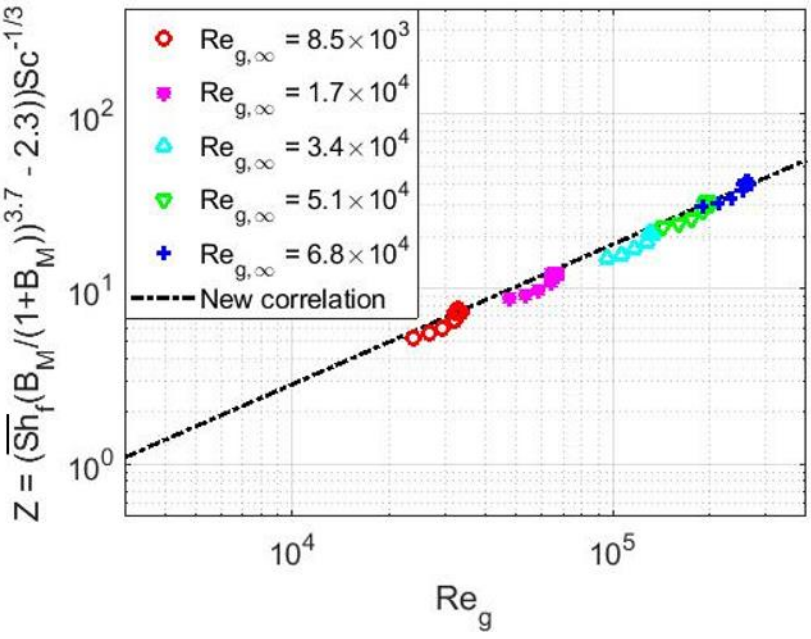

Figure 5.36 Comparison of the new Sherwood number correlation, $\overline{Sh_f}$, of the evaporating liquid wall film in turbulent flows at different Reynolds numbers at the inlet with numerical results; --: $Z = 0.0018Re_g^{0.797}$; symbols: data of numerical results.

Figure 5.36 compares the newly developed averaged Sherwood number correlation of the evaporating liquid wall film in turbulent air flows with numerical results at the same flow conditions. It can be seen that the newly developed correlation can match the numerical results very well for all the non-dimensional time instants and Reynolds numbers investigated in this study. For a certain flow condition (Reynolds number at the inlet), the averaged mass transfer number in

the gas phase varies with time changing, which can be attributed to the non-linear variation of thermos-physical properties during the evaporation process.

As demonstrated in the experimental study, the turbulence intensities do not have significant effects on the evaporation of oil wall film in turbulent gas flows with different turbulence intensities, since the evaporation mass flux is directly determined by the concentration gradients in the region close to the gas/liquid interface, which remain almost the same within the viscous sub-layer for the turbulent flows with different turbulence intensities [149]. Therefore, the newly developed correlation for the evaporation of liquid wall film in turbulent flows can be extend to simulate the evaporation of liquid wall film in turbulent flows with different turbulence intensities.

5.4 Summary

In this Chapter, numerical study on the evaporation of liquid wall film in engine-like conditions are performed; and the results of evaporating liquid wall film under different boundary conditions 1) in a stationary gas medium, 2) in laminar air streams, and 3) in turbulent air streams are presented. Also, the mass transfer correlations corresponding to different flow conditions are determined.

An analytical model with its pertinent boundary conditions for the evaporation of liquid wall film in a stationary gas medium with three different evaporation boundary conditions have been developed and solved. The results show that for the evaporation of liquid wall film in an infinite and finite space, the evaporation rate, characterized by the Sherwood number, drops quickly in the early stage of the evaporation process due to the large vapor concentration gradient between the gas/liquid interface with the gas medium. Moreover, the evaporation rates approach to a constant with time increasing. Furthermore, for the same evaporation conditions, the evaporation of liquid

wall film in an infinite space can achieve the highest evaporation rate, while evaporation rate of liquid wall film with oscillating boundary conditions is the lowest because of the diminishment of effective evaporation time. Finally, for the evaporation of liquid wall film in a stationary gas medium with oscillating boundary conditions, both oscillating frequency and amplitude of the interfacial temperature have significant effects on its evaporation process, and increasing the oscillating frequency or amplitude can enhance the evaporation process.

Numerical study has been performed to investigate the transient evaporation process of liquid wall film under laminar flow conditions; and a mass transfer correlation representing the transient evaporation of liquid wall film in laminar flow conditions are determined. The numerical model is validated through comparing the numerical results of velocity profiles and evaporation mass rates with experimental results of evaporation of oil film at room temperature. It is found that the evaporation rate characterized by mass transfer coefficient is non-uniform along the wall film, which is consistent with the development of species boundary layer and decreasing of concentration gradient within the boundary layer. A mass transfer correlation,

$$\overline{\mathrm{Sh}_\mathrm{f}}[\,\mathrm{B_M}/(1+\,\mathrm{B_M})]^{3.7} = 1.0 + \,0.0155\mathrm{Re}_\mathrm{g}^{0.534}\mathrm{Sc}_\mathrm{g}^{\frac{1}{3}}$$

is developed, which can increase the accuracy of modeling the transient evaporation of liquid wall film under laminar flow conditions compared with the traditional mass transfer correlations.

Finally, the evaporation of liquid wall film under a turbulent air stream is studied using the numerical evaporation model. Turbulence models with different near wall modeling methods are evaluated to identify the suitable turbulence model for the modeling of evaporation of liquid wall film in turbulent flow conditions. And the results show that the Standard $k-\varepsilon$ turbulent model with enhanced wall treatment is recommended for the modeling of evaporation problem in

turbulent flow conditions. The results also show that the transient evaporation rate of liquid wall film is mainly determined by the gas/liquid interfacial temperature, which is directly affected by the liquid heating process; while the effects of turbulence intensity on the evaporation of liquid wall film is insignificant. Finally, the correlation,

$$\overline{\mathrm{Sh}_\mathrm{f}}[\,\mathrm{B_M}/(1+\,\mathrm{B_M})]^{3.7} = 2.3 + \,0.0018\mathrm{Re}_\mathrm{g}^{0.797}\mathrm{Sc}_\mathrm{g}^{1/3}$$

is able to represent the transient evaporation process of liquid wall film under turbulent flow conditions very well; and the accuracy of the mass transfer correlation can be significantly improved compared with the traditional mass transfer correlation without considering of the transient effects.

Chapter 6
Conclusions and Future Work

In this thesis research, the transient evaporation characteristics of liquid wall film in DISI engine-like conditions are investigated; and their mass transfer correlations are determined. Three different evaporation boundary conditions (in a stationary gas medium, in laminar flow conditions and in turbulent flow conditions) are considered for the complete understanding of the evaporation of liquid wall film in DISI engine-like conditions.

An analytical model with its pertinent boundary conditions for the evaporation of liquid wall film in a stationary gas medium has been developed and solved to provide benchmark data for the verification of the species transport process in the numerical evaporation model. In addition, numerical studies on the evaporation of liquid wall film in a high temperature convective environment are also performed for the characterization of their transient evaporation process and the determination of their mass transfer correlations. Important physics involved in the evaporation of liquid wall film such as 1) the transient heating and motion of the liquid phase, 2) thermo-physical properties variations with the boundary layers, and 3) strong coupling among the momentum, heat and mass transfer, are included in the numerical models. The numerical results have been validated against analytical and experimental data; and very good agreement is achieved. These numerical studies provide an effective method to study the transient evaporation process of liquid wall film in DISI engine-like flow conditions. Moreover, more accurate mass transfer correlations that can represent the transient evaporation of liquid wall film in DISI engine-like conditions are developed based on the numerical study.

6.1 Conclusions of the Present Study

In summary, key conclusions can be drawn from this thesis research:

- the evaporation rate of liquid wall film, characterized by the Sherwood number, in a stationary gas medium without oscillating interfacial vapor mass fractions is largely dependent on the gradients of vapor species concentrations at the gas/liquid interface, which drops quickly at the early stage of the evaporation process and approaches to a constant with an increase in the evaporation time;
- for the evaporation of liquid wall film in a stationary gas medium with oscillating boundary conditions, both the oscillating frequency and amplitude can affect the evaporation process significantly, and increasing the oscillating frequency or amplitude can enhance the evaporation rate;
- a non-uniform evaporation mass flux along the evaporating wall film in a high temperature convective environment is observed, and the transient evaporation of liquid wall film in a high temperature gas medium is mainly determined by the gas/liquid interfacial temperature;
- the transient evaporation process of liquid wall film in laminar flow conditions can be characterized by the newly developed mass transfer correlation,

$$\overline{\mathrm{Sh}_\mathrm{f}}[\,\mathrm{B_M}/(1+\,\mathrm{B_M})]^{3.7} = 1 + \,0.0155\mathrm{Re}_\mathrm{g}^{0.534}\mathrm{Sc}_\mathrm{g}^{1/3},$$

  which can significantly increase the accuracy of the existing mass transfer correlation;

- the standard $k-\,\varepsilon$ model with enhanced wall treatment can provide accurate results for the turbulent gas flows adjacent to the gas/liquid interface in the typical range of turbulence

intensities in DISI engines; and this model is considered to be a suitable model for the numerical study of the evaporation in turbulent flow conditions;

- the newly developed correlation:

$$\overline{Sh_f}[\,B_M/(1+\,B_M)]^{3.7} = 2.3 + \,0.0018Re_g^{0.797}Sc_g^{1/3},$$

is able to represent the transient evaporation process of liquid wall film in turbulent flow conditions; and the accuracy of the mass transfer correlation is much better than the traditional mass transfer correlations.

6.2 Recommendations for Future Work

Based on the results of the present thesis study, some research areas are highlighted for the future study summarized as follows:

- study on the evaporation of liquid wall film in engines with the effects of intake and exhaust valve motion can be performed with more powerful computing facilities;
- the evaporation of liquid wall film at different engine operating conditions can be investigated and correlations between the evaporating liquid wall film and the engine-out PM emissions can be developed;
- the effects of waves formed on the gas/liquid interface caused by the strong gas/liquid interaction on the evaporation of liquid wall film still needs more work;
- the evaporation of liquid wall film under high temperature flows from vertical direction can also be studied to examine the effects of flow directions on its evaporation process;
- the underlying transport characteristics of multi-component evaporating liquid wall film still need investigation, and the mass transfer correlations of multi-component liquid wall film can be also developed.

References

[1] F. Zhao, M.-C. Lai and D.L. Harrington. Automotive spark-ignited direct- injection gasoline engines, Progress in Energy and Combustion Science. 25: 437–562, 1999.

[2] Y. Takagi, T. Itoh, S. Muranaka, A. Iiyama, Y. Iwakiri, T.Urushihara and K. Naitoh. Simultaneous attainment of low fuel consumption high output power and low exhaust emissions in direct injection SI engines, SAE Technical Paper, 980149, 1998.

[3] H. Cho, M. Kim, and K. Min. The Effect of Liquid Fuel on the Cylinder Liner on Engine-Out Hydrocarbon Emissions in SI Engines, SAE Technical Paper 2001-01-3489, 2001.

[4] R. Stanglmaier, J. Li, and R. Matthews. The Effect of In-Cylinder Wall Wetting Location on the HC Emissions from SI Engines, SAE Technical Paper 1999-01-0502, 1999.

[5] J. Li, R. D. Matthews, R. Stanglmaier, C. Roberts, R. Anderson. Further Experiments on the Effects of In-Cylinder Wall Wetting on HC Emissions from Direct Injection Gasoline engines, SAE Technical Paper, 1999-01-3661, 1999.

[6] K. H. Choi, J. H. Park, N. H. Lee, C. H. Yu, S. H. Noh. A research on fuel spray and air flow fields for spark-ignited direct injection using laser measurement technology, SAE Technical Paper, 1999-01-0503, 1999.

[7] S. Matsushita, T. Inoue, K. Nakanishi, K. Kato, N. Kobayashi. Development of the TOYOTA lean combustion system. SAE Technical Paper, 850044, 1985.

[8] M. M. Maricq, D. H. Podsiadlik, D. D. Brehob and M. Haghgooie. Particulate emissions from a Direct-Injection Spark-Ignition (DISI) engine, SAE Technical paper, 1999-01-1530, 1999.

[9] D. B. Kittelson, Engines and nanoparticles: a review. Journal of Aerosol Science, 29(5-6): 575-588, 1998.

[10] C. L. Myung, S. Park. Exhaust nanoparticle emissions from internal combustion engines: a review. International Journal of Automotive Technology, 13(1): 9-22, 2012.

[11] E. Stevens and R. Steeper, Piston wetting in an optical DISI engine: fuel Films, pool fires and soot generation, SAE Technical Paper 2001-0101203, 2001.

[12] C. Drake, T. D. Fansler, A. S. Solomon and G. A. Szekely. Piston fuel films as a source of smoke and hydrocarbon emissions from a wall-controlled spark-ignited direct-injection engine, SAE Technical Paper, 2003-01-0547, 2003.

[13] M. Braisher, R. Stone, and P. Price. Particle number emissions from a range of European vehicles. SAE Technical Paper 2010-01-0786, 2010.

[14] B. Graskow, D. Kittelson, M. Ahmadi, and J. Morris. Exhaust particulate emissions from a direct injection spark ignition engine. SAE Technical Paper 1999-01-1145, 1999.

[15] P. Penttinen, K. Timonen, P. Tiittanen, A. Mirme, J. Ruuskanen, and J. Pekkanen. Ultrafine particles in urban air and respiratory health among adult asthmatics. European Respiratory Journal, 17(3): 428–435, 2001.

[16] I. A. Khalek, T. Bougher, J. J. Jetter. Particle Emissions from a 2009 Gasoline direct injection engine using different commercially available fuels, SAE Technical Paper. 2010-01-2117, 2010.

[17] D. Sabathil, A. Koenigstein, P. Schaffner, J. Fritzsche and A. Doehler. The Influence of DISI Engine Operating Parameters on Particle Number Emissions, SAE Technical Paper, 2011-01-0143, 2011.

[18] Z. Han, J. Yi and N. Trigui. Stratified Mixture Formation and Piston Surface Wetting in a DISI Engine, SAE Technical Paper, 2002-01-2655, 2002.

[19] J. Yi, Z. Han, and N. Trigui. Fuel-air mixing homogeneity and performance improvements of a stratified-charge DISI combustion system, SAE Technical Paper, 2002-01-2656, 2002.

[20] C. Bai, A.D. Gosman. Mathematical modeling of wall Films formed by impinging sprays, SAE Technical Paper, 960626, 1996.

[21] H. Foucarth, C. Hanchi, J. F. Le Coz, and T. Baritaud. Development of a three dimensional model of wall fuel liquid film for internal combustion engines, SAE Technical Paper, 980133, 1998.

[22] P. O'Rourke, A. Amsden. A particle numerical model for wall fluid dynamics in port injected engines, SAE Technical Paper, 961961, 1996.

[23] P. O'Rourke, A. Amsden. A spray/wall interaction submodel for the KIVA-3 wall film model, SAE Technical Paper, 2000-01-0271, 2000.

[24] Z. Han, Z. Xu .Wall film dynamics modeling for impinging sprays in engines, SAE Technical Paper, 2004-01-0099, 2004.

[25] G. D. Mcbain, H. Suerhrcke and J. A. Harris. Evaporation from an open cylinder, International Journal of Heat and Mass Transfer, 43(12): 2117-2128, 2000.

[26] J. W. Rose. Approximate equation for forced convection condensation in the presence of a non-condensing gas on a flat plate and horizontal tube. International Journal of Heat and Mass Transfer, 23(4): 539-546, 1980.

[27] D. W. Staton, C. J. Rutland. Multi-dimensional modeling of thin liquid films and spray-wall interactions resulting from impinging sprays, International Journal of Heat and Mass Transfer, 41(20): 3037-3054, 1998.

[28] S. Witting, J. Himmelsbach, B. Noll, H. J. Feld, W. Samenfink. Motion and evaporation of shear-driven liquid films in turbulent gases, Journal of Engineering for Gas Turbines and Power, 114(2), pp.395-400, 1992.

[29] G. Desoutter, C. Habchi, B. Cuenot, T. Poinsot. DNS and modeling of the turbulent boundary layer over an evaporating liquid film, International Journal of Heat and Mass Transfer, 52(25-26): 6028-6041, 2009.

[30] G. Desoutter, C. Habchi, B. Cuenot, T. Poinsot. Single-component liquid film evaporation model development and validation using direct numerical simulation, ICLASS06-079, ICLASS-2006, Kyoto, Japan. 2006.

[31] D. J. Torres, P. O'Rourke, and A. Amsden, Efficient multicomponent fuel algorithm, Combustion Theory and Modelling, 7(1): 66-86, 2006.

[32] Y. Zeng, C. F. Lee. A multicomponent-fuel film-vaporization model for multidimensional computations, Journal of Propulsion Power, 16(6): 964-973, 2000.

[33] L. Song, W. Zhang, T. Zhang, Z. Qin. A new approach to transient evaporating film heating modeling based on analytical temperature profiles for internal combustion engines, International Journal of Heat and Mass Transfer, 81: 465-469, 2015.

[34] Y. Yan, H. Liu, M. Jia, M. Xie, H. Yin. A one-dimensional unsteady wall film evaporation model, International Journal of Heat and Mass Transfer, 88: 138-148, 2015.

[35] O. G. Sutton. Wind structure and evaporation in a turbulent atmosphere, Proceedings of the Royal Society A, Mathematical, Physical and Engineering Science, 146(858):701-722, 1934.

[36] D. Mackay, R. S. Matsugu. Evaporation rates of liquid hydrocarbon spills on land and water, The Canadian Journal of Chemical Engineering, 51: 434-439, 1973.

[37] W. C. Yang, H. Wang. Modeling of oil evaporation in aqueous environment, Water Research, 11: 879-887, 1977.

[38] M. F. Fingas. The evaporation of oil spills: prediction of equations using distillation data, Spill Science and Technology Bulletin, 3(4): 191-192, 1997.

[39] M. F, Fingas. Studies on the evaporation of crude oil and pertroleum products: I. the relationship between evaporation rate and time, Journal of Hazardous Materials, 56: 227-236, 1997.

[40] K. Okamoto, N. Watanabe, Y. Hagimoto, K. Miwa, H. Ohtani. Evaporation characteristics of multi-component liquid, Journal of Loss Prevention in the Process Industry, 23: 89-97, 2010.

[41] J. E. Welch, F. H. Harlow, J. P. Shannon, B. J. Daly, The MAC method: a computing technique for solving viscous, incompressible, transient fluid-flow problems involving free surfaces, LASL Rep. LA-3425, Los Alamos, New Mexico, 1965.

[42] J. E. Welch, F. H. Harlow, J. P. Shannon, B. J. Daly, The MAC method: a computing technique for solving viscous, incompressible, transient fluid-flow problems involving free surfaces, LASL Rep. LA-3425, Los Alamos, New Mexico, 1965.

[43] D. Juric, G. Tryggvason. A front-tracking method for dendritic solidification. Journal of. Computational Physics. 123(1): 127-148, 1996.

[44] W. F. Noh, P. Woodward. SLIC (simple line interface method), International Conference on Numerical Methods om Fluid Dynamics, 5th, Technische Hogeschool Twente, Enschede, Netherlans, 330-340, 1976.

[45] C. W. Hirt, B. D. Nichols, Volume of fluid (VOF) method for the dynamics of free boundaries, J, Journal of Computational Physics. 39: 201–225, 1981.

[46] D. Gueyffier, J. Li, A. Nadim, R. Scardovelli, S. Zaleski. Volume-Of-Fluid interface tracking with smoother surface stress methods for three-dimensional flows, Journal of Computational Physics. 152: 423–456, 1999.

[47] W. J. Rider, D. B. Kothe, Reconstructing volume tracking, Journal of Computational Physics. 141: 112–152, 1998.

[48] M. Sussman, P. Smerka, S. Osher. A level set approach for computing solutions to incompressible two-phase flow, Journal of Computational Physics. 114(1): 146-159, 1994.

[49] G. B. Liu, K. T. Yu, X. G. Yuan, C. J. Liu, A numerical method for predicting the performance of a randomly packed distillation column, International Journal of Heat and Mass Transfer 52(23-24): 5330–5338, 2009.

[50] L. Raynal, C. Boyer, J. P. Ballaguet, Liquid holdup and pressure drop determination in structured packing with CFD simulations, The Canadian Journal of Chemical Engineering, 82: 871–879, 2004.

[51] M. Klöker, E. Y. Kenig, A. Górak, On the development of new column internals for reactive separations via integration of CFD and process simulation, Catalysis. Today, 79–80: 479–485, 2003.

[52] Y. Egorov, F. Menter, M. Klöker, E. Y. Kenig, On the combination of CFD and rate based modelling in the simulation of reactive separation processes, Chemical Engineering and Processing: Process Intensification, 44(6): 631–644, 2005.

[53] Y. Yuan, M. Han, Y. Cheng, D. Wang, Y. Jin. Experimental and CFD analysis of two-phase cross/countercurrent flow in packed column with a novel internal, Chemical Engineering Science. 60(22): 6210–6216, 2005.

[54] I. Iliuta, B. P. A. Grandjean, S. Piché, F. Larachi, Two-fluid model for countercurrent dumped packing-containing columns, Chemical Engineering Science, 58(7): 1373–1380, 2003.

[55] I. Iliuta, C. F. Petre, F. Larachi, Hydrodynamic continuum model for two-phase flow structured-packing-containing columns, Chemical Engineering Science, 59(4): 879– 888.

[56] F. H. Yin, C. G. Sun, A. Afacan, K. Nandakumar, K. T. Chuang, CFD modeling of mass transfer processes in randomly packed distillation columns, Industrial and Engineering Chemistry Research. 39(5): 1369–1380.

[57] M. H. Fard, M. Zivdar, R. Rahimi, M. N. Esfahany, A. Afacan, K. Nandakumar, K. T. Chuang, CFD simulation of mass transfer efficiency and pressure drop in a structured packed distillation column, Chemical Engineering Technology. 30 (7): 854–861, 2007.

[58] M. R. K. Nikou, M. R. Ehsani, M. D. Emami, CFD simulation of hydrodynamics, heat and mass transfer simultaneously in structured packing, International Journal of Chemical Reactor Engineering. 6: A91, 2008.

[59] B. Szulczewska, I. Zbicinski, A. Górak, Liquid flow on structured packing: CFD simulation and experimental study, Chemical Engineering and Technology. 26 (5): 580– 584, 2003.

[60] F. Gu, C. J. Liu, X. G. Yuan, G. C. Yu. CFD simulation of liquid film flow on inclined plates, Chemical Engineering and Technology, 27(30): 1099–1104, 2004.

[61] P. Valluri, O. K. Matar, G. F. Hewitt, M. A. Mendes. Thin film flow over structure packing at moderate Reynolds numbers, Chemical Engineering Science. 60 (7): 1965– 1975, 2005.

[62] A. Hoffmann, I. Ausner, J. U. Repke, G. Wozny. Fluid dynamics in multiphase distillation processes in packed towers, Computers and Chemical Engineering, 29 (6) 1433 – 1437, 2005.

[63] Y. Xu, S. Paschke, J. U. Repke, J. Yuan, G. Wozny. Portraying the countercurrent flow on structured packing by three-dimensional computational fluid dynamics simulations, Chemical Engineering and Technology, 31(10): 1445–1452, 2008.

[64] A. Ataki, H. J. Bart. Experimental and CFD simulation study for the wetting of a structured packing element with liquids, Chemical Engineering and Technology, 29 (3): 336–347, 2006.

[65] S. J. Luo, W. Y. Fei, X. Y. Song, H. Z. Li. Effect of channel opening angle on the performance of structured packing, Chemical Engineering Journal, 144 (2): 227–234, 2008.

[66] J. Chen, C. Liu, X. Yuan, G. Yu, CFD simulation of flow and mass transfer in structured packing distillation columns, Chinese Journal of Chemical Engineering, 17 (3): 381– 388, 2009.

[67] Y. Haroun, D. Legendre, L. Raynal, Direct numerical simulation of reactive absorption in gas–liquid flow on structured packing using interface capturing method, Chemical Engineering Science, 65(1): 351-356, 2010.

[68] D. Juric, G. Tryggvason. Computations of boiling flows, International Journal of Multiphase Flow, 24 (3): 387–410, 1998.

[69] F. Gibou, L. Chen, D. Nguyen, S. Banerjee. A level set based sharp interface method for the multiphase incompressible Navier–Stokes equations with phase change, Journal of Computational Physics, 222 (2): 536–555, 2007.

[70] S. Tanguy, T. Ménard, A. Berlemont. A level set method for vaporizing two phase flows, Journal of Computational Physics, 221 (2): 837–853, 2007.

[71] X. Y. Luo, M. J. Ni, A. Ying, M. A. Abdou. Numerical modeling for multiphase incompressible flow with phase change, Numerical Heat Transfer, Part B, 48: 425–444, 2005.

[72] G. Son, V. K. Dhir, Numerical simulation of film boiling near critical pressures with a level set method, Journal of Heat Transfer, 120 (1): 183–192, 1998.

[73] C. Yang, Z. S. Mao, Numerical simulation of interphase mass transfer with the level set approach, Chemical Engineering Science, 60 (10): 2643–2660, 2005.

[74] J. Wang, P. Lu, Z. Wang, C. Yang, Z. S. Mao, Numerical simulation of unsteady mass transfer by the level set method, Chemical Engineering Science. 63(2): 3141–3151, 2008.

[75] S. W. J. Welch, J. Wilson, A volume of fluid based method for fluid flows with phase change, Journal of Computational Physics, 160(2): 662–682, 2000.

[76] M. G. Wohak, H. Beer, Numerical simulation of direct-contact evaporation of a drop rising in a hot, less volatile immiscible liquid of higher density – possibilities and limits of the SOLA-VOF/CSF algorithm, Numerical Heat Transfer, Part A, 33(6): 561–582, 1998.

[77] M. R. Davidson, M. Rudman, Volume-Of-Fluid calculation of heat and mass transfer across deforming interfaces in two-fluid flow, Numerical Heat Transfer, Part B, 41: 291–308, 2002.

[78] D. J. E Harvie, D. F. Fletcher. A hydrodynamic and thermodynamic simulation of droplet impacts on hot surfaces, Part I: theoretical model, International Journal of Heat and Mass Transfer, 44 (14): 2633–2642, 2001.

[79] D. J. E Harvie, D. F. Fletcher. A hydrodynamic and thermodynamic simulation of droplet impacts on hot surfaces, Part II: validation and applications, International Journal of Heat and Mass Transfer, 44 (14): 2643–2659, 2001.

[80] N. Nikolopoulos, A. Theodorakakos, G. Bergeles, A numerical investigation of the evaporation process of a liquid droplet impinging onto a hot substrate, International Journal of Heat and Mass Transfer, 50(1-2): 303–319, 2007.

[81] G. Strotos, M. Gavaises, A. Theodorakakos, G. Bergeles, Numerical investigation on the evaporation of droplets depositing on heated surfaces at low Weber numbers, International Journal of Heat and Mass Transfer, 51 (7-8): 1516–1529, 2008.

[82] R. Banerjee, A numerical study of combined heat and mass transfer in an inclined channel using the VOF multiphase model, Numerical Heat Transfer, Part A, 52: 163–183, 2007.

[83] R. Banerjee, K. M. Isaac, A study to determine vapor generation from the surface of gasoline flowing in an inclined channel using a continuous thermodynamics approach, Numerical Heat Transfer, Part A, 50: 705–729, 2006.

[84] R. Banerjee, Turbulent conjugate heat and mass transfer from the surface of a binary mixture of ethanol/iso-octane in a countercurrent stratified two-phase flow system International Journal of Heat and Mass Transfer, 51(25-26): 5874–5958, 2008.

[85] J. Schlottke, B. Weigand, Direct numerical simulation of evaporating droplets, Journal of Computational Physics, 227(10): 5215–5237, 2008.

[86] P. Nithiarasu. An arbitrary Lagrangian Eulerian (ALE) formulation for free surface flows using the characteristic-based split (CBS) scheme, International Journal of Numerical Methods in Fluids, 48: 1415–1428, 2005.

[87] J. Li, M. Hesse, J. Ziegler, A. W. Woods. An arbitrary Lagrangian Eulerian method for moving-boundary problems and its application to jumping over water, Journal of Computational Physics, 208: 289–314, 2005.

[88] W. Dettmer, D. Peric. A computational framework for free surface fluid flows accounting for surface tension, Computer Method in Applied Mechanics and Engineering, 195: 3038–3071, 2006.

[89] D. Lakehal, M. Meier, M. Fulgosi, Interface tracking towards the direct simulation of heat and mass transfer in multiphase flows, International Journal of Heat and Fluid Flow, 23: 242–257, 2002.

[90] D. Lörstad, M. Francois, W. Shyy, L. Fuchs, Assessment of volume of fluid and immersed boundary methods for droplet computations, International Journal of Numerical Methods in Fluids 46: 109 –125, 2004.

[91] R. Scardovelli, S. Zaleski, Direct numerical simulation of free-surface and interfacial flow, Annual Reviews of Fluid Mechanics, 31: 567–603, 1999.

[92] R. Scardovelli, S. Zaleski, Direct numerical simulation of free-surface and interfacial flow, Annual Reviews of Fluid Mechanics, 31: 567–603, 1999.

[93] M. Rudman. Volume-tracking methods for interfacial flow calculations, International Journal for Numerical Methods in Fluids, 24: 671–691, 1997.

[94] D. M. Anderson, G. B. McFadden, A. A. Wheeler, Diffuse-interface methods in fluid mechanics, Annual Review of Fluid Mechanics, 30: 139–165, 1998.

[95] S. Osher, R. P. Fedkiw, Level set methods: an overview and some recent results, Journal of Computational Physics, 169: 463–502, 2001.

[96] R. Banerjee, K. M. Isaac. An algorithm to determine the mass transfer rate from a pure liquid surface using the volume of fluid multiphase model, International Journal of Engine Research, 5(1): 23-37, 2003.

[97] J. M. Smith, H. C. Van Ness, M. M. Abbott, Introduction to chemical engineering thermodynamics, sixth ed., McGraw-Hill, New York, 2011.

[98] J. B. Haelssig, J. Thibault, A. Y. Tremblay, Correlation of the transport properties for the ethanol–water system using neural networks, Chemical Product and Process Modeling. 3 (1): Article 56, 2008.

[99] W. W. Baumann, F. Thiele. Heat and mass transfer in evaporating two component liquid film flow, International Journal of Heat and Mass Transfer, 33(2): 267 – 273, 1990.

[100] X. Cui, X. Li, H. Sui, H. Li. Computational fluid dynamics simulations of direct contact heat and mass transfer of a multicomponent two phase film in a inclined channel at a sub-atmospheric pressure, International Journal of Heat and Mass Transfer, 55: 5808 – 5818, 2012.

[101] K. Kanatani, A. Oron. Nonlinear dynamics of confined thin liquid-vapor bilayer systems with phase change, Physics of Fluids, 23, 032102: 1-14, 2011.

[102] J. P. Burelbach, S. G. Bankoff, S. H. Davis. Nonlinear stability of evaporating/condensing liquid films, Journal of Fluid Mechanics, 195: 463-494, 1988.

[103] M. Gerendas, S. Wittig. Experimental and numerical investigation on the evaporation of shear driven multicomponent liquid wall films, Journal of Engineering for gas turbines and power, 123(3): 580 – 588, 2001.

[104] W. Brustaert. A model for evaporation as a molecular diffusion process into a turbulent atmosphere, Journal of Geophysical Research, 70(20): 5017 - 5024, 1965.

[105] J. B. Heywood. (Woschni model) Internal combustion engine fundamentals, Mcgraw-hill, New York, 1988.

[106] D. Park. The influence of different In-cylinder flows on combustion in an SI engine, Ph.D. dissertation, University of Toronto, Toronto, 2005.

[107] A. Alharbi. High speed high resolution vector field measurements and analysis of boundary layer flows in an internal combustion engine, Ph.D. dissertation, University of Michigan, Ann Arbor, Michigan, 2010.

[108] A. Alharbi. Investigation of Boundary layers in internal combustion engines using a hybrid algorithm of high speed micro – PIV and PTV, Experiments in Fluids, 49(4): 949-959, 2010.

[109] S. B. Han, Y. J. Chung, S. Lee. Effect of engine variables on the turbulent flow of a spark ignition engine, Korean Society of Mechanical Engineers Journal, 19(4): 492-501, 1995.

[110] R. G. Prucka, T. K. Lee, Z. Filipi, D. Assanis. Turbulence intensity calculation from cylinder pressure data in a high degree of freedom spark ignition engine, SAE Technical Paper, 2010-01-0175, 2010,

[111] A. K. Agarwal, S. Gadekar, A. P. Singh. In-cylinder air flow characteristics of different intake port geometries using tomographic PIV, Physics of Fluids, 29, 095104:1-16, 2017.

[112] H. Yu, X. Liang, G. Shu, X. Wang, Y. Wang, H. Zhang. Experimental investigation on wall film distribution of dimethyl ether/diesel blended fuels formed during spray wall impingement, Energies, 9(946): 1:17, 2016.

[113] Y. Takahashi, Y. Nakase, H. Ichinose. Analysis of the fuel liquid film thickness of a port fuel injection engine, SAE Technical Paper, 2006-01-1051, 2006.

[114] ANSYS-FLUENT (15.0) Users Manuel – theory guide.

[115] David C. Wilcox, Turbulence modeling for CFD, 1994.

[116] V. C. Patel, W. Rodi, G. Scheuerer, Turbulence models for near-wall and low Reynolds number flows: a review, American Institute of Aeronautics and Astronautics Journal, 23 (9) : 1308–1319, 1984.

[117] B. E. Launder, B. I. Sharma, Application of the energy-dissipation model of turbulence to the calculation of flow near a spinning disc, Letters in Heat and Mass Transfer, 1: 131–138, 1974.

[118] R. Abid, Evaluation of two-equation turbulence models for predicting transitional flows, International Journal of Engineering Science 31 (6): 831–840, 1993.

[119] C. K. G. Lam, K. Bremhost, A modified form of the k–e mode for prediction wall turbulence, Journal of Fluids Engineering, 103(3): 456–460. 1981.

[120] K. Abe, T. Kondoh, Y. Nagano, A new turbulence model for predicting fluid flow and heat transfer in separating and reattaching flows I: Flow field calculations, International Journal of Heat and Mass Transfer, 37 (1): 139– 151, 1994.

[121] K. C. Chang, W. D. Hsieh, C. S. Chen, A modified low-Reynolds-number turbulence model applicable to recirculating flow in pipe expansion, Journal of Fluids Engineering, 117 (3): 417–423, 1995.

[122] W. D. Hsieh, K. C. Chang, Calculation of wall heat transfer in pipe-expansion turbulence flows, International Journal of Heat and Mass Transfer, 39 (18): 3813–3822, 1996.

[123] G. K. Morris, S. V. Garimella, R. S. Amano, Prediction of jet impingement heat transfer using a hybrid wall treatment with different turbulent Prandtl number functions, Journal of Heat Transfer, 118(3): 562–569, 1996.

[124] C. K. G. Lam, K. Bremhorst, A Modified Form of the k-ε Model for Predicting Wall Turbulence, Journal of Fluids Engineering, 103(3): 456 – 460, 1981.

[125] Yang, Z. and Shih, T. H. New time scale based k-e model for near-wall turbulence. American Institute of Aeronautics and Astronautics Journal, 31: 1191-1198, 1993.

[126] K. Abe, T. Kondoh, Y. Nagano. A two-equation heat transfer model reflecting second-moment closures for wall and free turbulent flows, International Journal of Heat and Fluid Flow, 17(3): 228 – 237, 1996.

[127] B. E. Launder and D. B. Spalding. The numerical computation of Turbulence flows, Computer Methods in Applied Mechanics and Engineering, 3:269-289, 1974.

[128] S. A. Orszag, V. Yakhot, W. S. Flannery, F. Boysan, D. Choudhury, J. Maruzewski, B. Patel. Renormalization group modeling and turbulence simulations, International Conference on Near Wall Flows, Tempe, Arizona, 1993.

[129] T. H. Shih, W. W. Liou, A. Shabbir, Z. Yang, J. Zhu. A new κ − ε eddy-viscosity model for high Reynolds number turbulence flows – model development and validation, Computers Fluids, 24(3): 227 – 238, 1995.

[130] F. R. Menter. Two equation eddy viscosity turbulence models for engineering applications. American Institute of Aeronautics and Astronautics Journal, 32(8): 1598-1605, 1994.

[131] Convective Heat Transfer, Lecture Notes in University of Waterloo.

[132] S. V. Patankar, Numerical, heat and mass transfer and fluid flow, McGraw-Hill, New York, 1980, 61.

[133] A. G Fedorov, R. Viskanta and A. A. Mohamad. Turbulent heat and mass transfer in an asymmetrically heated, vertical parallel-plate channel, International Journal of Heat and Fluid Flow, 18:307-315, 1997.

[134] M. Wolfstein. The velocity and temperature distribution of one-dimensional flow with turbulence augmentation and pressure gradient, Journal of Heat and Mass Transfer, 29(3): 301-318, 1969.

[135] C. L. Yaws, Chemical Properties Handbook, McGraw-Hill, New York, 1999.

[136] K. Saha, E. Abu-Ramandan, X. Li. Multicomponent evaporation model for pure and blended biodiesel droplets in high temperature convective environment, Applied Energy, 93: 71-79, 2012.

[137] A. Dudukovic, V. Miloševic, R. Pjanovic, Gas–solid and gas–liquid mass-transfer coefficients, The Canadian Journal of Chemical Engineering, 76: 269–270, 1998.

[138] R. H Perry, D. W. Green. Perry's Chemical engineers' handbook, seventh edition, McGraw-Hill New York, 1997.

[139] A. F. Mills, Heat and mass transfer, Richard D. Irwin, Inc., MA, 1995.

[140] J. C. Crause, I. Nieuwoudt, Mass transfer in a short wetted-wall column. 1. Pure components, Industry and Engineering Chemistry Research, 38(12): 4928–4932, 1999.

[141] J. A. Rocha, J. L. Bravo, J. R. Fair, Distillation columns containing structured packing: a comprehensive model for their performance. 2. Mass-transfer model, Industry and Engineering Chemistry Research, 35: 1660 –1667, 1996.

[142] J. Zhang, G. Zhang, Z, He, J. Lin, H. Liu, Analysis of oil consumption in cylinder of diesel engine for optimization of piston rings, Chinese Journal of Mechanical Engineering, 26(1): 207 – 216, 2013.

[143] J. Westerweel, A. A. Draad, Th. Van der Hoeven, J. Van Oord. Measurement of fully developed turbulent pipe flow with digital particle image velocimetry, Experiments in Fluids, 20(3): 165 – 177, 1996.

[144] J. Kim, P. Moin, R. Moser. Turbulence statistics in fully developed channel flow at low Reynolds number, Journal of Fluid Mechanics, 177:133 – 166, 1987.

[145] G. K. El Khoury, P. Schlatter, A. Noorani, P. F. Fischer, G. Brethouwer, A. V. Johansson. Direct numerical simulation of turbulent pipe flow at moderately high Reynolds numbers, Flow, Turbulence and Combustion, 91(3): 475 – 495, 2013.

[146] F. Durst, S. Ray, B. Ünsal, O. A. Bayoumi. The development lengths of laminar pipe and channel flows, Journal of Fluids Engineering, 127(6): 1154 – 1160, 2005.

[147] A. G. Darbyshire, T. Mullin, Transition to turbulence in constant-mass-flux pipe flow, Journal of Fluid Mechanics, 289: 83 – 114, 1995.

[148] B. A. Tuna, X. Li, S. Yarusevych. Investigation of the effect of inlet turbulence on transitional wall-bounded flows, Proceedings of the ASME 2017 Fluids Engineering Divisiod Summer Meeting, Waikoloa, Hawaii, July 31 – August 3, 2017, ASME Paper No. FEDSM2017-69321, 2017.

[149] S. J. Gill, Evaporation of thin lubricant films under laminar and turbulent boundary layers, M.Sc. dissertation, University of Waterloo, Waterloo, ON. 2019.

[150] C. Brognakke, G. C. Davis and R. J Tabaczynski, Prediction of in-cylinder swirl velocity and turbulence intensity for an open chamber cup in piston engine, SAE Technical Paper, 810224, 1981.

[151] G. C. Davis, C. Broganakke, The effect of in-cylinder flow processes (swirl, squish and turbulence intensity) on engine efficiency model predictions, SAE technical Paper, 820045, 1982.

[152] M. J. Hall and F. V. Bracco, Cycle-resolved velocity and turbulence measurements near the cylinder wall of a firing S.I. engine, SAE Technical Paper, 861503, 1986.

[153] S. E. Trautwein, A. Grudno, G. Adomeit, The influence of turbulence intensity and laminar flame speed on turbulent flame propagation under engine like conditions, Symposium (International) on Combustion/ The Combustion Institute, 23(1): 723-728, 1990.

[154] S. B. Han, Y. J. Chung, S. Lee. Effect of variables on the turbulent flow of a spark ignition Engine, The Korean Society of Mechanical Engineering, 9(4): 492 – 501, 1995.

[155] A. A. Alhusseini, K. Tuzla, J. C. Chen, Falling film evaporation of Single component liquids, International Journal of Heat and Mass Transfer, 41(12): 1623-1632, 1998.

[156] S. W. Burd, R. W. Kaszeta, T. W. Simon. Measurements in film cooling flows: hole L/D and Turbulence Intensity Effects, Journal of Turbomachinery, 120(4): 791 – 798, 1998.

[157] R. J. Jenkin, E. H. James and W. M. Malalasekera. Modeling of the effects of combustion and turbulence on near-wall temperatures gradients in the cylinders of spark ignition engines", Proceedings of the Institution of Mechanical Engineers, Part D: Journal of Automobile Engineering, 212(6): 533 – 546, 1998.

[158] K. H. Lee and C. S. Lee. Effects of tumble and swirl flows on turbulence scale near top dead center in a four-valve spark ignition engine, Proceedings of the Institution of Mechanical Engineers, Part D: Journal of Automobile Engineering, 217(7): 607 – 615, 2003.

[159] Z. Barbouchi and J. Bessrour, Turbulence study in the internal combustion engine, Journal of Engineering and Technology Research, 1(9): 194-202, 2009.

[160] R. G. Prucka, T. Lee, Z. Filipi, D. Assanis. Turbulence intensity calculation from cylinder pressure data in a high degree of freedom spark ignition engine, SAE Technical Papers, 2010-01-0175, 2010.

[161] W. Tutak, A. Jamrozik. Characteristics of the flow field in the combustion chamber of the internal combustion test, Chemical and Process Engineering, 32 (3): 203-214, 2011.

[162] S. Beroun, P. Brabec, V. Dvorak, F. Malecke. Compression chamber of an SI engine with Increase turbulence, Journal of Middle European Construction and Design of Cars, 01: 15 – 21, 2012.

[163] G. Jaishankar, P. Meena, Investigations on in-cylinder tumble flows of internal combustion engine using shear stress transport model, International Journal of Engineering Research and Technology, 2(7): 2025 – 2030, 2013.

[164] A. Misdariis, A. Robert, O. Vermorel, S. Richard, T. Poinsot, Numerical methods and turbulence modeling for LES of piston engines: impact on flow motion and combustion, Oil and Gas Science and Technology, 69 (1): 83-105, 2014.

[165] D. M. Heim, D. Jesch, J. B. Ghandhil. Size-scaling effect on the velocity field of an internal combustion engine, part II: Turbulence characteristics, International Journal of Engine Research, 15(2): 193–208, 2014.

[166] A. Ghanaati1, I. Z. M. Darusl, M. F. M. Said and A. M. Andwari. A mean value model for estimation of laminar and turbulent flame speed in spark-ignition engine, International Journal of Automotive and Mechanical Engineering 11: 2224-2234, 2015.

[167] P. T. A. Cruz, J. N. S. Vianna, C. S. Moreira, Study of the turbulence intensity variation within the combustion chamber of a SI engines due to turbocharging, SAE technical Paper, 2003-08-3687, 2003.

[168] D. Littera, A. Cozzolini, M. Besch, D. Carder, M. Gautam, Effect of turbulence intensity on PM emission of heavy duty diesel trucks - Wind tunnel studies, Atmospheric Environment 162: 31 – 44, 2017.

[169] A. K. Agarwal, S. Gadekar, A. P. Singh. In-cylinder air-flow characteristics of different intake port geometries using tomographic PIV, Physics of Fluids, 29(9): 1-16, 2017.

[170] M. Bencherif, M. Tazerout, A. Lizaid, Turbulence- combustion interaction in direct injection diesel engine, Thermal Science, 18(1): 17 – 27, 2014.

[171] L. Chen, J. Pan, H. Wei, L. Zhou, J. Hua. Numerical analysis of knocking characteristics and heat release under different turbulence intensities in a gasoline engine, Applied Thermal Engineering, 159: 113879, 2019.

[172] G. K. Batchelor, A. A. Townsend. Decay of isotropic turbulence in the final period", Proceedings of the Royal Society A: Mathematical, Physical and Engineering Science, 527-538, 1948.

[173] K. Y. Chien. Predictions of channel and boundary layer flows with a low-Reynolds-number turbulence model, American Institute of Aeronautics and Astronautics Journal, 20(1): 33-38, 1982.

[174] N. R. Saad, Flow and heat transfer for multiple turbulent impinging slot jets, Ph.D. Thesis, Department of Chemical Engineering, McGill University, Montreal, Quebec, Canada, 1981.

[175] N. R. Saad, S. Polat, W.J.M. Douglas, Confined multiple impinging slot jets without crossflow effects, International Journal of Heat and Fluid Flow 13 (1): 2–14, 1992.

[176] G. K. Morris, S. V. Garimella. Orifice and impingement flow fields in confined jet impingement, Journal of Electric Packaging 120 (1): 68–72, 1998.

[177] V. Narayanan, J. S. Yagoobi, R. H. Page, An experimental study of fluid mechanics and heat transfer in an impinging slot jet flow, International Journal of Heat and Mass Transfer, 47: 1827–1845, 2004.

[178] S. S. Thakre, J. B. Joshi, CFD modeling of heat transfer in turbulent pipe flow, The American Institute of Chemical Engineers, 46 (9): 1798–1812, 2000.

[179] T. L. Bergman, A. S. Lavine, F. P. Incropera. D. P. Dewitt. Fundamentals of Heat and Mass Transfer, Seventh Edition, John Wiley and Sons, 2007.

[180] R. J. Jaywood, R. Nafziger, and M. Renksizbulut, A detailed examination of gas and liquid phase transient processes in convective droplet evaporation, Journal of Heat Transfer, 111(2): 495 – 502, 1989.

[181] M. Renksizbulut, R. Nafziger and X. Li, A mass transfer correlation for droplet evaporation in high-temperature flows, Chemical Engineering Science, 46(9): 2351 – 2358, 1991.

[182] E. R. Gilliland, T. K. Sherwood. Diffusion of vapors into air streams, Industrial and Engineering Chemistry. 26 (5): 516–523, 1934.

[183] R. Kafesjian, C. A. Plank, E. R. Gerhard, Liquid flow and gas phase mass transfer in wetted-wall towers, American Institute of Chemistry Journal, 7 (3): 463–466, 1961.

[184] A. K. K. Pant, V. K. Srivastava, Mass transport correlation for CO2 absorption in aqueous monoethanolamine in a continuous film contactor, Chemical Engineering Processing: Process Intensification, 47 (5): 920–928, 2008.

[185] C. Strumillo, K. E. Porter, The evaporation of carbon tetrachloride in a wetted wall column, American Institute of Chemistry Journal, 11 (6): 1139–1142, 1965.

[186] J. C. Crause, I. Nieuwoudt. Mass transfer in a short wetted-wall column. 1. Pure components, Industry and Engineering Chemistry Research, 38 (12): 4928–4932, 1999.

[187] J. A. Rocha, J. L. Bravo, J. R. Fair, Distillation columns containing structured packings: a comprehensive model for their performance. 2. Mass-transfer model, Industry and Engineering Chemistry Research, 5 (5): 1660–1667, 1996.

[188] J. B. Haelssig, A. Y. Tremblay, J. Thibault, S. Gh. Etemad, Direct numerical simulation of interphase heat and mass transfer in multicomponent vapour–liquid flows, International Journal of Heat and Mass Transfer, 53: 3947 – 3960, 2010.

[189] B. E. Poling, J. M. Prausnitz, J. P. O'Connell. The properties of gases and liquids, Fifth Edition, McGraw- Hill, 2001.

APPENDICES

Appendix A
Thermo-physical Property Correlations

Gas and liquid phase pure component property correlations are presented for n-octane(C_8H_{18}), n-decane($C_{10}H_{22}$), and n-Octadecane($C_{18}H_{38}$), bases on the data and recommendation from Reid *et al.* [189].

Table A.1: Thermo-physical property correlations.

	Gaseous phase	Liquid phase
Viscosity μ_i	$\mu_{g,i} = a + bT + cT^2 + dT^3$	$\mu_{l,i} = a \exp\left(\frac{b}{T}\right)$
Thermal Conductivity K_i	$k_{g,i} = a + bT + cT^2 + dT^3$	$k_{,i,l} = a + bT$
Specific heat $Cp_{,i}$	$Cp_{g,i} = a + bT + cT^2 + dT^3$	$Cp_{l,i} = a + bT + cT^2$
Diffusion coefficient $D_{i,j}$	$D_{i,j,m} = \frac{0.0143T^{1.75}}{PM_{ij}^{1/2}[(\sum V)_i^{1/3} + (\sum V)_j^{1/3}]}$	-
Density ρ_i	-	$\rho_i = a(b-T)^c$

Note: the mixing law for the liquid density is $\rho_{l,m} = \left(\sum_{i=1}^{n} \frac{Y_i}{\rho_i}\right)^{-1}$

Table A.2: Gas phase correlation coefficients.

	i, j	a	b	c	d
$\mu_{g,i}$	C_8H_{18}	3.265×10^{-7}	1.95×10^{-8}		
	$C_{18}H_{38}$	-2.271×10^{-7}	1.355×10^{-8}		
	air	2.345×10^{-8}	6.203×10^{-8}	-2.92×10^{-11}	7.3×10^{-15}
$k_{g,i}$	C_8H_{18}	2.282×10^{-3}	-1.46×10^{-5}	1.885×10^{-7}	-7.83×10^{-11}
	$C_{18}H_{38}$	2.514×10^{-8}	-8.16×10^{-6}	9.149×10^{-8}	-4.18×10^{-12}
	air	-4.536×10^{-3}	1.23×10^{-4}	-7.95×10^{-8}	2.73×10^{-11}
$Cp_{g,i}$	C_8H_{18}	33.73	6.305	-3.106×10^{-3}	5.672×10^{-7}
	$C_{18}H_{38}$	-52.58	6.729	-3.739×10^{-3}	8.052×10^{-7}
	air	1013	-0.1571	4.910×10^{-4}	-2.055×10^{-7}

Table A.3: liquid phase correlation coefficients.

	i, j	a	b	c	d
$\mu_{l,i}$	C_8H_{18}	1.570×10^{-5}	962.1		
	$C_{18}H_{38}$	90257×10^{-6}	1724		
$k_{l,i}$	C_8H_{18}	0.21949	-3.275×10^{-4}		
	$C_{18}H_{38}$	0.20562	-1.918×10^{-4}		
$Cp_{l,i}$	C_8H_{18}	1897	-1.443	0.00896	-1.037×10^{-6}
	$C_{18}H_{38}$	2778	-42-.201	0.01050	
$\rho_{l,i}$	C_8H_{18}	136.1	556.3	0.29	
	$C_{18}H_{38}$	103.7	727	0.33	

Appendix B
Analytical Solution for Evaporation in Stagnant Gas Medium

B.1 Infinite Space

For the wall film evaporating in the infinite space, after introducing a dimensionless vapor mass fraction $\varphi = \frac{Y_i}{Y_{i,s}}$ and the similarity variable $\eta = y/\sqrt{4Dt}$ the governing equation (Eq. (5.1)) can be simplified as:

$$\frac{d^2\varphi}{d\eta^2} + 2\eta \frac{d\varphi}{d\eta} = 0 \tag{B.1}$$

After applying the boundary conditions and integral this equation twice, the analytical solution for equation (Eq. A.1) is:

$$\varphi = 1 - \frac{\int_0^\eta exp(-u^2)du}{\int_0^\infty exp(-u^2)du} = 1 - erf(\eta) \tag{B.2}$$

Substituting the dimensionless vapor mass fraction and the similarity variable into the solution gives:

$$Y_i = Y_{i,s}\left(1 - erf\left(y/\sqrt{4Dt}\right)\right) \tag{B.3}$$

B.2 Finite Space

In this case, wall film is assumed to evaporate in a finite space and the initial and boundary conditions for this case are displayed in Table 5.1 as case-II. After introducing the following dimensionless variables $\varphi = \frac{Y_i}{Y_{i,s}}$, $\eta = \frac{y}{y_b}$ and $\tau = \frac{Dt}{y_b^2}$, the governing equation for this case can be simplified as:

$$\frac{\partial \varphi}{\partial \tau} = \frac{\partial^2 \varphi}{\partial \eta^2} \tag{B.4}$$

At infinite time the system reaches a steady-state, and the vapor species mass fraction profile for steady state can be noted as $\varphi_\infty(\eta)$. So that at $\tau = \infty$, equation (Eq. B.4) becomes:

$$0 = \frac{\partial^2 \varphi_\infty}{\partial \eta^2} \tag{B.5}$$

With $\varphi_\infty = 1, \text{at } \eta = 0$ and $\frac{\partial \varphi_\infty}{\partial \eta} = 0, \text{at } \eta = 1$. Solving this equation (Eq. B.5) with its boundary conditions, the steady-state limiting profile can be got as:

$$\varphi_\infty = 1 \tag{B.6}$$

Then the tentative vapor mass fraction profile can be assumed as:

$$\varphi(\eta, \tau) = \varphi_\infty(\eta) - \varphi_t(\eta, \tau) \tag{B.7}$$

where $\varphi_t(\eta, \tau)$ is the transient part of the solution, which decreases to zero as time increases to infinity.

Substituting this expression into the governing equation (Equation B.4) and then the equation for φ_t is obtained, as:

$$\frac{\partial \varphi_t}{\partial \tau} = \frac{\partial^2 \varphi_t}{\partial \eta^2} \tag{B.8}$$

The pertinent boundary conditions are now:

$$\text{I.C: } at\ \tau\ \leq 0,\ \varphi_t = \varphi_\infty \tag{B.9}$$

$$\text{B.C.1: } at\ \eta = 0,\ \varphi_t = 0 \tag{B.10}$$

$$\text{B.C.2: } at\ \eta =\ 1,\ \frac{\partial \varphi_t}{\partial \eta} = 0 \tag{B.11}$$

Now, using the method of separation of variables, the tentative solution of φ_t is in the form of

$$\varphi_t = f(\eta)g(\tau) \tag{B.12}$$

Substitution of this trial solution into equation (Eq. B.8) and then division by the product $f(\eta)g(\tau)$, the partial equation can be separated into two single variable partial equations. After solving these equations separately and combining the general solution for each equation, we can get the general solution for φ_t as:

$$\varphi_t = \big(Bsin(c\eta) +\ Ccos(c\eta)\big)Ae^{-c^2\tau} \tag{B.13}$$

In which A, B and C are constants of integration.

Applying the boundary conditions and initial conditions, the general solution of equation (Eq. B.8) can be written as:

$$\varphi_t =\ \sum_{n=1}^{\infty} \frac{4}{(2n-1)\pi} exp\left(-\left(\frac{(2n-1)\pi}{2}\right)^2 \tau\right) sin\left(\frac{(2n-1)\pi}{2}\eta\right),\ \text{with } n =\ 1,2,3 \ldots \tag{B.14}$$

Substituting the steady and transient part of the analytical solutions into the tentative analytical solution, the finial expression for the non-dimensional mass fraction φ becomes:

$$\varphi = 1 - \sum_{n=1}^{\infty} \frac{4}{(2n-1)\pi} exp\left(-\left(\frac{(2n-1)\pi}{2}\right)^2 \tau\right) sin\left(\frac{(2n-1)\pi}{2}\eta\right), \text{with } n = 1,2,3 \ldots \quad \text{(B.15)}$$

B.3 Oscillating Boundary Conditions

For the third case, wall film is evaporating with oscillating boundary conditions. The solution of the vapor mass fraction profile is of the form as:

$$Y_i(y,t) = Y_{i,m} + \mathcal{R}\left(Y_{i,1}(y)e^{i\omega t}\right) \quad \text{(B.16)}$$

Substitute this trail into original partial equation, Equation (5.1), and obtains:

$$\mathcal{R}\left(Y_{i,1} i\omega e^{i\omega t}\right) = D\mathcal{R}\left(\frac{d^2 Y_{i,1}}{dy^2} e^{i\omega t}\right) \quad \text{(B.17)}$$

where $\mathcal{R}(z)$ means the real part of z.

Then Equation (B.17) can be transformed to:

$$\frac{d^2 Y_{i,1}}{dy^2} - \left(\frac{i\omega}{D}\right) Y_{i,1} = 0 \quad \text{(B.18)}$$

The general solution of Equation (B.18) is

$$Y_{i,1} = C_1 e^{\sqrt{i\omega/D}\, y} + C_2 e^{-\sqrt{i\omega/D} y} \quad \text{(B.19)}$$

Since $\sqrt{i} = \pm(1/\sqrt{2})(1+i)$, this solution can be transformed as:

$$Y_{i,1} = C_1 e^{\sqrt{\omega/2D}\,(1+i)y} + C_2 e^{-\sqrt{\omega/2D}(1+i)y} \quad \text{(B.20)}$$

After applying the boundary conditions, the solution for equation (B.18) is obtained as:

$$Y_{i,1} = Y_{is} e^{-\sqrt{\omega/2D} y} \mathcal{R}\left(e^{-i\left(\sqrt{\omega/2D} y - \omega t\right)}\right) \quad \text{(B.21)}$$

Substituting the solution of Y_{i_1} into the trail solution of Y_i equation (B.19) gives:

$$Y_i(y,t) = Y_{i,m} + Y_{is}e^{-\sqrt{\omega/2D}y}cos(\,\omega t - \sqrt{\omega/2D}\,y) \qquad \text{(B.22)}$$

Appendix C
Wall Treatment of Turbulent Models

C. 1 Near Wall Treatment of $k - \varepsilon$ Model

The presence of wall can significantly affect the turbulence flow, despite the obvious constrain that the mean velocity needs to satisfy the non-slip conditions. In the close wall region, the velocity fluctuation reduces to almost zero, due to the damping effects in the tangential direction and the kinematic blocking in the normal direction. However, in the region far from the wall, the turbulence rapidly increases due to the production of turbulence kinetic energy. Therefore, as the main source of vorticity and turbulence, the near wall region is crucial for the numerical simulation of the flow fields. Furthermore, the energy and species transport also occurs vigorously due to the large mean velocity gradient.

The near wall region can be largely divided into three sub-layers according to the experimental measurements. In the inner region, which is called "viscous sublayer", in which the flow is almost laminar and the molecular viscosity dominants the momentum, heat and mass transfer. In the outer region, also known as "fully turbulent region or log-law region", the turbulence is important on the transport of mass momentum and energy. Finally, there is a buffering region between the viscous sublayer and the fully turbulent layer, in which the effects of molecular viscosity and turbulence are equally important. Furthermore, there is an outer region outside the log-law region.

Traditionally, there are two major approaches to model the flow in the near wall region. The first approach is called "wall functions", in which a semi-empirical model is used to bridge the viscosity – affected region between the wall and the fully turbulent region away from the wall. The use of wall functions obviates the need to modify the turbulence modes to account for the presence of the

wall; however, the numerical results deteriorate under fine meshes, especially when y^+ value is less than 15. The other approach for the near wall region modeling is called "near wall modeling" approach, in which the turbulence model is modified to resolve the viscosity affected region all the way to the wall, including the viscous sublayer.

Wall functions

Wall functions are a set of semi-empirical equations, which "bridge" the solution variables at the near wall cells and the corresponding quantities on the wall. The wall functions are usually consisted of two parts. The first one is law of the wall for the mean velocity and temperature; and the second part is the formula for the near wall turbulent quantities.

Near wall modeling approach (enhanced wall treatment $\varepsilon -$ equation)

Enhanced wall treatment for the $\varepsilon -$ equation is a near wall modeling method, which combines a two-layer model with enhanced wall functions.

Two layers model for enhanced wall treatment

The viscosity-affected near wall region is completely resolved in the near-wall model. The two layer approach is used to calculate both turbulence kinetic energy dissipation rate ε and the turbulent viscosity in the near wall grids. In this approach, the computational domain is divided into a viscosity-affected region and a fully turbulent region. The two regions is determined by a wall-distance based, turbulent Reynolds number, Re_y, defined as,

$$Re_y = \frac{\rho y \sqrt{k}}{\mu} \tag{C.1}$$

In which, y is interpreted as the distance to the nearest wall, and it is independent of the mesh topology.

In the fully turbulent region $(Re_y > Re_y^*, Re_y^* = 200)$, the $k-$ ε model is adopted, while in the viscosity affected region $(Re_y < Re_y^*)$, the one equation model of Wolfstein [134] is used. In the one equation model, the momentum equation and the k equation are the same as $k-$ ε model, however, the turbulent viscosity, μ_t, is calculated from

$$\mu_{t,2layer} = \rho C_\mu l_\mu \sqrt{k} \tag{C.2}$$

where l_μ is the length scale, which can be determined by

$$l_\mu = yC_l^*\left(1 - e^{-\mathrm{Re}_y/A_\mu}\right) \tag{C.3}$$

The turbulent viscosity in a two layer model is smoothly blended with the high Reynolds number μ_t and the two layer turbulent viscosity $\mu_{\mathrm{t,2layer}}$.

$$\mu_{\mathrm{t,enh}} = \lambda_\varepsilon \mu_t + (1 - \lambda_\varepsilon)\mu_{\mathrm{t,2layer}} \tag{C.4}$$

The blending function is defined as：

$$\lambda_\varepsilon = \frac{1}{2}\left[1 + \tanh\left(\frac{\mathrm{Re}_y - \mathrm{Re}_y^*}{A}\right)\right] \tag{C.5}$$

The constant A in (Equation C.5) determines the width of the blending function, and the width can be given as a variable of ΔRe_y, as a result is

$$A = \frac{|\Delta Re_y|}{\mathrm{artanh}(0.98)} \tag{C.6}$$

Typically, $\Delta\mathrm{Re}_y$ is assigned a value that is between 5% and 20% of Re_y^*.

The ε in the viscosity-affected region can be calculated as

$$\varepsilon = \frac{k^{3/2}}{l_\varepsilon} \tag{C.7}$$

The length scale is computed form the equation developed by Chen and Patel as

$$l_\varepsilon = yC_l^*\left(1 - e^{-\mathrm{Re}_y/A_\varepsilon}\right) \tag{C.8}$$

In the region of the viscosity-affected region $\left(\mathrm{Re}_y < \mathrm{Re}_y^*\right)$, the ε value is obtained algebraically from equation *.

The constants are taken form [114], as follows $C_l^* = kC_\mu^{-3/4}$, $A_\mu = 70$, $A_\varepsilon = 2C_l^*$

Enhanced wall treatment for momentum equations

The single wall function is employed here to extend the capability throughout the near-wall region (from viscous sublayer in the near wall region, to buffer region and to the fully-turbulent outer region). The expression of the blending function is suggested as:

$$u^+ = e^\Gamma u_{lam}^+ + e^{1/\Gamma} u_{tub}^+ \tag{C.9}$$

Where the blending function is given by

$$\Gamma = -\frac{a(y^+)^4}{1+by^+} \tag{C.10}$$

With constant of $a = 0.01$, and $b = 5$.

With

$$\mathrm{u}_{\mathrm{lam}}^+ = \mathrm{y}^*, \qquad \mathrm{y}^* \le 11.225 \tag{C.11}$$

$$\mathrm{u}_{\mathrm{turb}}^+ = \frac{1}{\kappa}\ln(\mathrm{Ey}^*), \quad \mathrm{y}^* > 11.225 \tag{C.12}$$

in which κ is the Von Kaman constant (0.4187), and E is an empirical constant (9.793), U_P and k_P are the mean velocity, turbulent kinetic energy of the wall-adjacent cell centroid, and y_P represents distance from the centroid of the wall-adjacent cell to the wall, respectively; μ is the dynamic viscosity of the fluid;

The range of y^* values, in which wall functions are suitable to use, depends on the overall Reynolds number of the flow. The lower limit is always in the order of $y^* \sim 15$, while the upper limit varies with the overall Reynolds number. Here a value of 60 is choose as the upper limit of the Reynolds number as the experimental results suggested.

Wall boundary conditions for Standard $k-$ ε model

In the $k-$ ε model, the k equation is solved in the whole computational domain and the boundary condition of k at the wall is defined as,

$$\frac{\partial k}{\partial n} = 0 \tag{C.13}$$

n is the normal direction of local coordinate at the wall.

The production of the turbulence kinetic energy and its dissipation rate are the source terms in the k equation, which is calculated based on the local equilibrium hypothesis. With this assumption, the production of k is equal to its dissipation rate in the wall adjacent cells. Therefore, the production of k can be estimated by

$$G_k \approx \tau_w \frac{\partial U}{\partial y} = \tau_w \frac{\tau_w}{\kappa \rho C_\mu^{1/4} k_P^{1/2} y_P} \tag{C.14}$$

$$\varepsilon_P = \frac{C_\mu^{3/4} k_P^{3/2}}{\kappa y_p} \tag{C.15}$$

C.2 Near Wall Treatment of $k-\omega$ Model

The SST $k-$ ω model use the standard $k-$ ω model in the near wall region, which can model the low-Reynolds effects, and $k-$ ε model away from the wall to resolve the problem of sensitivity of the solutions to values of k and ω outside the shear layer. A blending function is developed to add both models together, which is designed to activate the standard $k-$ ω model in the near wall region and activate the transformed $k-$ ε model in the outer region.

For the SST $k-$ ω model, the transport of turbulent kinetic energy and specific turbulent dissipation rate can be written as

$$\frac{\partial \rho k}{\partial t} + \frac{\partial (\rho k U_j)}{\partial x_j} = \frac{\partial}{\partial x_j}\left[\left(\mu + \frac{\mu_t}{\sigma_k}\right)\frac{\partial k}{\partial x_j}\right] + G_k - Y_k \tag{C.16}$$

$$\frac{\partial \rho \omega}{\partial t} + \frac{\partial (\rho \omega U_j)}{\partial x_j} = \frac{\partial}{\partial x_j}\left[\left(\mu + \frac{\mu_t}{\sigma_\omega}\right)\frac{\partial \omega}{\partial x_j}\right] + G_\omega - Y_\omega + D_\omega \tag{C.17}$$

σ_k and σ_ω in the SST $k-$ ω model is the turbulent Prandtl number for k and ω, which is defined as:

$$\sigma_k = \frac{1}{F_1/\sigma_{k,1} + (1-F_1)/\sigma_{k,2}} \tag{C.18}$$

$$\sigma_\omega = \frac{1}{F_1/\sigma_{\omega,1} + (1-F_1)/\sigma_{\omega,2}} \tag{C.19}$$

where the blending function $F_1$is defined as

$$F_1 = \tanh\left\{\min\left[\max\left(\frac{2\sqrt{k}}{0.09\omega y}, \frac{500\mu}{\rho y^2 \omega}\right), \frac{4\rho k}{\sigma_{\omega,2} D_\omega^+ y^2}\right]^4\right\} \tag{C.20}$$

with

$$D_\omega^+ = \max\left(2\rho \frac{1}{\omega \sigma_{\omega 2}} \frac{\partial k}{\partial x_j}\frac{\partial \omega}{\partial x_j}, 10^{-10}\right) \tag{C.21}$$

The turbulent viscosity in the SST $k-$ ω model is calculated as,

$$\mu_t = \frac{\rho k}{\omega} \frac{1}{\max\left(\frac{1}{\alpha^*}, \frac{SF_2}{a_1 \omega}\right)} \tag{C.22}$$

In which y is the distance from the wall, and α^* defined as

$$\alpha^* = \alpha_\infty^* \left(\frac{\alpha_0^* + \mathrm{Re}_t/R_k}{1 + \mathrm{Re}_t/R_k}\right) \tag{C.23}$$

where Re_t is the turbulent Reynolds number, defined as $\frac{\rho k}{\mu \omega}$; S is the mean rate of strain tensor and F_2 is defined as

$$F_2 = \tanh\left\{\left[\max\left(\frac{2\sqrt{k}}{0.09\omega y}, \frac{500\mu}{\rho y^2 \omega}\right)\right]^2\right\} \tag{C.24}$$

in which y is corresponding to the distance from the wall.

G_ω represents the production of ω, which can be calculated as,

$$G_\omega = \alpha \frac{\omega}{k} G_k \tag{C.25}$$

In which the coefficient α is calculated by,

$$\alpha = \frac{\alpha_\infty}{\alpha^*} \left(\frac{\alpha_0 + \mathrm{Re}_t/R_\omega}{1 + \mathrm{Re}_t/R_\omega}\right) \tag{C.26}$$

Y_k corresponding to the dissipation of k, which can be calculated as

$$Y_k = \rho \beta_i^* k \omega \tag{C.27}$$

and Y_ω is the dissipation of ω, calculated form

$$Y_\omega = \rho \beta_i \omega^2 \tag{C.28}$$

D_ω is the blending function to blend these two equation models, which can be defined as,

$$D_\omega = 2(1 - F_1)\rho \frac{1}{\omega\sigma_{\omega 2}} \frac{\partial k}{\partial x_j} \frac{\partial \omega}{\partial x_j} \tag{C.29}$$

The closure constants are:

$a_1 = 0.31, \alpha_0^* = 0.024, R_k = 6, \alpha_\infty^* = 1,\ R_\omega = 2.95, \beta_{i,1} = 0.075, \beta_{i,2} = 0.0828,$

$\beta_\infty^* = 0.\ 09, R_\beta = 8, \sigma_{k,1} = 1.176\ , \sigma_{k,2} = 1.0, \sigma_{\omega,1} = 2.0\ , \sigma_{\omega,2} = 1.168,\ \alpha_\infty = F_1\alpha_{\infty,1} + (1 - F_1)\alpha_{\infty,2}\ ,\ \alpha_{\infty,i} = \frac{\beta_{i,i}}{\beta_\infty^*} - \frac{k^2}{\sigma_{\omega,1}\sqrt{\beta_\infty^*}}, \beta_i^* = \beta_\infty^* \left[\frac{4/15 + \left(Re_t/R_\beta\right)^4}{1 + \left(Re_t/R_\beta\right)^4}\right],\ \beta_i = F_1\beta_{i,1} + (1 - F_1)\beta_{i,2}.$

The wall boundary conditions for the k equation in the $k - \omega$ model is the same as the boundary conditions for k equation in $k - \varepsilon$ models when the enhanced wall treatment is used. This means that all boundary conditions for wall-function meshes will correspond to the wall function approach; however, when the meshes are fine, appropriate low Reynolds number boundary conditions will be applied.

For the value of ω at the wall is specified as

$$\omega_w = \frac{\rho(u^*)^2}{\mu}\omega^+ \tag{C.30}$$

Analytical solution can be obtained for both the laminar sublayer and logarithm region as:

$$\omega_{lam}^+ = \frac{6}{\beta_i(y^+)^2} \tag{C.31}$$

$$\omega_{tur}^+ = \frac{1}{\sqrt{\beta_\infty^*}} \frac{du_{turb}^+}{dy^+} \tag{C.32}$$

Appendix D
List of User Defined Functions

D.1 User Subroutines

#define …

Define the model related parameters

double Get_rho_oct_liquid(double T)

Calculate local density values of liquid phase

double Get_rho_air_gas(double T)

Calculate local density values of the air in the gaseous phase

double Get_rho_gas(cell_t c,Thread *t)

Calculate local density values of the mixture in the gaseous phase

double Get_mu_oct_liquid(double T)

Calculate the octane viscosity in the liquid phase

double Get_mu_oct_gas(double T)

Calculate the octane vapor viscosity

double Get_mu_air_gas(double T)

Calculate the air viscosity

double Get_mu_gas(cell_t c,Thread *t)

Calculate the effective viscosity in the gas phase

double Get_mu_liquid(cell_t c,Thread *t)

Calulate the effective viscosity in the liquid phase

double Get_k_oct_liquid(double T)

Calculate the thermal conductivity of liquid octane

double Get_k_oct_gas(double T) Get the thermal conductivity of octane vapor

Calculate the thermal conductivity of octane vapor

double Get_k_air_gas(double T)

Calculate the effective thermal conductivity of air in the gaseous phase

double Get_k_gas(cell_t c,Thread *t)

Calculate the effective thermal conductivity of the gaseous phase

double Get_k_liquid(cell_t c,Thread *t)

Get the effective thermal conductivity in the liquid phase

double Get_cp_oct_liquid(double T)

Get the thermal conductivity of liquid octane

double Get_cp_oct_gas(double T)

Get the thermal conductivity of octane vapor

double Get_cp_air_gas(double T)

Get the effective thermal conductivity of air in the gaseous phase

double Get_cp_gas(double T)

Get the effective thermal conductivity of the gaseous mixture

double Get_cp_liquid(double T) /* heat capacity of gasmixture */

Get the effective thermal conductivity in the gaseous phase

double Get_Diff_air_gas(double T)

Calculate Octane vapor -- air diffusion coefficient

double Get_Diff_gas(cell_t c,Thread *t, int i)

Calculate diffusion coefficient in the gaseous phases

double Get_hfg(double T)

Get the latent heat;

double Get_P_sat(double T)

Calculate the saturated pressure

double Get_yi_s_oct(double T_s)

Calculate the interfacial vapor mass fraction of octane

double Get_Sou_yi_g_oct(cell_t c,Thread *t)

Calculate the interfacial mass fraction of octane in the gas phase

double Get_Sou_x_momentum(cell_t c,Thread *t)

Calculate the interfacial momentum fraction of octane in the gas phase

double Get_Sou_ms_g_oct(cell_t c,Thread *t)

Calculate the interfacial mass fraction of in the gas phase

double Get_Sou_ms_li_oct(cell_t c,Thread *t)

Calculate the interfacial mass fraction of in the liquid phase

D.2 Standard UDFs on the FLUENT Platform

enum /* UDMs */

{….

NUM_UDM

};

Name all the variables needed to be calculated in the model

DEFINE_PROPERTY(charname, c, t)

{ double var;

var= …;

return var;

}

DEFINE_SPECIFIC_HEAT(charname ,T , Tref,h, yi)

{…}

Usage: specific heat is different from other definitions

DEFINE_DIFFUSIVITY(diffusivity,c,t,i)

{ …}

Usage： define diffusivity in the model

```
DEFINE_INIT(Evap_initialization, d)
{
   thread_loop_c(t,d)
     {  begin_c_loop(c,t)
        { …
        }end_c_loop(c,t)
}
}
```

Usage： model initialization

```
DEFINE_ADJUST(Evap_adjust,d)
{
    thread_loop_c(t,d)
    { begin_c_loop_all(c,t)
       {…}end_c_loop_all(c,t)
    }
}
```

Usage: model related parameter and variables updates

```
DEFINE_SOURCE(name, c, t, dS, eqn)
{ double source;
```

```
    source= …;
    dS[equ] = …;
    return source;
}
```

Usage：source term calculations and return them to the governing equations

Appendix E
Numerical Results Samples

E.1 Evaporation in Laminar Flow Conditions

Table E.1.1: Numerical results of the average Sherwood number for the evaporation of liquid wall film in laminar air stream at $\mathrm{Re}_{g,\infty} = 1.7 \times 10^4$ and $T_\infty = 1000\mathrm{K}$ at different non-dimensional time instants.

Point/ #	1	2	3	4	5	6	7	8	9
t^*	0.4	0.6	0.8	1.0	1.2	1.4	1.6	1.8	2.0
$\overline{\mathrm{Sh_f}}$	191.88	156.92	132.59	113.97	97.18	81.13	65.98	53.00	42.94

Table E.1.2: Numerical results of the average Sherwood number for evaporation of liquid wall film at different non-dimensional time instants with different flow conditions at the inlet (Reynolds number, $Re_{g,\infty}$).

$Re_{g,\infty}$ / t^*	8.5×10^3	1.7×10^4	3.4×10^4	5.1×10^4	6.8×10^4
0.4	135.18	191.88	245.53	296.53	340.04
0.6	108.76	156.92	197.04	237.84	272.65
0.8	90.38	132.59	163.31	197.02	225.77
1	76.31	113.97	137.50	165.77	189.90
1.2	63.88	97.18	114.74	138.25	158.30
1.4	52.28	81.13	93.58	112.68	128.96
1.6	42.18	65.98	75.41	90.77	103.87
1.8	33.61	53.00	60.01	72.21	82.61
2.0	27.23	42.94	48.61	58.49	66.92

E.2 Evaporation in Turbulent Flow Conditions

Table E.2.1: Numerical results of the average Sherwood number for the evaporation of liquid wall film in turbulent air stream at $\mathrm{Re}_{g,\infty} = 1.7 \times 10^4$, $T_\infty = 1000\mathrm{K}$ and $\mathrm{I}_\infty = 5\%$ at different non-dimensional time instants.

Point/ #	1	2	3	4	5	6	7	8	9
t^*	0.4	0.6	0.8	1.0	1.2	1.4	1.6	1.8	2.0
$\overline{\mathrm{Sh}_\mathrm{f}}$	267.42	181.90	112.95	89.00	74.05	63.88	58.38	56.01	55.34

Table E.2.2: Numerical results of the average Sherwood number for the evaporating liquid wall film in turbulent air streams at different non-dimensional time instants with different flow conditions at the inlet (Reynolds number, $Re_{g,\infty}$).

$Re_{g,\infty}$ / t^*	8.5×10^3	1.7×10^4	3.4×10^4	5.1×10^4	6.8×10^4
0.4	187.29	267.42	456.49	647.92	831.99
0.6	125.06	181.90	304.81	432.63	555.54
0.8	77.65	112.95	189.27	268.64	344.96
1	61.19	89.00	149.14	211.69	271.83
1.2	50.91	74.05	124.09	176.13	226.16
1.4	43.92	63.88	107.05	151.94	195.10
1.6	40.14	58.38	97.83	138.85	178.30
1.8	38.50	56.01	93.85	133.21	171.05
2.0	38.05	55.34	92.73	131.62	169.02